University of Stavanger

FACULTY OF SCIENCE AND TECHNOLOGY

MASTER THESIS

	Springsemester, 2023 Open
Author: Jakob Haugå	Jakob Haugå (author signature)
Supervisor: Associate Professor Charlotte Obhrai	
Master thesis title: Wind resource analyses at Westermost Rough Wind Farm	
Keywords: Offshore wind, reanalysis data, Atmospheric stability, WindPRO, WAsP.	Number of pages: 80 + appendices/other: 104 Stavanger, 02.07.2023 date/year

Abstract

A transition towards renewable energy sources is a pressing concern for society and government officials, and the offshore wind industry is more relevant than ever. The industry has the potential to meet Europe's energy demand by seven times, if fully realized. Reliable wind resource assessments and energy production methods are vital in order to determine the feasibility of new offshore wind farms and for technology to evolve. According to the IEC 61400-12-1 standard procedure for power curve validation of wind turbines, measurements of the wind speed is taken at hub height. The standard procedure assumes that the hub height wind speed makes a sufficient representation of the wind speed experienced across the entire rotor swept area. As the wind industry is moving offshore and the turbine rotor gets bigger, the IEC 61400-12-1 assumption becomes questionable.

This thesis examines the theoretical energy output of a reference wind turbine through hub height wind speed (HHWS) and rotor equivalent wind speed (REWS) and compare it to the actual power output retrieved from SCADA. A new method for calculating the real power curve through SCADA data has also been applied and deals with the velocity deficit caused by rotor distortion. The thesis further examines the validity of complementing reanalysis data with local measurements through scaling, using WindPRO and WAsP. This method could be strongly beneficial when the data quality in the local measurements is low.

Acknowledgements

I would like to show my gratitude to my supervisor, Associate Professor Charlotte Obhrai, for giving her support and guidance throughout this semester. I would also like to thank Ørsted for sharing the Westermost Rough data with me.

Table of Contents

Table of Figures

List of Tables

Appendices

1 Introduction

Climate change, limited energy supply, and a growing cost of energy (‘’CoE’’) has made the shift towards renewable energy sources a hot topic for society and government officials. Greenhouse gas emissions in the EU were reduced by 25% between 1990 and 2019, thanks to new policy initiatives and economic factors (EEA, 2022). However, going forward, a faster pace in the reduction of greenhouse gas emissions to accomplish the European Climate Law's aim of climate neutrality by 2050 is needed. The European Commission agreed on March 30, 2023, to boost the European Union's binding renewable objective for 2030 from 32% to a minimum of 42.5%, nearly doubling the EU's renewable energy contribution (European Commission, 2023).

The offshore wind industry is a promising application of wind power with the potential to meet Europe’s energy demand by seven times if fully realized (Stiesdal, 2019, p.11). The global interest in offshore wind power exploitation has grown significantly, mainly due to increased energy demand and the substantially greater wind speed ratios compared to onshore, resulting in the possibility of larger turbines and higher energy outputs. Since the building of the world’s first offshore wind farm in Vindeby, Denmark, in 1991, individual wind farms have developed from 5 megawatts (‘’MW’’) to more than 1000 MW (Stiesdal, 2019, p.11). During the period 2020-2021, offshore installation increased from 35.5 gigawatts (‘’GW’’) to 55.7 GW (Bojek, 2022). Despite its promising potential and rapid technical advancements, the offshore wind sector is still in its infancy, with limited integration among supply chain participants and a need for more demand, order, and inventory transparency and collaboration (Stiesdal, 2019, p.16). In order to be competitive against fossil fuel-based technologies, CoE of offshore wind power needs to be reduced, and the sharing of knowledge within the industry needs to be improved (Stiesdal, 2019, p.16).

Reliable wind resource assessments are critical in offshore wind farm development. Meteorological data for this purpose is typically delivered as a time series, which entails large volumes of data. There are several data sources, ranging from refined mesoscale model data to local observations. It is not unusual for local measurements to have gaps or incorrect data; it is also unusual to find coherent local measurements collected over long periods (Dorrego et al., 2022). As a result, various studies have been conducted to investigate the validity of reanalysis data as an alternative to measured data. Model data is frequently accessible in entire series and for long-term periods stretching back in time. Nevertheless, the model data is known to have

inaccuracies. Accurate evaluation of wind speed characteristics at wind turbine relevant height is critical in the wind energy field since an error of roughly 1% in wind speed estimation can lead to a 2% mistake in wind energy (Azad et al., 2011).

1.1 Objectives and outline

In this thesis, different analyses are performed based on data from the Westermost Rough wind farm. For a better overview of the thesis, its main objectives are outlined below and will be presented in thes same order in the results and discussion chapters.

- **Compare different methods for determining the atmospheric stability.**

The thesis compares the Bulk Richardsen and the Gradient Richardsen methods in determining atmospheric stability. The calculations have been conducted by using LiDAR data from a Leosphere Windcube which is positioned close to the center of the wind farm.

- **Use LiDAR data to calculate energy output through hub height wind speed and rotor equivalent wind speed**.

The energy output predicted though the hub height wind speed (''HHWS'') and rotor equivalent wind speed (''REWS'') is compared to the actual production SCADA data.

- **Obtain the real power curve through SCADA data.**

As a part of the thesis, a novel idea on obtaining the real power curve using SCADA data as proposed by Dai et al (2022) has been tested. The method relies on applying moving average filter (MAF) to the wind speed, and the idea is that the wind experienced on the nacelle anemometer is heavily distorted compared to the wind experienced on the rotor.

- **Scale reanalysis data to LiDAR on-cite measurements for long-time correction and compare the energy prediction to actual energy production.**

The thesis also examines the validity of complementing reanalysis data with local measurements (LiDAR) through transfer functions (scaling). This is done due to the low availability of LiDAR data in the reference period (12%), which is often the case for wind

projects. This part of the thesis is done in WindPRO, using local measurements (LiDAR), NORA3, NEWA, and ERA5 for comparison.

- **Compare performance of the Jensen wake model and the Eddy-viscosity wake model.**

Both the Jensen and the Eddy-viscosity models are used in WindPRO as part of the Annual Energy Production (AEP) calculation. The deficits due to wake are compared for the individual turbines and presented.

- **Performance check for the wind farm using SCADA data in WindPRO**

Performance check is a powerful module in WindPRO that through the use of production data, error codes, and wind data, makes analyses of the wind farm operation. The module also quantifies how much energy has been lost according to the error codes chosen, and compares the actual and potential production.

Turbine A01 (Appendix3, figure 49) has been chosen as reference turbine for some of the calculations throughout this thesis. This turbine was chosen through preliminary wake studies, where A01 showed to experience the least wake impact (figure 44) among all the 35 turbines at Westermost Rough. The turbine could therefore be assumed to be the turbine experiencing the least amount of disturbed wind.

2 Theory

2.1 Boundary Layer Meteorology

The troposphere spans from ground level to a height of roughly 11 kilometers, while the underlying surface frequently modifies only the first kilometers of altitude. The boundary layer is a part of the troposphere and is defined as the portion that is immediately impacted by the presence of the earth's surface and responds to surface forcings in a timeframe of little more than one hour (Stull, 1988). The boundary layer may be further divided into altitude portions, with the surface layer accounting for approximately 10%. Inside this layer, mechanical shear rather than buoyancy dominates turbulence. The logarithmic wind profile is based on the assumption that wind speed grows near-logarithmically in the surface layer. When the wind blows over the sea surface, the depth of the boundary layer changes rather slowly in both space and time. Because of the substantial amount of mixing within the top layer of the ocean, the sea surface temperature experiences small fluctuations throughout a diurnal cycle, as opposed to on-land circumstances. Water may also absorb a lot of heat from the sun without causing any noticeable temperature changes. A slow fluctuation in sea surface temperature equals a slow variation in surface boundary layer force. Vertical particle motion and advection of air masses over the ocean surface are the major contributors to variations in boundary layer depth offshore. When an air mass with one temperature crosses an ocean with a different temperature, the air mass changes as its temperature equilibrates to the sea surface's temperature (Stull, 1988). As a result, the offshore boundary layer becomes thinner, resulting in less turbulence and more stability.

2.2 Atmospheric Stability

The thermal stability of the atmosphere causes it to cycle between discrete states. Air parcels near the surface will be heated when the earth is heated by the sun. The heat transfer from the earth will eventually become considerable, and the rise in temperature gradient will result in turbulent mixing. Without the heat of the sun, the ground transforms from a heat source to a heat sink in the evening. As air parcels migrate below, the lower atmosphere becomes more stratified. The theory is the same for offshore conditions. However, the sea surface temperature does not follow a diurnal cycle, and stability is seasonally determined rather than diurnal. When describing wind profiles in the atmospheric boundary layer, it is critical to acknowledge atmospheric stability. Even though it is commonly acknowledged that unstable

atmospheric conditions can result in increased turbulence, it is frequently overlooked in simulations of wind turbine (WTG) load and motion offshore (Putri et al., 2019). Air is classified as a Newtonian fluid, with stress proportional to deformation rate, and can thus be represented using the Navier-Stokes equation. Turbulence kinetic energy (''TKE'') is a significant quantity used to analyze the boundary layer where buoyant thermals and mechanical eddies can generate turbulence (Wang et al., 2021a). The turbulence intensity (''TI'') is measured using the TKE theorem, which is derived from the Navier-Stokes equation. The TKE may be calculated by calculating the root mean square (''RMS'') value of the variations in flow velocity, which is defined as a turbulent flows mean KE per unit mass (Magnusson et al., 1996):

$$Kinetic\ energy = \frac{1}{2}mv^2 \quad [1]$$

$$\frac{Kinetic\ energy}{m} = TKE \quad [2]$$

$$TKE = \frac{1}{2}\left(\overline{u'^2} + \overline{v'^2} + \overline{w'^2}\right) \quad [3]$$

Where the components in equation 3, u', v' and w', represent the fluctuating velocity components in each direction (Celik, 1999). The fluctuation velocities are time-dependent and needs to be derived to equation 4 in order to see the changes with time:

$$\frac{\partial TKE}{\partial t} = \frac{g}{\theta_v}(\overline{\omega'\theta_v'}) - \overline{u'w'}\frac{\partial U}{\partial z} - \frac{\partial \overline{w'k}}{\partial z} - \frac{1}{p}\frac{\partial \overline{w'p}}{\partial z} - \epsilon \quad [4]$$

$$a \qquad b \qquad c \qquad d \qquad e \qquad f$$

Where a, is the change in TKE with respect to time; b is the buoyant term; c is the shear term; d is the transport of TKE by turbulent eddies; e is the transport of TKE by pressure perturbation; and f is the decay due to dissipation (Stull, 1988).

The formula determines whether kinetic energy is produced or consumed (buoyancy or shear). Each term can be both a producer and a consumer. When the TKE lowers over time, the atmospheric boundary layer (''ABL'') gets less turbulent; when the TKE increases over time, the ABL becomes more turbulent.

2.3 Turbulence

In contrast to surfaces on land, the sea surface roughness is not constant but strongly dependent on wind speed due to the wave height that governs from the wind, hence the surface roughness length will increase with an increase of wind speed (Csandy, 2001). Turbulence intensity is dependent on the roughness length and therefore a function of the wind speed (Vickers and Mahrt, 1997). To get a better understanding of the marine boundary layer and the operation and environment of offshore wind turbines, the understanding of TI over open sea surface is crucial. Turbulence intensity is often calculated from 10 minutes mean data retrieved from on-cite measurements, and is a relationship between the horizontal wind speed variance, σ_u, and mean wind speed u (Türk and Emeis, 2010):

$$TI = \frac{\sigma_u}{u} \quad [5]$$

The ratio between the longitudinal wind speed variance and the friction velocity u_*, is given by:

$$\sigma_u^2 = 6.25 \times u_*^2 \quad [6]$$

For load calculations on wind turbines an important measure is the 90th percentile of the TI for a given wind speed bin (Emeis, 2014). The IEC 61400-3 (2005) recommends the following wind speed dependence:

$$\sigma_{u90} = \frac{u_h}{\ln\left(\frac{z_h}{z_0}\right)} + 1.28\ (1.44 ms^{-1}) I_{15} \quad [7]$$

Where u_h is the hub height wind speed; z_h is the hub height; I_{15} is the hub height turbulence intensity average at a wind speed of 15 m/s; z_0 is the roughness length (determined through the

charnock relation, equation 10). The first right hand side component of equation 7 calculates the mean wind speed standard deviation for a thermally neutral stratification using a logarithmic wind profile (Emeis, 2014). The second term in equation 7 assumes a gaussian distribution for the wind speed standard deviation, hence the 90% percentile of the wind speed standard deviation, σ_{u90}, is 1.28 times the magnitude of standard deviation, of the wind speed standard deviation (Emeis, 2014).

2.4 Wind Profiles

2.4.1 Wind Shear

Wind shear can be described as the variation of wind speed with height. Wind shear is especially important to understand as it causes a direct impact on the available power at different turbine hub heights, and significantly influence the cyclic loading experienced by the turbine blades (Ray et al., 2006).

2.4.2 Power Law Profile

The vertical velocity profile is commonly required for estimating the KE that is available for wind turbines. In several situations, velocity measurements are limited in height. The wind profile depicts how wind speed varies with height above ground. It might be represented by an idealized model profile, most often the power law or logarithmic profile models. The power law profile is defined as follows:

$$U(z) = U(H)\left(\frac{z}{H}\right)^{\alpha} \quad [8]$$

Where U(z) represents the average wind speed; U(H) is wind speed at hub height; H is the distance in height between sea surface and rotor hub; z is the height used for reference; α is the power law exponent which according to the DNV-RP-C205 standard is set to 0.14.

The power law is frequently employed as the fundamental wind profile in wind power evaluation due to its simplicity for calculating wind speeds at turbine heights less than 50 meters from the near-surface reference height, or when correcting data from diverse heights to a standard height (Robeson, 1997).

2.4.3 Logarithmic Profile

The power law profile has limited use since it cannot account for surface roughness or the effect of atmospheric stability. The other very popular profile of use is the logarithmic profile, defined as follows:

$$U(z) = \frac{u_*}{k_a} \ln\left(\frac{z}{z_0}\right) \quad [9]$$

Where U(z) represents the wind speed at height; u_* is the friction velocity; k_a represents the Von Karman constant = 0.4 (DNV-RP-C205); z_0 is the parameter for terrain roughness; z is height.

The Charnock relation (Charnock, 1955) is extensively used to explain the change in sea surface roughness length as a function of wind speed and may be stated as:

$$z_0 = \frac{A_c U_*^2}{g} \quad [10]$$

Where A_c is the Charnock constant; U_* is the friction velocity; g the acceleration of gravity. The DNV standards make use of this relationship.

2.4.4 Stability-corrected Logarithmic Wind Profile

The atmospheric stability conditions have a considerable impact on the wind speed profile. The profiles given in equation 8 and 9 are both independent of atmospheric stability. To account for this, The DNV-RP-C205 suggests a logarithmic model with stability adjustments. The equation is as follows:

$$\mathrm{U(z)} = \frac{u_*}{k_a} \left(ln\frac{z}{z_0} - \Psi\right) \quad [11]$$

The introduction of the stability-dependent function, Ψ, which is reliant on the non-dimensional stability parameter, separates this new equation from equation 9.

$$\zeta = \frac{\mathrm{z}}{\mathrm{L}} \quad [12]$$

Where z is the height; and L is the Monin-Obukhov length. The dimensionless stability parameter is negative under steady conditions, building a more substantial wind velocity. Under unstable conditions, the reverse is true. Because the stability-dependent function is zero when the circumstances are neutral, atmospheric conditions have no effect on wind speed under those conditions.

2.4.5 Monin-Obukhov Length

Monin-Obukhov similarity theory (''MOS''), has been the scientific standard approach for the past four decades when describing the surface layer atmospheric turbulence (Grachev and Fairall, 1997). The Monin-Obukhov (''MO'') length is defined as the distance in altitude where turbulence is buoyancy dominated, rather than shear dominated. The MO length can be expressed as:

$$L = \frac{u_*^3 \overline{\theta_v}}{k_a g \overline{(w'\theta_v)_S}} \qquad [13]$$

Where u_* is the friction velocity; $\overline{\theta_v}$ the mean virtual potential temperature; $k_a$the von karman constant (0.4); and $\overline{(w'\theta_v)_S}$ the surface virtual potential temperature flux.

Following Holtsag (2014) we distinguish between the different stability classes based on their respective MO length in table 1. To determine stability, different approaches can be utilized. Some of the most popular include the Eddy-correlation method, Bulk Richardson number, and the Gradient Richardson number.

Class Boundaries	**Stability Class**
-200 ≤ L^* < 0	very unstable
$-500 \leq L - 200$	unstable
$\|L\| > 500$	neutral
$200 < L \leq 500$	stable
$0 < L \leq 200$	very unstable

Table 1: Stability class boundaries (Holtsag et al., 2014).

*The MO length is derived from on-site measurements.

2.4.6 Gradient Richardson Number

The Richardson number (Ri) is a critical nondimensional parameter when measuring the competition between the destabilizing influence of mechanical shear, and the stabilizing real Brunt-Vaisala frequency, that is, a measure of buoyancy (Geernaert, 2003). It is a coarse measure of expected turbulence. The gradient Richardson number can be expressed as:

$$Ri = -\frac{g\left(\frac{d\rho_0}{dz}\right)}{\rho_0\left(\frac{dU}{dz}\right)^2} \quad [14]$$

Where the top part of the equation is the vertical density gradient multiplied with the acceleration of gravity. The bottom part is the horizontal wind speed's vertical gradient squared, multiplied with the unperturbed density. The Ri is negative when the heat flux is upward oriented (unstable), whereas the opposite is true for positive Ri values. The different stability classes can be distinguished based on the Ri number as suggested by Obhrai et al (2012), presented in table 2:

Gradient Richardson Number	Stability Class
Ri < -5.34	very unstable
-5.34 <= Ri <-2.26	unstable
-2.26 <= Ri <-0.569	weakly unstable
-0.569 <= Ri < 0.083	neutral
0.083 <= Ri < 0.196	weakly stable
0.196 <= Ri < 0.49	stable
0.49 <= Ri	very stable

Table 2: Gradient Richardson number and corresponding stability class (Obhrai et al., 2012)

2.4.7 Bulk Richardson Number

The bulk Richardson number (Rib) is an approximation of the Ri. It is structured as a approximation of local gradients by finite differences across layers (Weisman and Klemp, 1986). The Richardson bulk number is given by:

$$Rib = \frac{\left(\frac{g}{T_v}\right)\Delta\theta_v\Delta_z}{(\Delta U)^2 + (\Delta V)^2} \quad [15]$$

Where T_v is the absolute virtual temperature; $\Delta\theta_v$ is the differences in the virtual potential temperature across a layer of thickness Δ_z. ΔV and ΔU are the change in horizontal wind components when traversing through the same layer.

2.5 Distribution Models

As we are experiencing an increase in energy demand, researchers have increased their focus on improving the efficiency of the wind power generation The first step in the development of wind energy is to assess the characteristics and the potential of wind energy. The wind speed distribution at a particular location determines the wind energy available, and the energy conversion systems performance (Chen and Blaabjerg, 2009).

The KE in the airflow is converted into electrical energy via wind turbines. The wind speed has a statistically significant positively skewed distribution. Wind power, on the other hand, exhibits volatility, intermittent characteristics and randomness, leading wind farm power output to significant fluctuate (Shi et al., 2021). In wind farm analysis, design planning, construction and O&M, several probability distribution models have been used. Many probability distribution models have been utilized in wind farm analysis, design planning, building, operation and maintenance (Wang et al., 2021b).

2.5.1 Two-Parameter Weibull Distribution

The most commonly used density function with regards to wind speed modelling is the Weibull distribution (Sarkar et al., 2019):

$$p(U) = \left(\frac{k}{\alpha}\right)\left(\frac{x}{\alpha}\right)^{k-1}\exp\left[-\left(\frac{x}{\alpha}\right)^{k}\right] \quad [16]$$

The Weibull distribution (Weibull, 1951) is a well-tested distribution that may be utilized in wind speed modeling. The shape parameter, k, and the scale parameter, a, are required by the Weibull distribution. Both the wind speed and its standard deviation are used to calculate the parameters. The shape parameter affects the width of the data distribution, whereas the scale parameter regulates the abscissa scale (Shi et al., 2021). Despite its ease of use, the two-parameter Weibull distributions performance is reduced when fitting low wind speeds, and

much worse when the wind speed data contains a large number of null values (Akgül et al., 2016). To properly fit and characterize the wind regimes, it is necessary to eliminate null values before fitting.

2.5.2 Rayleigh Distribution

When the two-parameter Weibull distribution possess a shape parameter equal to 2, it forms the Rayleigh distribution (Shi et al., 2021):

$$f(x) = \frac{x}{\alpha^2}\exp\left[-\frac{1}{2}\left(\frac{x}{\alpha}\right)^2\right] \quad [17]$$

The Rayleigh distribution is of relevance when modeling wind speed and evaluating the performance of wind turbines (Saleh et al., 2012). It is more convenient than the Weibull distribution as it only contains one parameter that is easier to estimate. The Rayleigh distribution assumes that the long-term wind vector is zero. At sea, the wind vector significantly deviates from zero. This relatively limits the applicability of the distribution to sea winds (Perrin et al., 2006).

2.5.3 Gamma Distribution

The generalized Gamma distribution is another distribution of popular use in wind speed modeling (Aries et al., 2018) and reads as following:

$$f(x) = \frac{\alpha^k}{\Gamma(k)}x^{k-1}\exp\left(-\alpha x\right) \quad [18]$$

Where α and Γ represents the scale parameter and the shape parameter, respectively.
The distribution is representing the sum of all the exponentially distributed stochastic variables identified by the scale and shape parameter (Aries et al., 2018).

2.5.4 Kernel Density Estimation

The Weibull, Rayleigh, and Gamma distributions are all parametric distributions. Although there are certain advantages with these distributions in wind speed modeling, selecting a qualifying distribution remains difficult (Shi et al., 2021). The model may not accurately characterize the actual wind regimes, and the estimated parameter values may fail statistical tests (Xu et al., 2015). However, when using a nonparametric model, the model does not have

to make any assumptions on the theoretical wind speed distribution or estimate the parameters of any distributions (Xu et al., 2015). One of the most frequently used nonparametric models is the kernel density estimation (KDE) (Qin et al., 2011). The KDE gets the probability density function from the sample data:

$$f(\alpha) = \frac{1}{nh}\sum_{i=1}^{n} K(a) \quad [19]$$

Where n is the number of samples; h is the bandwidth; K(a) the kernel function; and the relative distance between estimated and sample value is given by a which can be further described as:

$$\alpha = \frac{x - x_i}{h} \quad [20]$$

Where x is a fixed location, and xi an observation. There are several kernel functions used to generate KDE functions, the Gaussian kernel function is the most utilized kernel function in the generation of KDE functions (Han et al., 2019):

$$K(\alpha) = \frac{1}{\sqrt{2\pi}} e^{\left[-\frac{(x-x_i)^2}{2h^2}\right]} \quad [21]$$

KDE models are very adaptable and stable. Recently, Han et al. (2019) conducted a study on wind speed data from 698 wind stations at different locations in China. The results from the study showed that the KDE model outperformed the Weibull distribution along with 18 other popular parametric distributions. Anyhow, correct bandwidth selection is vital for the model to do a good fit. Otherwise, the model could experience over-fitting and under-fitting which will affect the estimated value (Han et al., 2019).

2.6 The Wind Turbine Power Curve

The WTG power curve depicts the relationship between WTG power output and wind speed, and essentially captures the performance of wind turbines. Accurate power curve models are a valuable tool in wind power forecasts and assist in wind farm growth. The relationship between the wind speed and the power for a vertical-axis wind turbine can be expressed as follows:

$$p(v) = \begin{cases} 0 & v_{out} < v < v_{in} \\ q(v) & v_{in} \le v < v_r \\ P_r & v_r \le v \le v_{out} \end{cases} \quad [22]$$

Where p(v) is the electrical power output in Watts; v_{in} is the cut-in wind speed (m/s); v_{out} is the cut-out wind speed (m/s); v_r is the rated wind speed (m/s); P_r is the rated power output in watts; and q(v) is the non-linear relationship between wind speed and power (Carillo et al., 2013). The power curve is illustrated in figure 1.

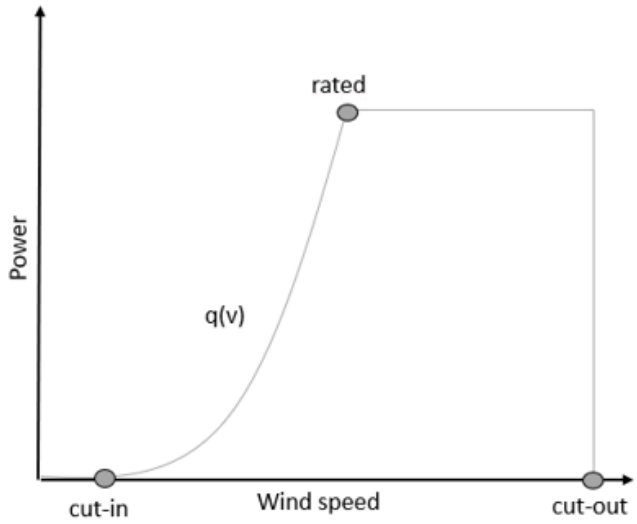

Figure 1: Power curve representation.

2.6.1 Momentum theory

As described by momentum theory, it is possible to express the power of a WTG to capture wind energy as:

$$P = \frac{1}{2}\rho S v_d (v_1^2 - v_2^2) \quad [23]$$

Where ρ is the air density; S is the rotor swept area; v_d is the wind speed that passes through the WTG rotor; v_1 is the wind speed upstream of the WTG rotor; and v_2 is the wind speed downstream of the WTG rotor. Hansen (2015) describes the relationship between the upstream wind speed, v_1, the wind speed passing though the rotor, v_d, and the downstream wind speed, v_2, as:

$$v_2 = 2v_d - v_1 \quad [24]$$

With the use of equation 24, equation 23 can now be expressed as:

$$P = 2\rho S v_d^2 (v_1 - v_d) \quad [25]$$

Subsequently, equation 25 can be expressed as (Dai et al., 2016):

$$v_1 = \frac{P}{2\rho S v_d^2} + v_d \quad [26]$$

2.6.2 Power Curve Correction Using SCADA Data

One of the key issues to be solved in the operation and maintenance process of a wind turbine is to accurately obtain the wind turbine performance. In order to calculate the theoretical power output of a wind turbine using wind data it is necessary to know the specific turbine's power curve that describes the relationship between the wind speed and the turbine's power output. This sub chapter follows Dai et al (2022) paper ''Study on Obtaining Real Power Curve of Wind Turbines Using SCADA Data'' in order to obtain the real power curve for the Siemens-Gamesa-6.0 WTG that is used at Westermost rough. The Power curve model can be expressed as:

$$P = \frac{1}{2}\rho\pi R^2 C_p(v, \omega, \beta, \gamma) v^3 \quad [27]$$

With R being the radius of the rotor; C_p the power coefficient; ω the rotational speed of rotor; β the pitch angle; and γ the yaw angle (all available from the SCADA data). The wind speed retrieved from the SCADA data is provided by anemometers installed on the nacelle, which is not the true incoming wind speed (Dai et al., 2016). As the wind travels through the rotor plane before it reaches the anemometer, a portion of the wind energy will already have been absorbed by the rotor which results in smaller measures by the anemometer than the actual incoming wind speed. As of this, if the SCADA data wind speed is directly used in analysis, there must be a significant deviation (Dai et al., 2022). Therefore, correcting the wind speed SCADA through moving average filtering before performing the power curve modelling will yield a more precise power curve.

2.6.2.1 Moving Average Filtering (MAF)

Because the effect of wind velocity on generator power is the result of wind in a specific period, modelling the power curve using velocity averages rather than the instant values is more reasonable. There is also a lag effect between variations in wind velocity and power variation to consider (Dai, et al., 2022). The primary reason for this is that the WTG rotor is a large inertial system. The moving average filtering (MAF) method is using a sliding window of certain size in order to determine the average of data points within the set window. The discrete expression of the moving average filter can be expressed as:

$$y(n) = \frac{1}{N+1}\sum_{k=0}^{N} x(n-k) \qquad [28]$$

Where y(n) is the output of the filter; x(n) is the input of the filter; and N is the window length of the MAF filter. Before the process of filtering, the null values are filled with zeros. Also, if a zero value is located in between two measurements it is repaired by averaging the adjacent data. If multiple zeros is occurring consecutively, the data is rejected:

$$\begin{cases} x(n) = 0, if\ x(n) is\ null \\ x(n) = \dfrac{x(n-1) + x(n+1)}{2}, if\ x(n) = 0, x(n-1) > 0\ and\ x(n+1) > 0 \\ x(n) = 0, if\ x(n+1) = 0, x(n+2) = 0, \ldots \end{cases} \qquad [29]$$

2.7 Power Performance Estimation

Power performance measurement is essential in the wind industry since it serves as the foundation for the wind turbine's power production forecast. A WTG power performance measurement consists of simultaneously monitoring the wind speed in front of the turbine and the turbine's power output.

To describe the wind field around the wind turbine in flat terrain, the IEC 61400-12-1 standard for wind turbine power performance assessment only requires the measurements of wind speed at hub height and air density (derived from temperature and pressure data). However, other wind characteristics, such as the variation of wind direction with height (veer), the horizontal wind speed with height above ground (shear), and the fast variation of wind speed around the 10-min average wind speed (turbulence), have been shown to influence the power performance of large WTGs (Wagner et al., 2011). That is why, in practice, the power curve measured in

accordance with the current standard is specific both to the meteorological conditions and the location during the test.

Antoniou et al. (2009), and VanLuvanee et al. (2009) discovered that power generation reduced with increased shear in their investigations. They also discovered that wind speed profiles having a greater wind speed gradient above hub height than below hub height (such as those produced by low level jets) experienced increase in power production. Their findings suggests that profiles that deviate from a power law shape may have a bigger power deviation than those that closely resemble a power law.

2.7.1 Hub Height Wind Speed

Traditionally, estimating the hub-height wind speed (HHWS) has been critical for a comprehensive wind resource assessment. The wind speed is extrapolated or interpolated in order to determine the wind speed at hub height. The power output is calculated through the equation:

$$P = \frac{1}{2} C_p A V^3 \quad [30]$$

Where P is the power output in watts; C_p is the power coefficient; A is the rotor swept area; and V is the hub height wind speed. IEC 61400-12-1 standard assumes that the hub height wind speed makes a sufficient representation of the wind speed across the whole turbine rotor swept area. The assumption becomes rather questionable as we experience growth in turbine rotor diameter and the wind speed difference experienced by the different rotor sections becomes significant. The wind profile interaction with a large rotor can be visualized in figure 2.

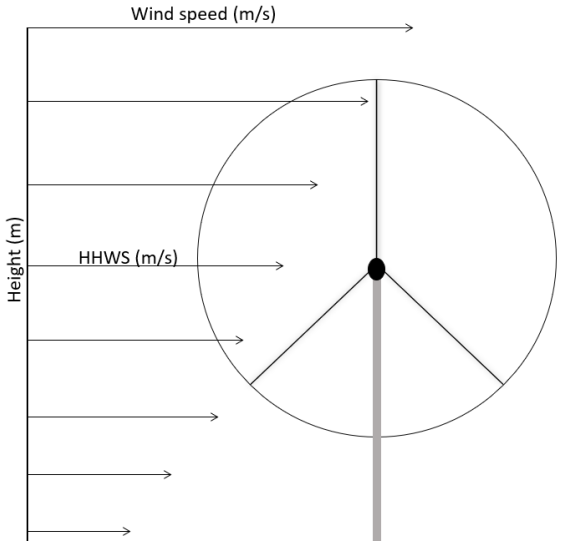

Figure 2: Hub height wind speed (HHWS)

It is assumed that in case of the wind shear coefficient being constant, the difference between the hub height wind speed and the rotor equivalent wind speed is usually small (Van Sark et al., 2019). However, an experiment carried out by Bratton and Womeldorf (2011) showed that, in some cases, a constant wind shear coefficient was insufficient in describing the wind shear profile. Wharton and Lundquist (2012) performed a similar experiment, where their findings showed to support Bratton and Womeldorf's: The difference of the HHWS and REWS could be significant.

2.7.2 Rotor Equivalent Wind Speed

Wind shear, directional shear, and direction variations are known to restrict power generation capacity, whereas turbulent intensity increases it. However, an elaborate superposition of these influences reshapes the properties of the power estimate, indicating the need for a new formulation (Choukulkar et al. 2016). Wind resource assessments have traditionally been done using meteorological towers, which give measurements at hub height (Choulkular et al. 2016). As technology advances, we witness an increase in both hub height and rotor swept area. We have also moved offshore, which provides us with a different basis for including atmospheric stability. The influence of both mechanical shear and atmospheric stability is now more important, and point measurements from met-towers are no longer a suitable depiction of turbine-wind interaction (e.g. Wharton and Lundquist 2012; Wagner et al. 2009; Sumner et al. 2006). Rotor equivalent wind speed u_{eq} can be expressed as:

$$u_{eq} = \sqrt[3]{\sum_{i=1}^{n_h} \frac{A_i}{A} u_i^3} \quad [31]$$

In which A is the rotor disk total area; A_i is the area of the i-th segment of the rotor disk; and u_i represents the wind speed at each segment. The segments are used to weight wind speeds to the area centers as illustrated in figure 3(a) . The area of the i-th segment can be determined through the equation:

$$A_i = R^2 \cos^{-1}\left(\frac{R-h}{R}\right) - (R-h)\sqrt{2Rh-h^2} \quad [32]$$

The segment area can be determined through equation 32 by utilizing the arc sine function as illustrated in figure 3(b). When establishing the first segment from the top it is assumed that radius of rotor rotation area is R, and the height of the sector is h. Further, the segment lengths can be found by following:

$$h_i = H + \frac{1}{n_h}\left[i - \left(\frac{n_h+1}{2}\right)\right] \times D \quad [33]$$

Where n_h is the total number of sectors. The relationship between rotor equivalent wind speed to hub height wind speed can be found through the following equation (Ryu et al., 2022):

$$\frac{V_{REWS}}{V_{HHWS}} = \sqrt[3]{\sum_{i=1}^{n_h} \frac{A_i}{A}\left[1 + \frac{1}{n_h}\left(i - \left(\frac{n_h+1}{2}\right)\right) \times \frac{D}{H}\right]^{3a}} \quad [34]$$

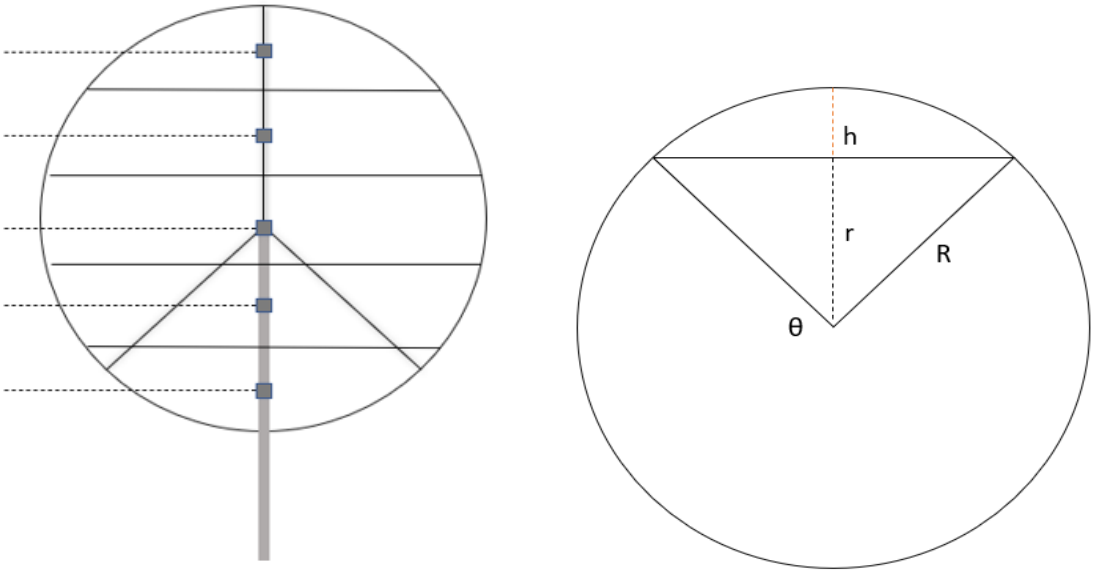

(a) (b)

Figure 3: REWS rotor segments (a); rotor area segments thorugh arc cosine function (b).

2.7.3 Annual Energy Production

According to the IEC 61400-12-1 (10, p.32) standard, the annual energy production (AEP) is calculated as described in the equation:

$$AEP = N_h \sum_{k=1}^{N} [\mathrm{F}(\mathrm{V_k}) - \mathrm{F}(\mathrm{V_{k-1}})] \left(\frac{P_{k-1} + P_k}{2}\right) \quad [35]$$

Where Nh is the total number of hours in one year (8769); N is the number of bins; Vk is wind speed normalized and averaged in bin k; Pk is the power output normalized and averaged in bin k. The IEC 61400-12-1 also states that is should be assumed zero power for wind speeds above and below the range of the relevant power curve.

2.8 Wakes

Due to the energy extraction from the wind, WTG farms cause tens of kilometers of atmospheric wakes which results in reduced wind speeds and increase in downstream turbulence intensity of the wind farm (Hasager et al., 2015). For a wind farm that has many WTGs in operation, the

wake of the turbines start to overlap and form a combines wake from the wind farm (Ahsbahs et al., 2020). It is important to take the resulting velocity deficit into account for more accurate energy yield calculations. Wind farm wakes are also known to be dependent of the atmospheric stability (Hansen et al., 2012; Platis et al., 2018). Accurate wake modelling is important for wind plant layout optimalization and is also essential in the work of creating effectual control strategies (Meyers et al., 2022; Veers et al., 2022).

2.8.1 Wake models

2.8.1.1 The Jensen Wake Model

The Jensen wake model is a mass-conserving engineering wake model with its purpose to estimate the downstream wind speed of a WTG at a distance x, u, when subjected to an inflow wind speed at hub height, u_0 (Peña et al., 2016). The model is of popular use due to its reasonably accurate results despict its simplicity (Sebastiani et al., 2021). The normalised velocity deficit using the Jensen model is found as:

$$\delta_u = u_0 \left(\frac{2a}{\left(1 + \alpha \left(\frac{x}{r_1}\right)\right)^2} \right) \quad [36]$$

In this equation, u_0 is the inflow wind speed at hub height; α the wake decay coefficient; and a is the axialy induction factor. Further, the wake expansion radius r_1 can be expressed as follows:

$$r_1 = r_0 \sqrt{\frac{1-a}{1-2a}} \quad [37]$$

Where r_0 is the rotor radius. The axial induction factor a is dependent on the thrust coeficcient, Ct, and can be calculated from their relationship:

$$a = \frac{\left(1 - \sqrt{1 - C_t}\right)}{2} \quad [38]$$

The wake decay constant determines the size of the expanded wake downstream the WTG (Yang and Cho, 2019) and can be determined by using the turbine hub height, h, and the local surface roughness length of the wind farm, z_0, following the formula:

$$\alpha = \frac{0.5}{\ln\left(\frac{h}{z_0}\right)} \quad [39]$$

The model is a good approximation for the near wake, less or equal to two rotor diameters downstream, but not efficient in describing the far wake. The model relies on the assuption that the radial speed within the wake is constant and is expanding radially with the rate k_w (Peña et al., 2016). The Wind Atlas Analysis and Application Program (WasP) suggests a wake decay coeficcient (‘’WDC’’) of 0.04, however, DTU have later found (2018) that a WDC of 0.06 yields more accuracy for offshore conditions (Rathmann et al., 2018). A schematic representation of the Jensen wake model is given in figure 5.

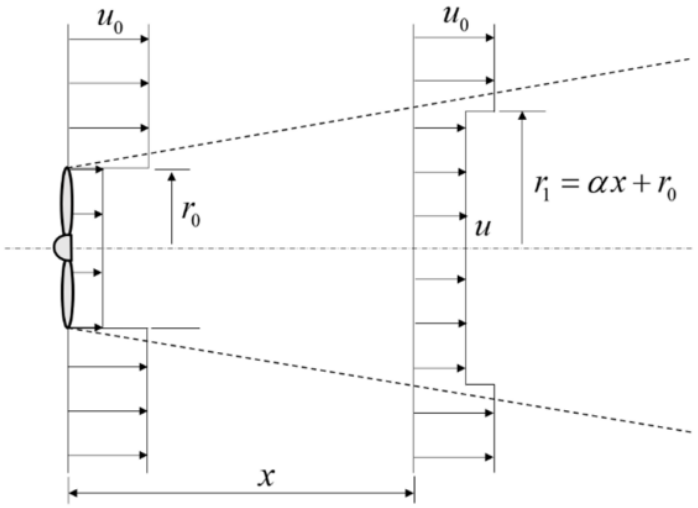

Figure 4: Schematic representation; Jensen wake model (Yang and Cho, 2019).

2.8.1.2 The Eddy viscisity Wake Model (Ainsle Wake Model)

Eddy viscosity hypothesis is a prominent approach for determining the turbulent Reynold stresses in wind turbine wake modeling (Scott et al., 2023). The model is based on the assumption that the flow is axisymmetric, stationary without rotation, and fully turbulent (Sebastiani et al., 2021). These assumptions result in the Euler equations, as expressed by cylindrical coordinates:

$$\frac{v}{r} + \frac{\partial u}{\partial x} + \frac{\partial v}{\partial r} = 0 \quad [40]$$

$$u\frac{\partial u}{\partial x} + v\frac{\partial u}{\partial r} = \frac{v\tau}{r}\left(\frac{\partial u}{\partial r} + r\frac{\partial^2 u}{\partial r^2}\right) \quad [41]$$

In which u and v respectively are the axial and radial velocity components; and where r is the radial position. The Euler equations is solved through a numerical scheme which determines the velocity field inside the wake starting from an initial downstream distance of 2D (Sebastiani et al., 2021). Both the Eddy viscosity and the Jensen wake models have the ability to evaluate the reduction of speed within a wake. However, when several turbines are clustered there is a need for evaluating the combined wake effects. The most common used method for this purpose is the sum of squares (Katic et al., 1986).

2.8.1.3 Wind Farm Model

Inside a WTG farm, local wakes are superposed in the effort to estimate the speed deficit, δ, at the n'th turbine, δ_n. That way, as suggested by Katic et al (1986), it can be applied a quadratic sum of the square of all local speed deficits, sub-indexed i . The method is utilized in WAsP, which is integrated in WindPRO:

$$\delta_{u_j} = \left(\sum_{i=1}^{n} \delta_{u_i}^2 \right)^{\frac{1}{2}} \quad [42]$$

The speed received at the nth turbine, u_n, is then given as $u_n = u_0(1 - \delta_u)$. If the interspace between the local turbine and an upstream turbine is not aligned with the direction of the wind, a partial wake interaction may be experienced by the local turbine (Peña et al., 2016). Partial wake interaction can be visualized in figure 5. The partial wake interaction can be determined as the relationship between the intersecting area of the wake and the rotor area as follows:

$$\delta_u = u_0 \left(\frac{2a}{\left(1 + \alpha \left(\frac{x}{r_1}\right)\right)^2} \right) \frac{A_{overlap}}{A_r} \quad [43]$$

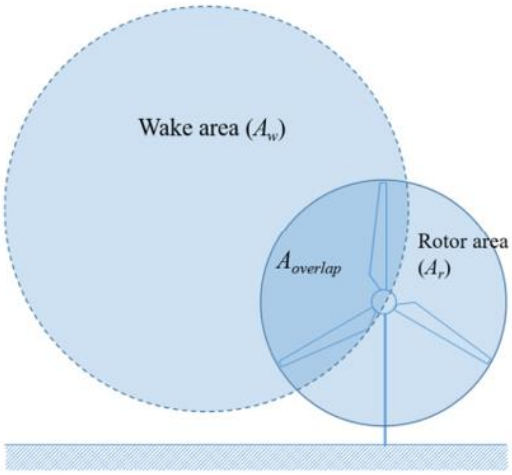

Figure 5: Overlapping wake and rotor areas (Yang and Cho, 2019)

2.9 Model Evaluation – Goodness of fit

In climate, air quality, and meteorology research studies, the root mean square error (''RMSE'') has long been employed as a standard statistical tool to quantify model performance (Chai et al., 2014). The RMSE is the standard deviation of the prediction errors (residuals). It is an effective tool for analyzing how concentrated the data is to the line of best fit (Christie and Neill., 2021). RMSE can be described through the formula:

$$RMSE = \sqrt{\frac{1}{n}\sum_{i=1}^{n} S_i - O_i^2} \quad [44]$$

Where S_i are the predicted variable values; O_i are the observations; and n is the number of observations.

2.10 Climate Reanalysis Data

Reanalysis data sets have increasingly become of interest amongst researchers for large scale wind power analyses, mainly because they cover long time spans and large areas (Rose and Apt, 2015). Long-term wind data is essential for developers and financers of wind projects as it reduces uncertainties about future revenues of proposed wind plants. It is also important for operation and maintenance of existing wind farms as it makes it possible to estimate rare event probabilities. Finally, it gives a a good basis for assessing cycles and trends in wind resource (Rose and Apt, 2015). Reanalysis data is collected through meteorological stations over many

decades and is further combined with today's weather models to deliver a complete and consistent picture of the past weather (Hersbach et al., 2018).

It is shown that mesoscale model data can have some directional bias (Dorrego et al., 2022). In the northern parts of Europe, an observation is that the wind speeds for East and North-East directions is too low, and for South-West they often are too high (EMD, 2023b). A reason for the observed bias might be direction inaccuracies. Often, the measurements can be wrongly calibrated by direction or contain periods with offsets caused by measurement equipment (EMD, 2023b).

2.10.1 NORA3

The three kilometers Norwegian Reanalysis (NORA3) is a 15- year mesoscale hindcast of the North Sea, Barents Sea, and the Norwegian Sea. The nonhydrostatic numerical weather forecast model HARMONIE-AROME, with a horizontal resolution of three kilometers, runs resolved deep convection and produces fields of hindcast that effectively is the downscale of the ERA 5 reanalysis (Haakenstad et al., 2021). The available NORA3 data through EMD download in WindPRO is given in Table 3, and contains the data used for calculation in chapter 6.4.1.

NORA3		
Reference period		01.01.1999 – 31.12.2022
Observation		60 - min averages
Observation heights (m)	Temperature	2
	Relative humidity	2
	Mean wind speed	10, 20, 50, 100, 250, 500
	Wind direction	10, 20, 50, 100, 250, 500.

Table 3: NORA3 data set available through WindPRO

2.10.2 NEWA

The New European Wind Atlas (NEWA) is the descendant of the 1989 European Wind Atlas (EWA, Troen and Petersen, 1989) and is one of the more recent data sets. The data set aims to provide a freely available, high resolution wind energy resource data set for Europe (Dörenkämper et al., 2020) . Offshore, NEWA uses satellite data to validate data at 10 meters above sea level. Furthermore, a validation at 100 meters above sea level is performed by

extrapolating the wind speed at 10 meters by utilizing the log-law relationship (Badger et al., 2016). The available NEWA data through EMD download in WindPRO is given in Table 4, and contains the data used for calculation in chapter 6.4.1.

NEWA		
Reference period		01.01.2009 – 31.12.2018
Observation		30 - min averages
Observation heights (m)	Temperature	100, 200
	Mean wind speed	100, 200
	Wind direction	100, 200

Table 4: NEWA data set available through WindPRO

2.10.3 ERA5

The European Centre for Medium Range Weather forecasts (ECMWF) has long experience with the use of reanalysis data. The ERA5 reanalysis data set is their fifth-generation atmospheric reanalysis and covers the period from 1950 to present date, with a grid resolution of 31 km (Hersbach et al., 2020). The data set provides hourly estimates of atmospheric, oceanic, and climate variables and covers 137 levels from surface to 80km height (Hersbach et al., 2018b). The available ERA5 data through EMD download in WindPRO is given in Table 5, and contains the data used for calculation in chapter 6.4.1.

ERA5		
Reference period		01.01.1990 – 31.03.2023
Observation		60 - min averages
Observation heights (m)	Temperature	2
	Relative humidity	2
	Stability (1/L)	2
	Solar irradiation	2
	Mean wind speed	10, 100
	Wind direction	10, 100

Table 5: ERA5 data set available through WindPRO

3 Software

In this chapter the software and modules that have been used in this thesis will be presented.

3.1 WindPRO

The program used for energy analyses in this thesis is WindPRO, which is a wind resource analysis program developed by the Danish software and consulting company EMD International. The program uses Wind Atlas Analysis and Application Program (WAsP) as calculation engine. The WAsP engine is developed by RISØ and was first introduced in 1987. WAsP's procedure for estimating the wind speed can be described through the wind atlas method (Woo et al., 2012); the method converts the Weibull distribution of the wind data measured into generalized wind statistics. This is done by removing the effects caused by roughness length, obstacles, and the topography. The WAsP engine then makes the assumption that the prediction site and the measurement site are located in the same climatic region, and then applies generalized wind statistics to the site of production (Woo et al., 2012). According to Lars Landberg et al (2003) at offshore locations the controlling terrain parameter is the surface roughness and not orographic effects.

The WindPRO software has a wide range of applications from calculating energy, uncertainty quantifications, wind data analyses, site suitability assessment, to calculating environmental impact. WindPRO is also a strong tool for post construction analyses. WindPRO contains of different modules that handle the different tasks. In this chapter, only the modules and objects used for analyses will be presented briefly. The data input depends upon the module of choice, anyhow, WTG power curve and specification along with meteorological data are required to complete a calculation of the energy output. The meteorological data may consist of actual local measurements that can be imported from a file, or it can be added from third party reanalysis data sets.

Information regarding modules out of scope for this thesis can be found at EMD-international official web page.

3.1.1 Modules and Objects

3.1.1.1 BASIS

The BASIS module is a preliminary module and serves as a backbone for the other WindPRO modules. It gives a graphical user interface of the wind farm project, as well as park information containing turbine layout and spacing.

3.1.1.2 PARK

PARK is a flexible tool that is used in calculation of the Annual Energy Production (‘’AEP’’) for one or several wind farms. The module combines flow and wake models together with the site data to determine the energy yield of the WTG-s. Multiple sets containing wind data can be used in a PARK calculation. The module takes by default the nearest set of wind data unless else is specified (Nielsen, 2016)

3.1.1.3 Measure Correlate Predict

The Measure-Correlate-Predict (MCP) module is a tool for long time correction of local wind data and is based on the correlation with long-term reference data. This module is proficient when comparing graphs and determining correlation between local data and reference data. The module makes it possible to long-term correct the local measurements with a long-term reference by applying time-shifts and filling gaps. The MCP is a very powerful tool when you have a sound amount of data that contains gaps and out of range values and you need to correct it to a coherent time-series. When the data quality is very low for your local measurements, the MCP module can be utilized purely as a comparison tool. For this instance, you want to scale meso-scale data to your local measurements. This is an iterative process, and the MCP module can be used between iterations to see the current correlation between the reference data and local data (Jogararu, 2018).

3.1.1.4 Performance Check

Performance check is a set of tools used to analyse wind turbine SCADA data. The module has the ability to quantify losses, lower the AEP uncertainty, and improve pre-construction estimates. The analyses is based on error codes typically retrieved from SCADA, or by user specifications if SCADA does not contain error codes.

3.1.1.5 METEO Object

WindPRO offers a range of different objects that carries different data and is placed in the project. A METEO object serves as a point of measuring that holds measurement data. This can be local measurements (e.g., LiDAR or mast), or reference data from meso-scale data.

3.1.1.6 AREA Data

Tool for digitizing and importing areas as closed polygons, each with similar characteristics. The sea surface is described using the Area object.

3.1.1.7 WTG Area

The WTG Area Object is used together with the PARK module and defines the area that is used to cite the WTG's. All the WTG-s in the wind project that are used for analyses are linked to this object.

4 Current research

4.1 Previous studies at Westermost Rough wind farm

The Westermost Rough (WMR) wind farm has been a popular location for studies related to wake generation because of the turbine layout and geographical location. Nygaard et al (2018) presented dual-Doppler measurements of the wake generated behind the WMR wind farm. Through radar measurements they were able to track the evolution of the wakes through the farm and further downstream. The study found through measurements that the wake region extends at least 17 km downstream WMR. The measurements were then compared with two different engineering wake models, the top-down wake model and the Park model. Both models predicted correctly up to 10km behind WMR. The Park model does not consider shift in wind direction behind the wind farm and thus overestimated the wind speed on lines aligned on the turbine rows. Two years later Nygaard et al (2020) presented two new models for wind turbine interactions effect including a recipe for combining them. The first being an extension of the Park model which incorporates both the atmospheric turbulence, and the turbulence generated in the wake itself. This modified model proved a better fit to describe wake recovery over longer distance which is beneficial when considering wake effects from neighboring wind farms. Ahsbahs et al's (2020) recent work showed a good agreement between Doppler radar measurements and SAR images at WMR in cases without any stable atmospheric stratification.

4.2 Reanalysis data

Haakenstad et al (2021) did a performance study of the NORA3 reanalysis data set where they compared surface wind speeds assured from offshore observing stations that was retreived from the Norwegian Meteorological Institute, and made an comparison to NORA10 and ERA5. The validation period was 2004-18. The best-performing reanalysis data set was NORA3, followed by NORA10. The least-performing data set was ERA5.

Solbrekke et al (2021) did a validation study of NORA3 for the Norwegian Sea and the North Sea during the period 2004 – 2016. They conclude that the NORA3 data set is well suited for estimating the wind power but gives a rather conservative estimate on the offshore wind metrics. They found that the NORA3 wind speeds typically is 5% lower than actual wind speeds, which gives an offshore wind power underestimation of 10-20%.

4.3 Wake models

There are different wake models being used to calculate the energy deficits in wind modelling. Both the Jensen and the Eddy viscosity are engineering wake models that are is simpler and require less computational power than more advanced models.

Shakoor et al (2016) did a comparative study of different wake models offshore, including the Jensen and the Eddy viscosity model. They conclude that both models have the possibility of high errors in accuracy compared to real measurements.

Vanluvanee (2006) compared the practical aspects and simulation results from three different wake models: the Eddy viscosity, Larsen, and Jensen wake model. They found that the Eddy viscosity model showed high prediction accuracy for measurements on the wake width for larger down-stream distances, while Jensen outperforms the Eddy viscosity model for shorter distances.

Sørensen et al (2006) did a validation of the wake model performance for large offshore wind farms where they present the results of a case study done at Horns Rev wind farm from 2005 to 2006 using WindPRO, and the calculated wake losses are compared to actual observed wake losses. The case study indicated that the Jensen wake model was more precise in predicting the wake loss observed than the Eddy viscosity model. Their main results concluded that the Jensen wake model with a wake decay coefficient of 0.04 is more conservative than the Eddy viscosity model.

4.4 Wind Profiles

Gryning et al. (2007) discovered, through examination of meteorical readings from a 160-meter mast at Høvsøre in Denmark, and a 250 meter tall TV tower in Hamburg in Germany, that wind profiles that are based on surface-layer theory and Monin-Obukhov scaling are only valid up to 80 meters for neutral atmospheric conditions, and fairly less for adiabatic atmosphere. Above 80 meters, deviations occurred progressively. With technological advances wind turbines become larger and the turbine hub height will be positioned outside the limitations of what Monin-Obhukov scaling is valid for, necessitating the extension of wind profiles.

4.5 Rotor Equivalent wind speed

Ryu et al (2022) did an analysis of the vertical wind shear effects on the prediction accuracy in offshore wind energy production, applying the the rotor equivalent wind speed. The analysis was conducted for the Anholt offshore wind farm using two years of SCADA data and compared the two methods to actual power output. They concluded with REWS being more accurate at predicting the higher wind speeds and had a more accurate prediction than the HHWS. Overall, the REWS method showed better prediction accuracy than the HHWS.

5 Materials and Methods

5.1 The Westermost Rough Wind Farm

The wind farm studied in this thesis is the Westermost Rough wind farm in England operated by Ørsted, the largest offshore wind farm developer in the world. The WMR wind farm is a medium sized offshore wind farm situated at the southeast coast of England, eight kilometers off the Holderness coast, and has a covering area of $32km^2$. The wind farm consists of 35 turbines of the type Siemens-Gamesa SWT-6.0-154 and has the potential to yield a combined total capacity of 210 MW (Ørsted, 2015). The turbines have a monopile substructure each weighing up to 800 tons and has a diameter of 6.5m. Figure 6a displays an overview of the park, whereas figure 6b displays the wind farm layout. Internal spacings between the turbines can be found in Appendix 3 fig. 49, and table 34.

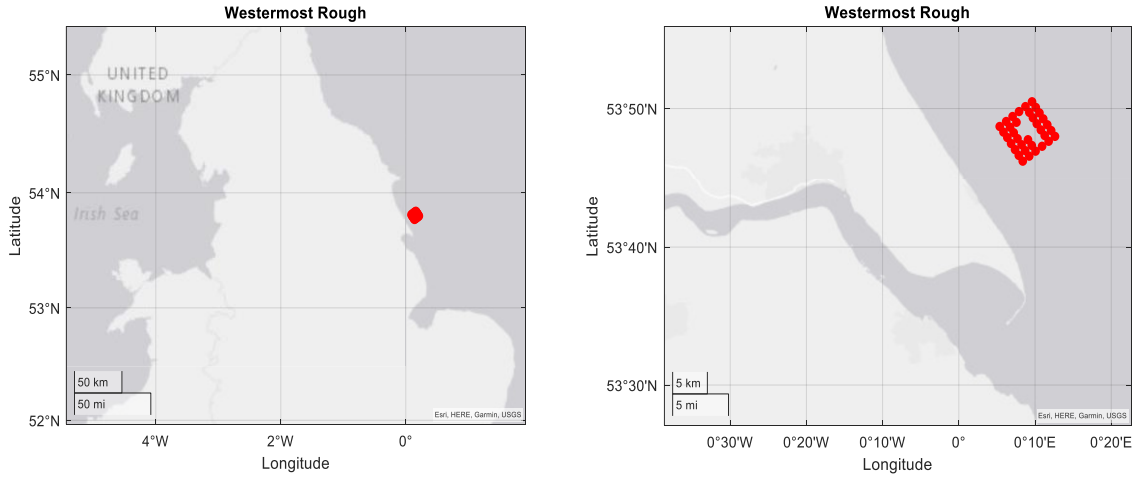

(a) (b)

Figure 6: Overview of WMR wind park (a); enlarged overview WMR wind park with field layout (b).

Westermost Rough Project Timeline (Ørsted)	
May 2007	Awarded leasing agreement to develop a wind Farm at WMR.
Nov. 2011	Consent awarded.
Feb. 2013	Onshore construction began.
Jan. 2014	Offshore construction began.
Aug. 2014	First turbine erected.
Sep. 2014	First power generated.
Jul. 2015	Fully commissioned and Operational.

Table 6: Westermost Rough Project Timeline. Ref: (www.orstedcdn.azureedge.net).

The WMR project was the first commercial deployment of the Siemens-Gamesa SWT-6.0-154 wind turbines (Ørsted, 2015), and the project timeline from awarded leasing agreement to fully commissioned and operational is given in table 6. The turbines stand 177m tall from sea level to the highest reach of the blade tip. The wind farm specifications can be found in table 7. The Siemens Gamesa SWT-6.0-154 technical parameters are provided in table 8.

Item	Content
Wind Turbines	Siemens-Gamesa SWT-6.0-154
Number of turbines	35
Nominal Power [MW]	6
Hub Height [m]	106
Rotor diameter [m]	154
Water depth [m]	16-26
Distance to shore [km]	8
Wind farm area [km^2]	32
Power regulation	Pitch regulated, variable speed

Table 7: Technical specification SWT-6.0-154. Ref: (https://www.siemensgamesa.com/products-and-services/offshore/wind-turbine-swt-6-0-15).

The Siemens Gamesa SWT-6.0-154 turbine parameters from datasheet	
Content	**Value**
Rated power	6,000,0 kW
Cut-in wind speed	4.0m/s
Rated wind speed	13.0 m/s
Cut-out wind speed	25.0 m/s
Survival wind speed	70.0 m/s
Rotor speed, max	11.0 U/min
Tip speed	89 m/s

Table 8: Siemens Gamesa SWT-6.0-154 Datasheet. Ref: (https://en.wind-turbine-models.com/turbines/657-siemens-swt-6.0-154).

5.1.1 Offshore Wind Lidar

Average wind speed increases with height and reduces the braking effect of ground-based barriers. For this reason, turbine hub heights increase in elevation in order to exploit the resources which can be found at higher altitudes. State of the art wind turbines now have hub heights of 120 to 160 meters, and the rotary blades may reach as high as 200 meters at blade tip. When planning a wind project this can be challenging as the towers used for wind measurements seldom exceeds 100 meters altitude. Doppler LiDAR systems has been introduced in wind resource assessment as they are very precise in measuring air movement and fluctations at higher elevations. The WindCube LiDAR rotates a laser beam in cone shape using pulsed heterodyne technology. The wind speeds and direction are determined by detecting the Doppler shift of the laser.

At the WMR wind farm the LiDAR is of the model type WindCube manufactured by Leosphere, and is installed on the roof deck of the offshore substation Z01 at a height of 33.8 m from the Lowest Astronomical Tide (LAT). The data received from the LiDAR is given in 10 minutes average observation during the reference period 13 January 2016 to 6 December 2017. For calculation purposes in this study the height has been assumed to 34 meters. Table 9 contains description and content available from the wind cube at WMR. The location of the substation Z01 is depicted in figure 7.

Description		Content
Type		Leosphere WindCube
Observation		10-min averaged
Accuracy		0.1m/s (speed), 2 degrees (dir)
Reference period		2016.01.13 – 2017.12.06
Height above MSL† [m]		33.8 (34 for analysis)
Location GPS		Roof deck Z01 sub-station
Observation height [m]	Wind speed	40, 60, 70, 80, 100, 120, 140, 160, 180, 250, 270, 290
	Wind dir*	40, 60, 70, 80, 100, 120, 140, 160, 180, 250, 270, 290
	Air Pressure	33.8
	Air temperature	33.8
	Relative humidity	33.8

Table 9: Content description of the Leosphere WIndcube located at WMR substation Z01.

† To correctly calculate height above Lowest Astronomical tide (LAT), the height of the LiDAR lens must be considered (33.8 m above LAT). For example: if the configured measuring height is 10m, true height of measurement is 43.8 m above LAT.

* Wind direction for every measuring height must be corrected according to the offset value (direction between LiDAR reference angle 0 and north), which depending on when the measurement were taken, is +4deg and -129deg.

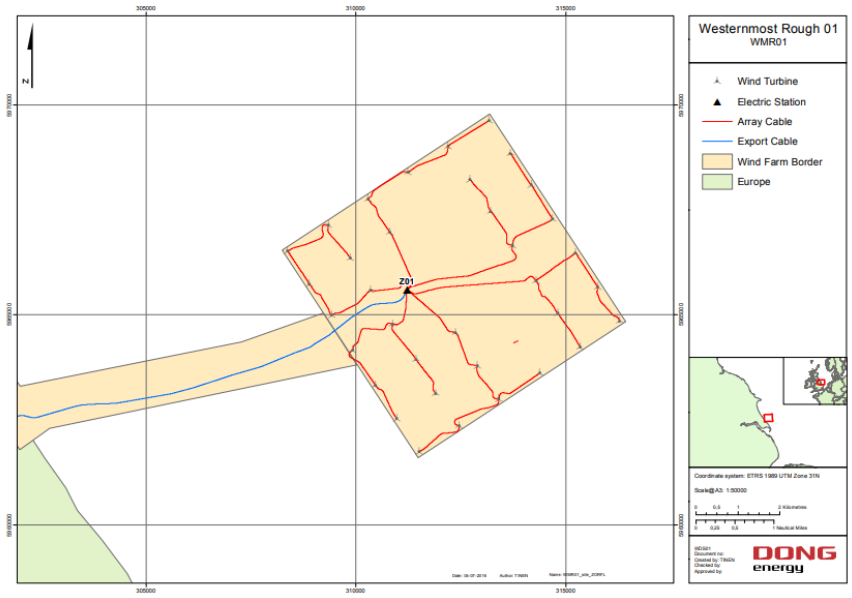

Figure 7: Lidar location on roof deck of substation Z01. Ref: (Westermost Rough Lidar documentation report – Dong energy, prepared 25 May 2016)

5.1.2 Offshore Buoy

Inside the WMR wind farm a wave buoy manufactured by Fugro Oceanor of the model SEAWACTH Midi is installed. The data retrained from the buoy is given in table 10.

Description		Content
Type		SEAWATCH Midi
Observation		30-min averaged
Sampling period		2016.01.01 – 2017.12.31
Location		53°50.250'N, 000°09.500'E
Observation depth [m]	Current direction	2, 3, 6, 9, 12, 15, 18, 21, 24, 27, 30, 33
	Current speed	2, 3, 6, 9, 12, 15, 18, 21, 24, 27, 30, 33
	Water temperature	Sea surface

Table 10: Buoy data SEAWATCH Midi

5.2 Data Quality and Filtering

With different data sources covering different measurement periods this thesis uses the period 2016.01.13 – 2017.12.06 as the reference period. This period serves as the reference period as it is the shortest of all the different data sources (LiDAR).

5.2.1 LiDAR

Due to the position of the LiDAR, the wind observation does have the potential to be distorted as wake generates downstream of a wind turbine. All the data is handled in separate collumn vectors and sorted to have the same start and end date, and follows the same time step. SCADA data contained double sampling of june 2017 which had to be removed in order to align the data. The oceanographic data attained from the buoy are stored as 30 minute averages which for more detailed measurements is interpolated to 10 minutes observations. During the reference period 13 January 2016 to 6 December 2017, the LiDAR data had some significant deficiencies, and it is natural to assume that it was out of service for longer stretches during the reference period. 100% 10-min average samplings calls for 99775 measurements while our dataset only contains about 11256 measurements of windspeed (each height), 11437 measurements of temperature, and 11256 measurements of direction (each height), hence a data quality of 11.28 – 11.46%. Figure 8 shows significant gaps in the wind speed time series at hub height.

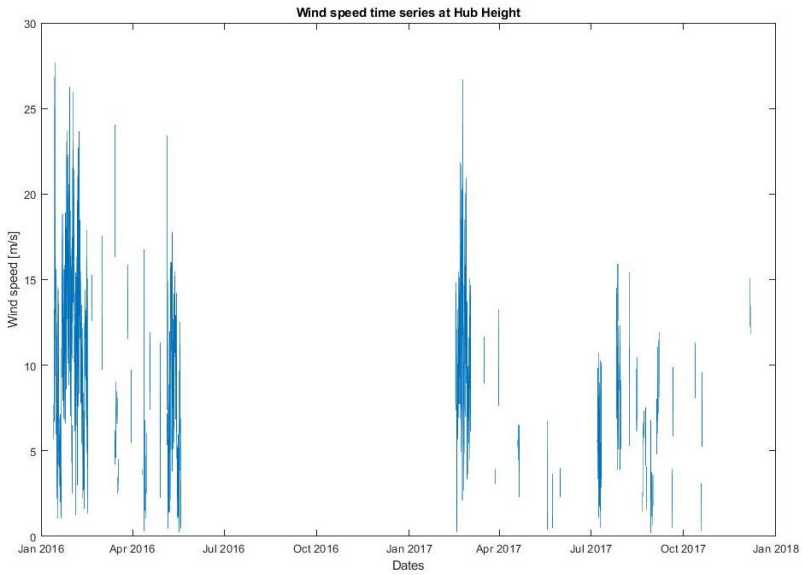

Figure 8: Wind speed time series LiDAR at hub height (106m)

Following Obhrai et al (2012), the data was filtered in order to remove non-stationary conditions which conformed the three criteria: i) a variation in temperature more than 0.5C, ii) a variation in wind speed of more than 10% and iii) a change in wind direction of more than 10 in between consecutive values. For stability calculations, windspeeds lower than 2 m/s along with negative air and sea temperature were filtered out from the dataset. The data quality before and after filtering using Obhrai 2012 is presented in table 11. Due small deviations in quality among the different turbines, only wind speed and direction for 106m is presented, however, the filtering is applied to all heights. The wind rose for the hub height pre- and post-calibration is depicted in figure 9 and 10 respectively.

Data description	Pre-filtering	Post-filtering	Filtered [%]
Wind speed (106 m)	11256	10134	9.97%
Wind direction (106 m)	11256	10241	9.02%
Air temperature	11437	11134	2.65%

Table 11: data quality pre and post-filtering.

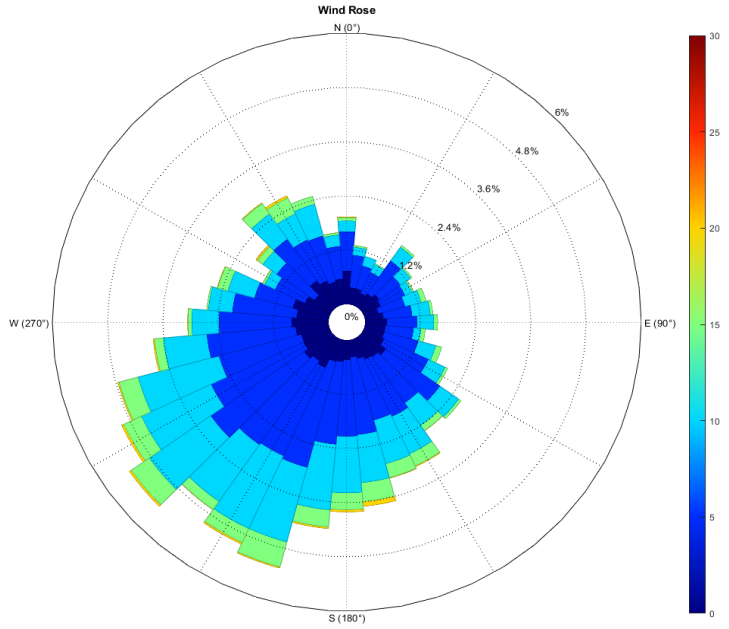

Figure 9: Wind Rose at hub height before filtering. Based on 11256 measurements of 10-min averages during the reference period.

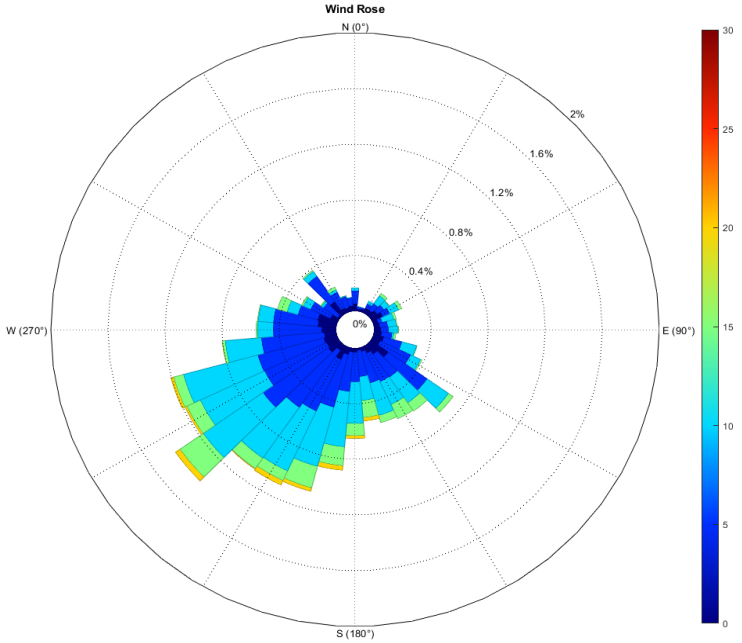

Figure 10: Wind Rose at hub height after filtering. Based on 10134 measurements of 10 min-averages during the reference period.

5.2.2 Buoy

The Buoy data set containing water temperature had some significant outlier data which was filtered and smoothed as it does not experience critical diurnal changes. The data from the buoy was given in 30-minutes measurements which was interpolated to 10-minutes measurements. The smoothed data gives us 99775 10-minutes measurements of water temperature during the reference period. The wave height and direction measurements had very few outliers and had a data quality of 98.64% during the reference period. A wave rose is depicted in figure 11.

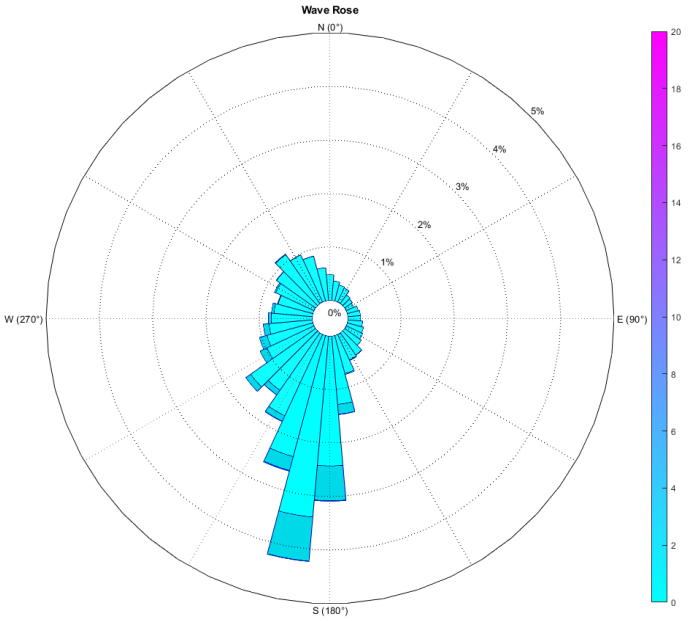

Figure 11: Wave rose during the reference period based on 98418 measurements.

5.2.3 SCADA data

The SCADA data had great consistency for all the turbines. There were no significant deviations in the data availability between the different turbines, however, most of the turbines had a double sampling of June 2017 which had to be removed. Because of low deviations the following data availability for the A01 turbine, presented in table 12, can be assumed approximate equal, and representative for all turbines.

Data	Number of samples	Available samples	Availability [%]
Wind Speed	99775	97370	97.59
Wind Speed standard dev.	99775	97370	97.59
Mean active power output	99775	97396	97.62
Ambient Temperature	99775	97371	97.59
RPM	99775	97370	97.59
Pitch position	99775	97370	97.59
Yaw position	99775	97370	97.59

Table 12: representation of available data thorugh turbine A01 SCADA during the reference period.

Figure 12 and 13 display the wind speed density from the A01 SCADA data fitted with different distributions. The Weibull parameters are given in table 13.

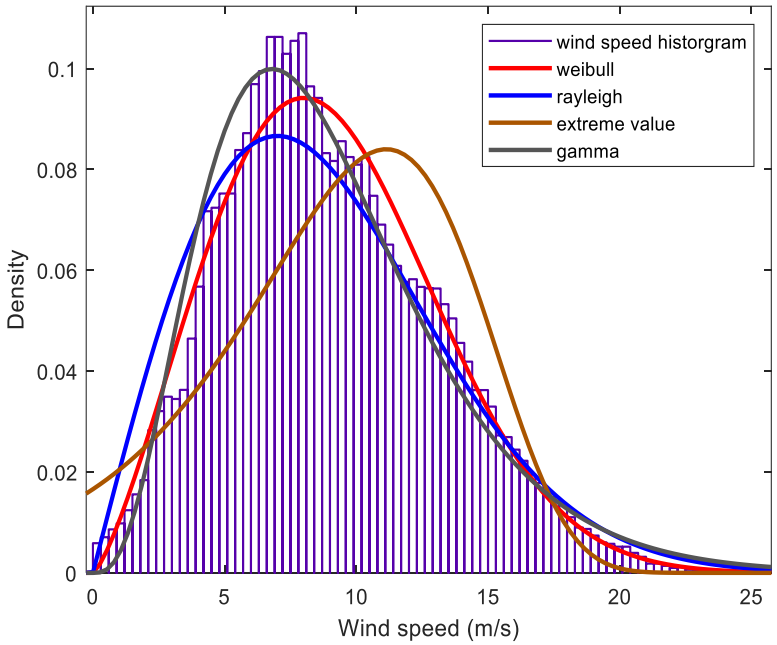

Figure 12: Different distributions fit to the SCADA wind-speed for the A01 turbine.

Parameter	Value
Estimated scale parameter:	10.1687
Estimated shape parameter:	2.3357
95% Confidence interval for scale parameter:	[10.1373, 2.3233]
95% Confidence interval for shape parameter:	[10.2002, 2.3482]

Table 13: Two-parameter Weibull parameters.

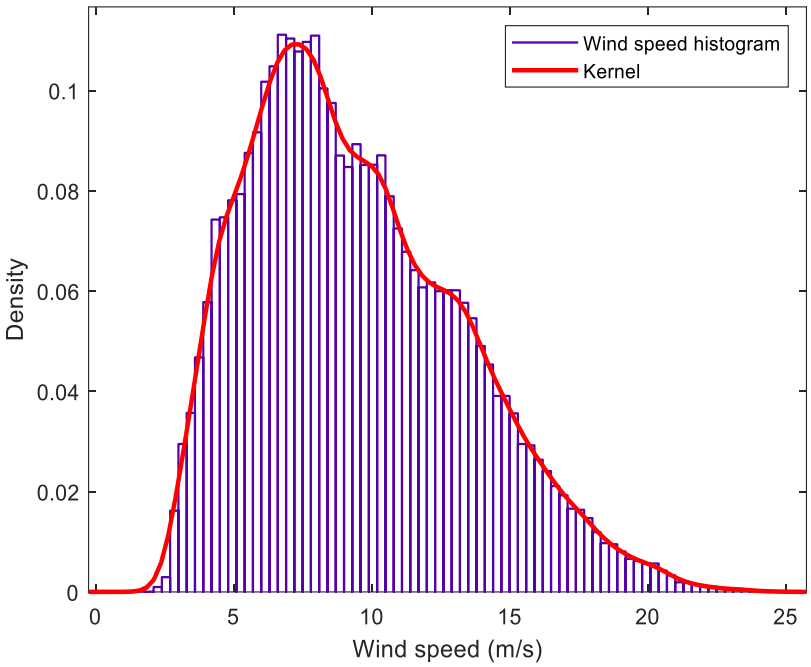

Figure 13: Kernel distribution fit to SCADA wind speed for turbine A01

6 Results

6.1 Stability

In determination of the atmospheric stability at WMR both the Bulk Richardson number and Gradient Richardson number were used for comparison. Since the only measure for temperature we have is at the same altitude as where the LiDAR is positioned (34m), the temperature from the turbine C03 SCADA data had to be used in order to get temperature from two altitudes in order to calculate the gradient Richardson number. The turbine C03 was chosen as it is located closest to the LiDAR and we can assume little variation in temperature between the C03 to the LiDAR, for a complete overview of the wind farm with labeled turbine numbers see Appendix 3, figure 49. Figure 14 shows the stability for different heights normalized to the lowest measuring height, 74m, where the right hand side contains stability measure using gradient richardson, and left hand side for bulk richardson. The data used in analysis is the post filtered LiDAR data as presented in chapter 5.2.

Bulk Richardson **Gradient Richardson**

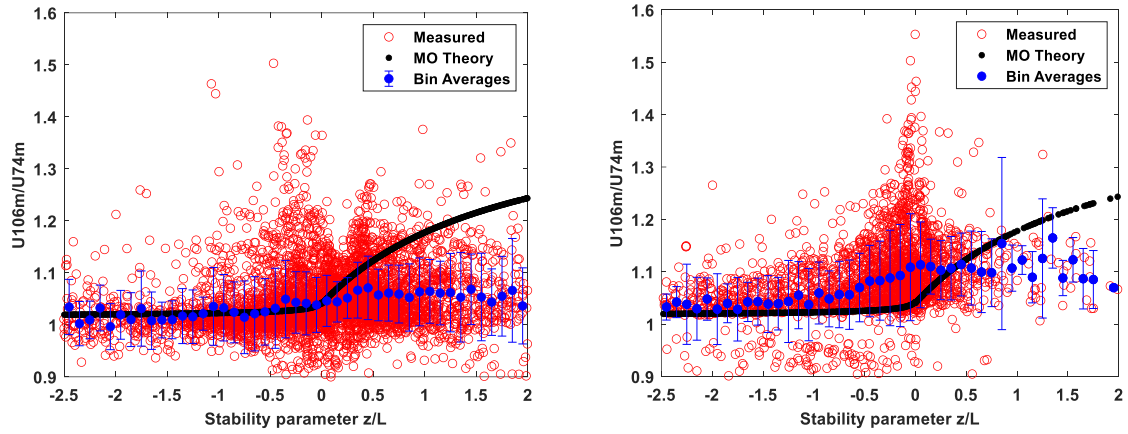

(a) (b)

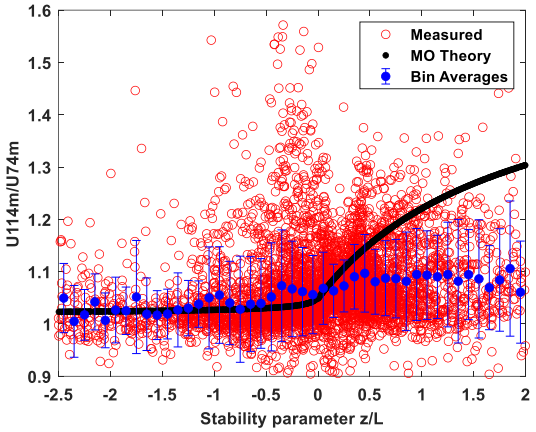

(c)

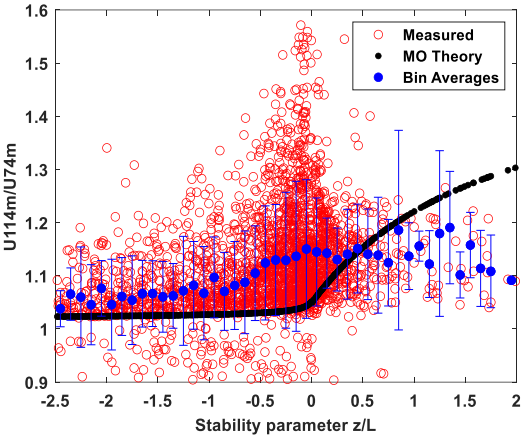

(d)

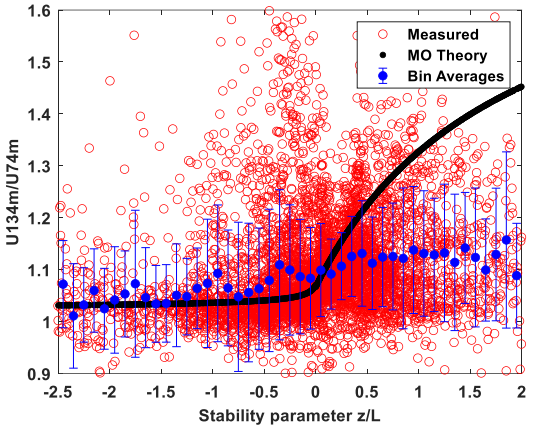

(e)

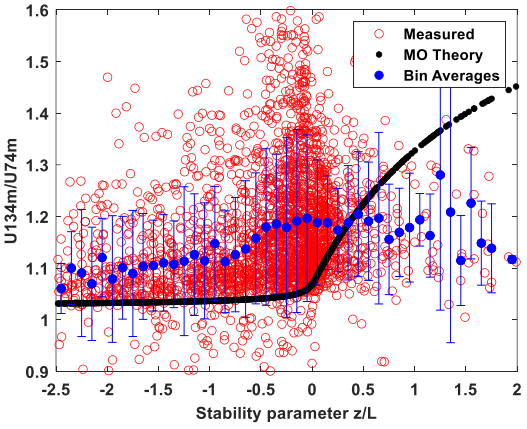

(f)

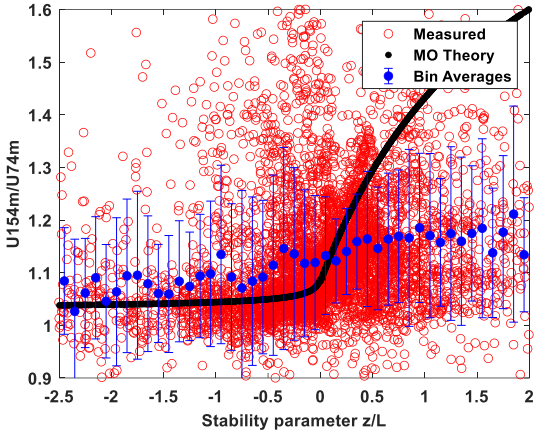

(g)

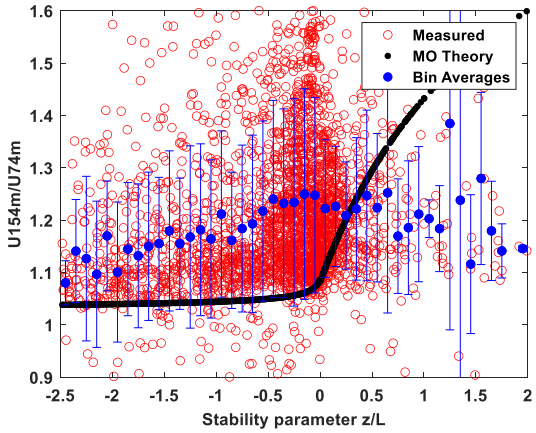

(h)

Figure 14: Comparison of bulk richardson (B) to gradient richardson (G); B U106m/U74m (a); G U106m/U74m (b); B U114m/U74m (c); G U114m/U74m (d); B U134m/U74m (e); G U134m/U74m (f); B U154m/U74m (g); G U154m/U74m (h).

The root mean square error (RMSE) for (a) to (h) is presented in table 14.

Height (m)	Bulk	Gradient
106	0.0609	0.0668
114	0.0813	0.0886
134	0.1093	0.1225
154	0.1378	0.1641
174	0.1658	0.1999
194	0.1961	0.2405

Table 14: RMSE comparison Bulk Vs Gradient method using 45 bins.

6.1.1 Turbulence

The wind speed is normalized at 74m and sorted into stability classes using the gradient Richardson number and wind speed distribution for each stability class is determined. Figure 15 and 16 shows the turbulence intensity and the 90th percentile turbulence at hub height respectively.

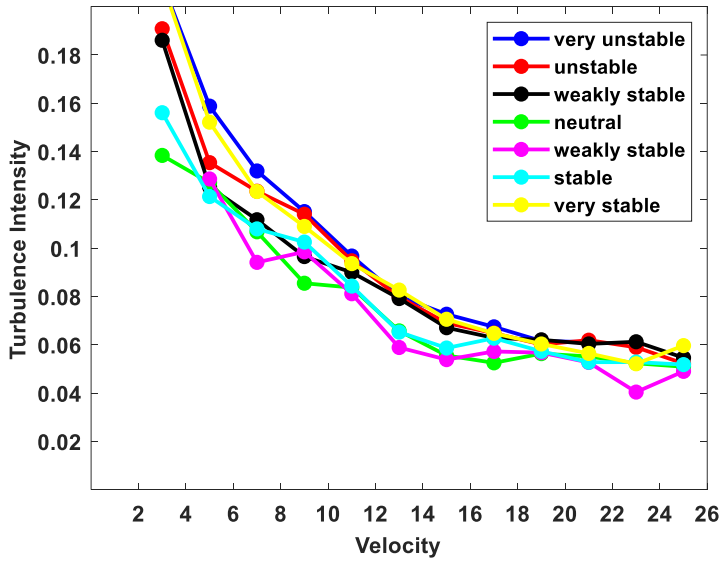

Figure 15: Turbulence intensity for different stability classes at hub height (106m)

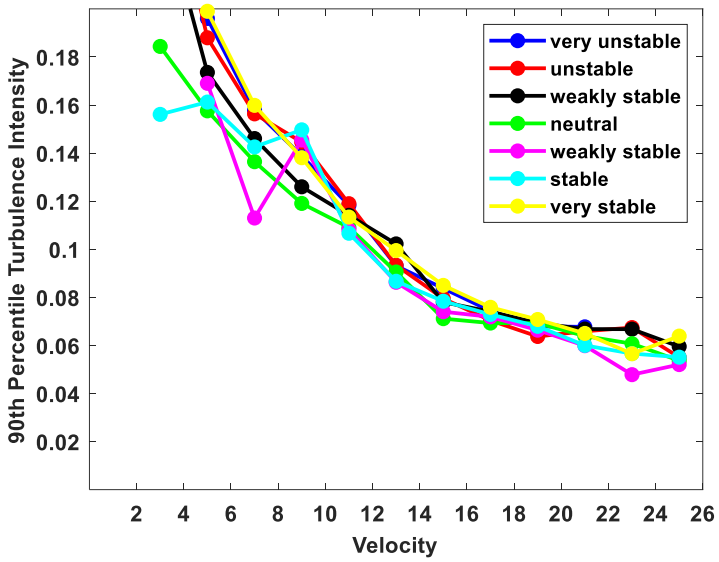

Figure 16: 90th percentile turbulence intensity for different stability classes at hub height (106m)

6.2 Power Calculations Using LiDAR data

The second objective of this thesis was to apply the hub height wind speed and rotor equivalent wind speed to the LiDAR data and compare the energy output to the actual energy generated in the SCADA data. For this calculation turbine C03 was chosen as reference turbine as this is the turbine placed closest, adjacent, to the LiDAR and it is assumed that the turbine experiences the same wind as the LiDAR. The calculations in this sub-chapter will be conducted for one turbine only, C03. The power curve used for this calculation is presented in-depth in chapter 6.3 ‘’Power Curve Correction’’. Because of large gaps in the LiDAR data during the reference period, the longest period with coherent LiDAR data was used for analyses and spans from 13 January 2016 to 17 February 2016 (figure 17) and contains 4884 10-minutes measurements. A sectionally binned representation of the wind speed and direction is given in figure 18.

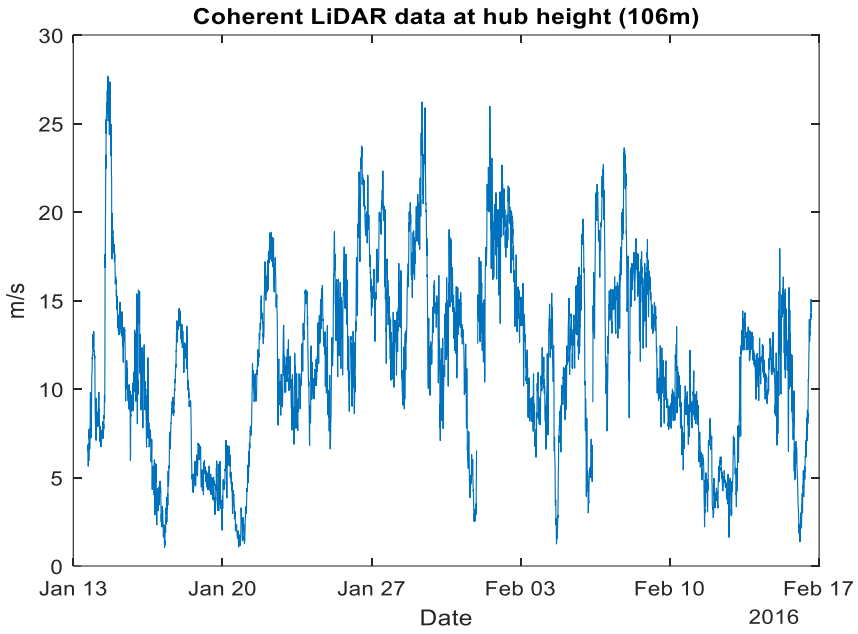

Figure 17: LiDAR wind speed at hub height from 13.01.2016 to 17.02.2016 based on 4884 10-min measurements.

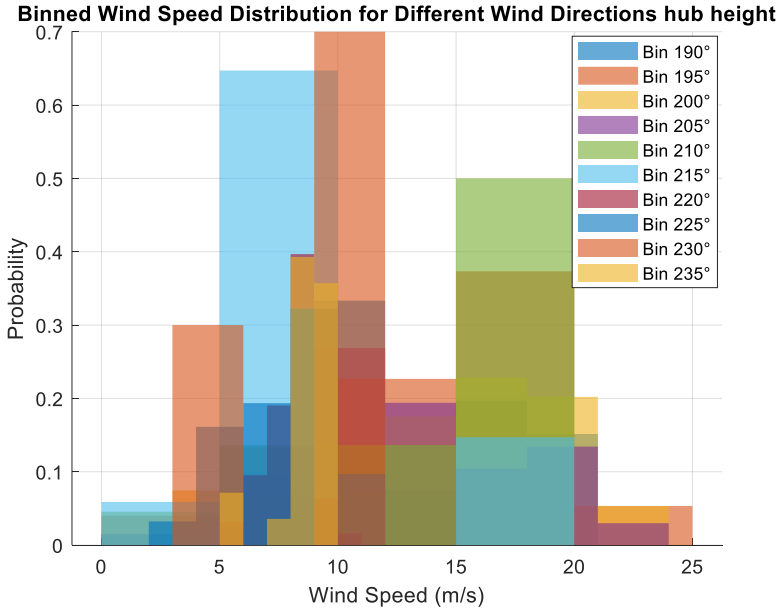

Figure 18: sectionally binned wind speeds based on 4884 10-min measurements with 0 degrees being North.

The turbine rotor was split into five segments with equal distance to each other, with the lowest centre (U1) being 44.4 meters above sea water level (‘’SWL’’). The sections are determined in accordance with Chapter 2.7.2 . The five sections of the area (A1-A5) are used to weight the wind speeds at the area centers. Figure 20 displays the WTG rotor with segment centres. Table 15 shows the segment details after splitting in accordance with equation 32 and 33. It should be reminded that the distance from SWL to the rotor tip at the bottom is 29 meters.

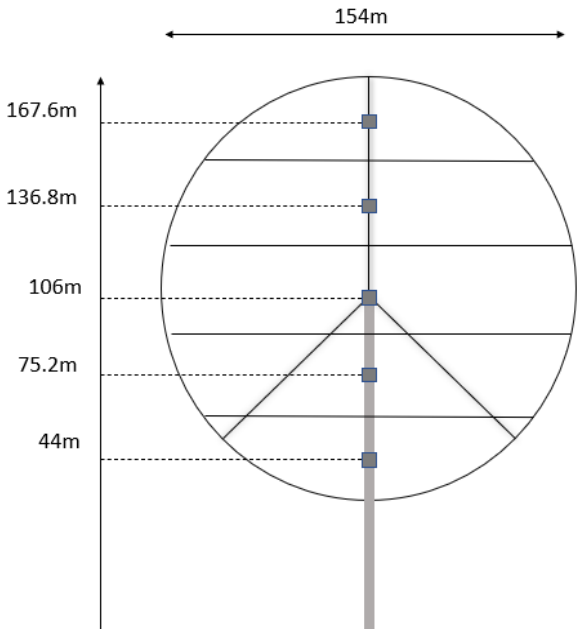

Figure 19: Rotor split into segments

Segment	wind speed height [m]	segment weighting [%]	segment bottom [m]	segment top [m]	segment height [m]	Wind Speed [m/s]
A5	167.6	5.20	152.2	183	30.8	11.4762
A4	136.8	25.23	121.4	152.2	30.8	11.1477
A3	106	39.13	90.6	121.4	30.8	10.7482
A2	75.2	25.23	59.8	90.6	30.8	9.5449
A1	44.4	5.20	29	59.8	30.8	8.1572

Table 15: Segment details.

The rotor equivalent wind speed is then determined by utilizing equation 31. For power output calculation we use the power curve which will be described in the next chapter (chapter 6.3). Table 16 gives the power output determined by using REWS, and HHWS compared to actual production for the period.

Method	Energy [MWh]
Hub height wind speed	4 281
Rotor equivalent wind speed	4 473
SCADA	4 900

Table 16: Power output the period 13 Jan – 17 Feb 2016.

6.3 Power curve correction

One of the objectives of this theses was to compare a ‘’real power curve’’ obtained through SCADA data and MAF as described in chapter 2.6.1, to standard turbine specific power curve. After filtering the SCADA data through equation 25, we want to determine the filter output through equation 24. The critical problem when using the MAF filters is to determine the filters window length. The filter window should be appropriate in length to compare trends in wind speed change and power change. In the determination of correct length of window through iteration, we choose one week of SCADA data as reference (1008 10-min samples). It should be noted that one week of data is rather arbitrary, but as long as the window is long enough to clearly see trends and patterns in the data, which is the main objective, it is considered sufficient. The MAF with chosen window length is then applied to the whole reference period. Here, the turbine A01 is used as the reference turbine. Figure 20 to 22 shows the filtered wind speeds with different window lengths. The basis for choosing A01 is explained in chapter 1.1.

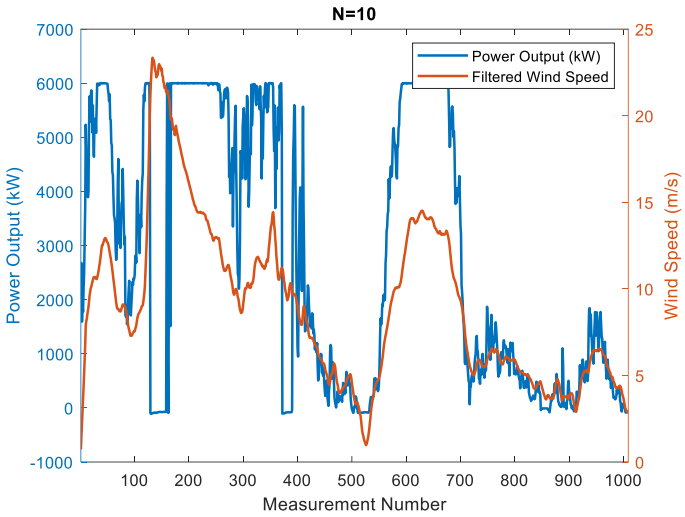

Figure 20: MAF with filter window length N = 10 during a one week period.

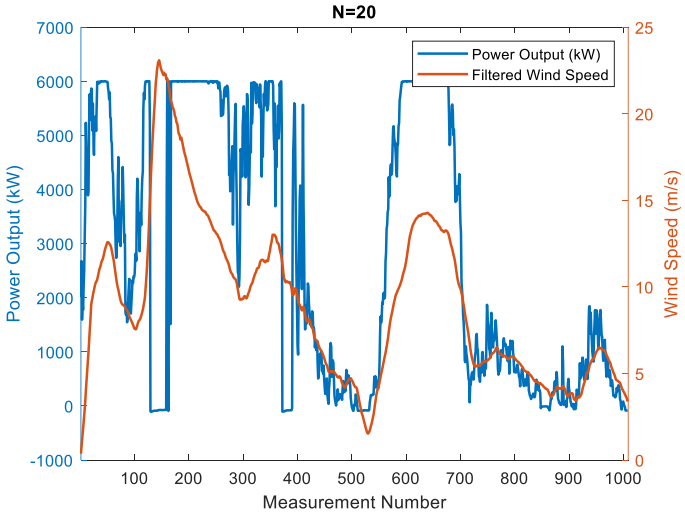

Figure 21: MAF with filter window length N = 20 during a one period.

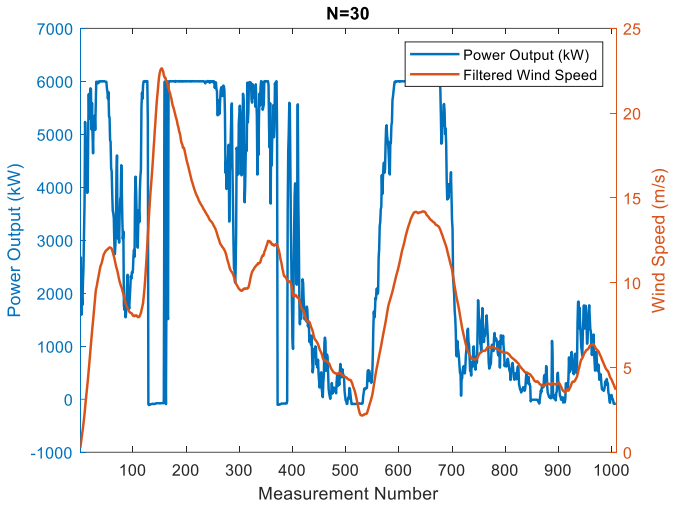

Figure 22: MAF with filter window length N = 30 during a one week period

After filtering, the wind speed fluctuations are reduced. The magnitude of reduction depends on the filter length of choice. There is good consistency of trend in wind speed and power. Dai et al (2022) stresses that the window length value only serves as an approximate value due to the wind conditions complexity, and that it is not that the longer filter window length, the better. But a smaller window length as long as the consistency of trends is present is favourable. That is why in this theses we proceed with a window length of N = 10.

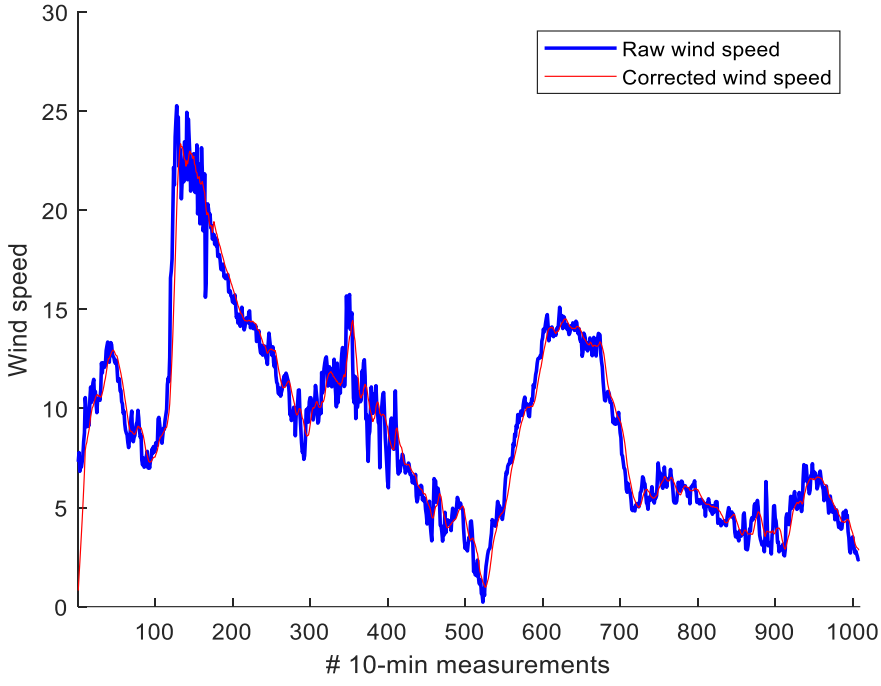

Figure 23: comparison raw wind speed (blue) and corrected wind speed through MAF with filter length N = 10 (red).

We can tell from figure 23 that the wind speed fluctuation has been reduced as a result of the filtering, and the filtered wind speed has a small delay in time when compared to the raw wind speed. This delay slightly increases with the increase of window length, N. According to the momentum theory of an ideal WTG and combined with the anemometer installation position, the difference between the measured and actual wind speeds is roughly compensated. Proceeding to model the power curve only a scatterplot can be obtained from SCADA data. For this reason, various fitting forms were tested using the curve fitting toolbox in MATLAB, including Polynomial fit (figure 24), Fourier fit (figure 25), sum of sine (figure 26), and Gaussian fit (figure 27). The figures 24 – 27 contains all yaw angles.

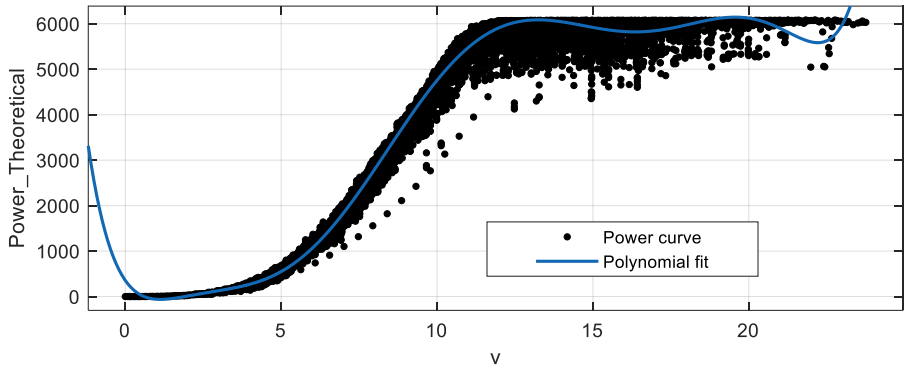

Figure 24: Corrected power curve with polynomial fit.

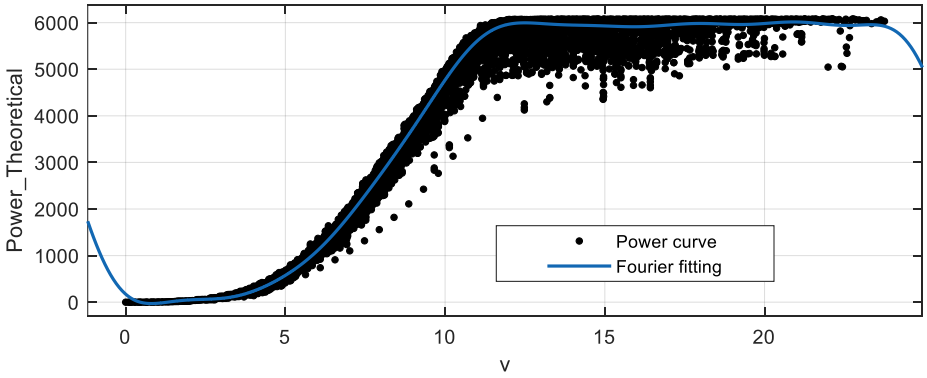

Figure 25: Corrected power curve with fourier fit.

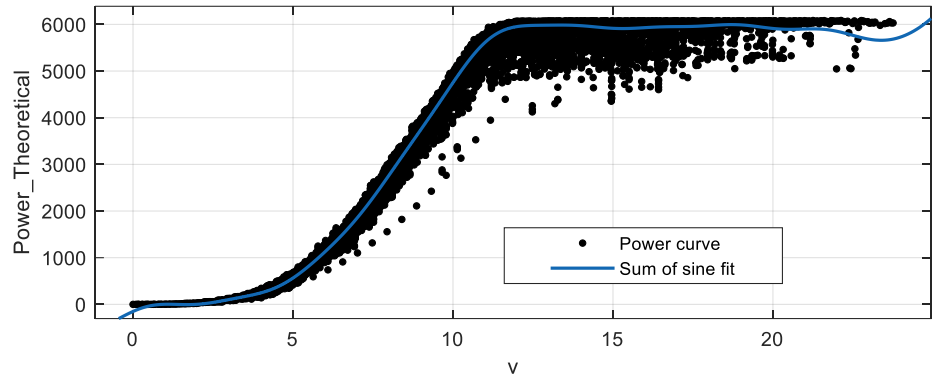

Figure 26: Corrected power curve with sum of sine fit.

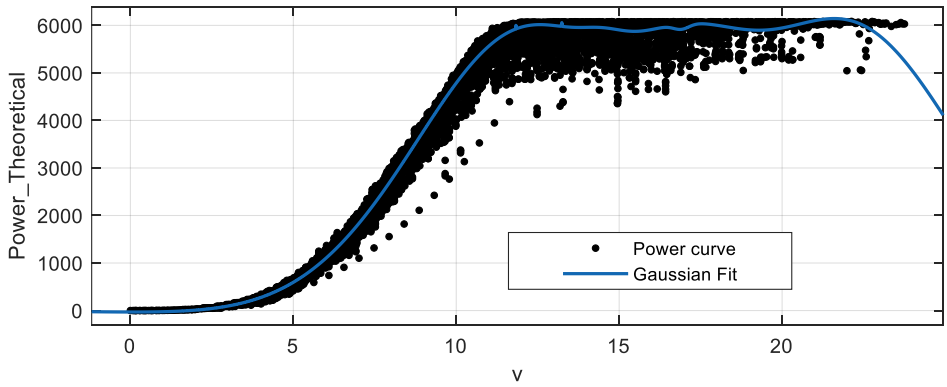

Figure 27: Corrected power curve with Gaussian fit.

The different fits were then analysed together with the raw fitted power curve (only applied the filtering, no MAF) (figure 28) in the curve fitting toolbox. Table 17 presents the goodness of fit for the raw power curve and the corrected power curve fitted with Fourier fit, which showed the best fit.

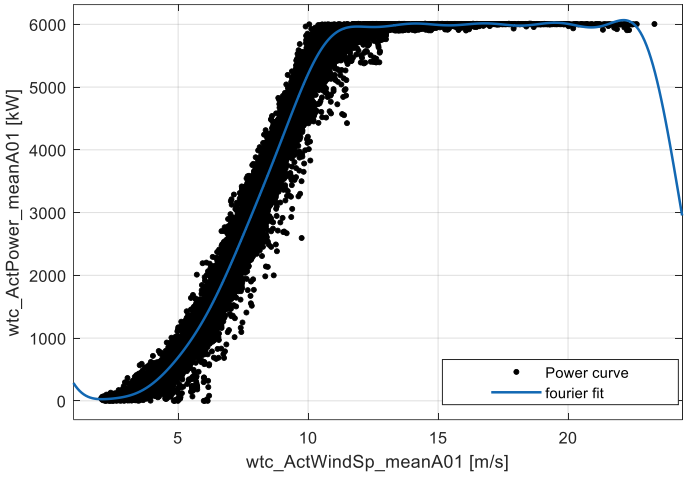

Figure 28: raw power curve with fourier fit.

	Coefficients	Power curve corrected	Power curve raw SCADA
a0		3859 (3833,3885)	4010 (3932, 4089)
a1		-1175 (-1215,-1135)	-1832 (-2069, -1596)
b1		2949 (2917, 2980)	-2444 (-2517, -2371)
a2		954 (944.7, 963.2)	134 (-73.48, 341.5)
b2		627.3 (574.9, 679.7)	-1207 (-1223, -1192)
a3		-323.6 (-350.5, -296.7)	-196.8 (-332.9, -60.72)
b3		-166.7 (-199, -134.4)	-282.8 (-344, -221.5)
a4		-82.93 (-116.3, -49.55)	-211.3 (-343.4, -79.32)
b4		369.8 (355.7, 383.8)	-304.8 (-370.7, -238.8)
a5		125.9 (101.5, 150.2)	-118.3 (-194.8, -41.71)
b5		-117.1 (-131.6, -102.6)	-105.4 (-159.4, -51.41)
a6		-140 (-150.9, -129.2)	-128.6 (-179.9, -77.28)
b6		-43.9 (-60.28, -27.51)	-66.09 (-122.6, -9.622)
a7		28.54 (23.62, 33.45)	-51.15 (-72.66, -29.64)
b7		50.55 (40.16, 60.94)	-16.93 (-47.6, 13.75)
a8		8.203 (5.509, 10.9)	-45.66 (-49.76, -41.55)
b8		-45.04 (-48.88, -41.2)	10.7 (-12.88, 34.27)
Goodness of fit			
SSE		1.6e+09	1.868e+09
R-square		0.9969	0.9951
Adjusted R-square		0.9969	0.9951
RMSE		**126.6505**	**150.6**

Table 17: Coeficcient with 95% confidence bounds comparison.

Both the power curves are compared in table 18, from cut in wind speed 4m/s, to rated wind speed, 13m/s. By examining the table, we can clearly tell that the corrected power curve yields lower power output for the same wind speeds between cut-in and rated.

Wind speed [m/s]	Power curve raw [kW]	Cp	Power curve corrected [kW]	Cp
4	267	0.37	258	0.35
5	670	0.47	578	0.4
6	1303	0.53	1150	0.46
7	2137	0.55	1866	0.47
8	3111	0.53	2779	0.47
9	4220	0.51	3758	0.45
10	5185	0.46	4793	0.42
11	5832	0.38	5627	0.37
12	5962	0.30	5956	0.3
13	5979	0.24	5977	0.24

Table 18: Comparison of power curves

6.4 WindPRO

In this sub chapter the work and results for WindPRO will be presented. The chapter is further split into three sub chapters as follows:

Chapter 6.4.1 ‘’Project setup and Annual Energy Production (‘’AEP’’)’’: Both power curves determined in chapter 6.3 will be utilized for comparison in AEP calculation using reanalysis data scaled to local LiDAR data using transfer functions. The main purpose for this chapter is to determine the suitability for reanalysis data scaling when we have small ampunts of local data available. For this thesis’ instance, our local data only covers 12% of the reference period. Data used in this analysis is presented in chapter 5.2.1 (LiDAR) along with reanalysis data.

Chapter 6.4.2 ‘’Wake models’’: As a part of the AEP calculation, the Jensen wake model and the Eddy-viscosity (Ainsle) wake model is used for energy reduction. This chapter compares the two models and displays turbine-by-turbine reduction in energy due to wakes.

Chapter 6.4.3 ‘’ Performance check’’: the performance check is a stand-alone module in WindPRO where the individual turbines SCADA data is used together with power curve.

As WindPRO is a very practical software and the knowledge of the software is mainly for industry, chapter 6.4 will be presented as ‘’step by step’’ approach. It should be noted that WindPRO requires the use of MATLAB or other numeric computing software in some of the iterative processes. Illustrations given in this chapters are made both through MATLAB and WindPRO. For a better overview the source will be given in the figure citation.

6.4.1 Project Setup and Annual Energy Production

The first step in the setup was to import the geo-reference map of Westermost Rough with the correct coordinate and datum (WGS84) information. When starting a new WindPRO project WTG’s can either be imported as a shapefile or placed one by one at the desired location. Another option is to import the existing wind turbines from the EMD server, which is a comprehensive source for WTG positions worldwide. The server is based on data downloaded 2019-12-04. Westermost Rough has not experienced any modification with regards to turbine position since that period and can be assumed accurate. The Siemens Gamesa SWT-6.0-154 wind turbine is not part of the EMD wind turbine catalogue, so the first step is to create a new wind turbine that has the same properties as the SWT-6.0-154. The basic information is retrieved from the producer’s technical data sheet as presented in table 7 and 8, (chapter 5.1) as

both the power curves are to be tested we create two new power curves. The two power curves with their respevtive power coefficient can be seen in figure 29 and 30.

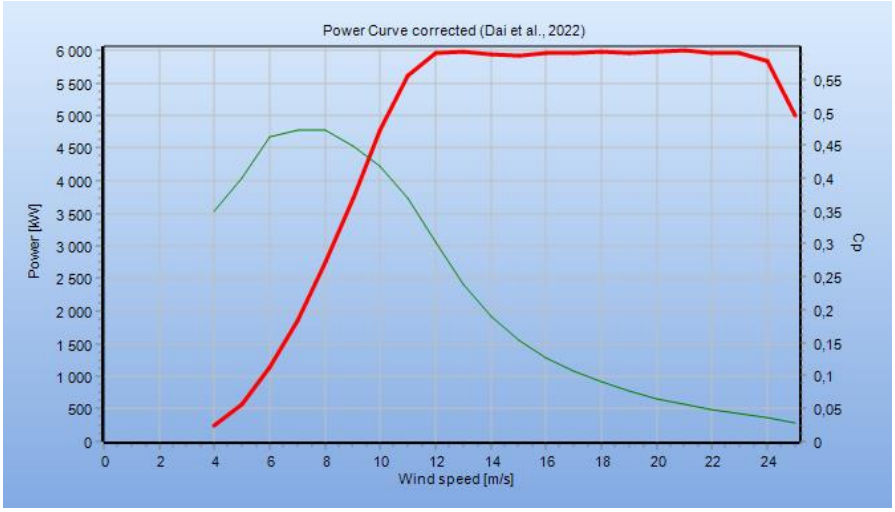

Figure 29: Corrected power curve (red), Power coefficient (green); WindPRO.

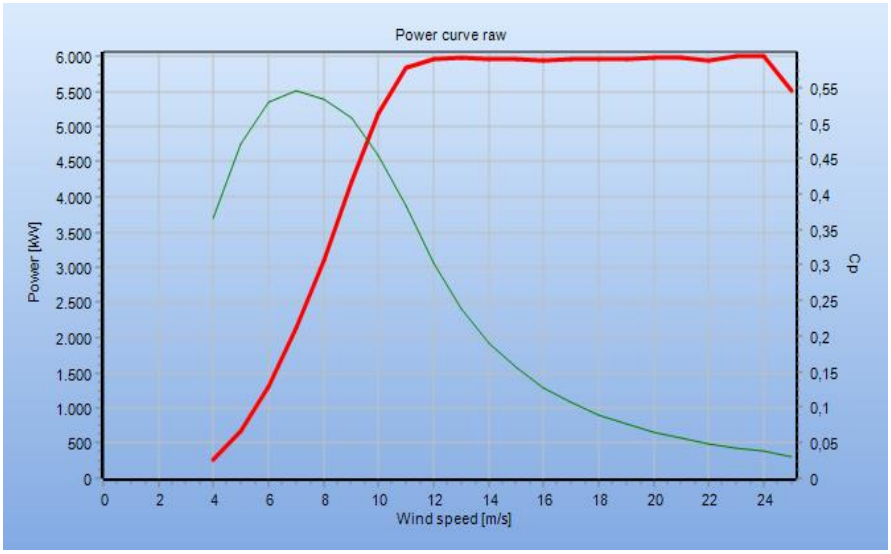

Figure 30: Raw power curve (red), Power coeficcient (green); WindPRO.

Now that the turbines have been positioned by the EMD database and validated with the use of the turbine metadata retrieved by Ørsted. the WMR wind park turbine layout can be seen in figure 31.

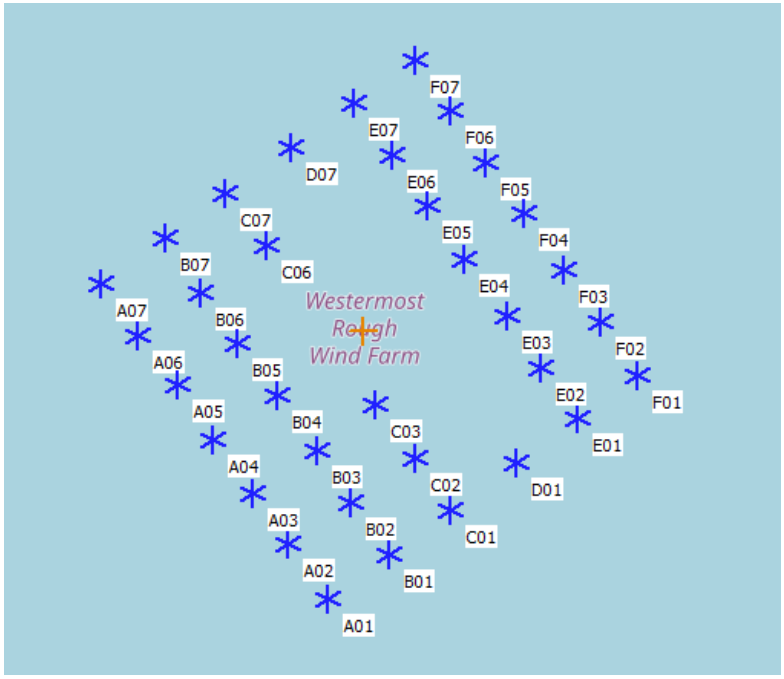

Figure 31: Westermost Rough park layout. Turbines (blue) and cite center (orange); WindPRO.

Next, we place METEO Objects within the wind farm. One object containing the local measurement data retrieved from LiDAR. Since the LiDAR is placed on the roof of the substation Z01 and we know the substation coordinates, we can name the METEO object Z01 and place it within the correct coordinates. The LiDAR data is imported as ASCII time series. In the import setup, we choose the type of data, sub-type (mean, std, max, min), and unit. We also choose the specific heights the data is representing. In the data setup we choose the lower and higher limits of the data. Here we can add or delete signals to the different heights. Because of small amount of LiDAR measurements within the reference period, calculating the annual energy produced (AEP) done solely with the use of LiDAR measurements can not be done and is why we want to examine the possibility of using reanalysis data scaled to local measurements, in order to make a coherent time series for the whole reference period. We create a new METEO object for the reanalysis data and proceed to download the data sets of interest directly from the EMD. When downloading the reanalysis data in to the METEO object, we select the relevant third party reanalysis data sets NEWA, NORA3, the Global assimilation dataset ERA5 and check for coverage in the area around the WMR wind farm. The location of the datasets relative to the wind farm is depicted in figure 32.

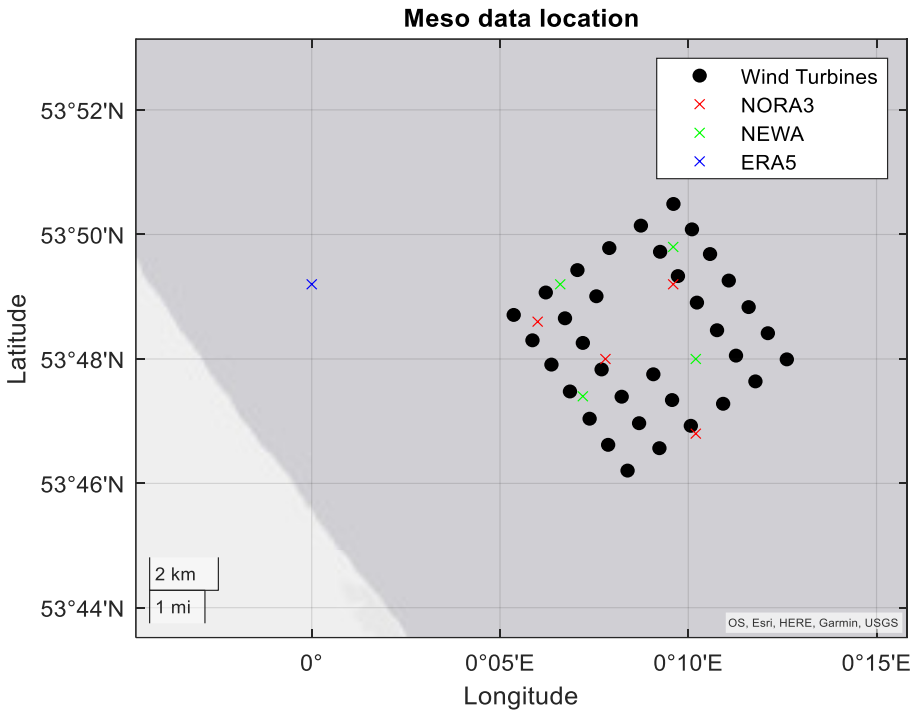

Figure 32: WMR wind park with location of reanalysis data given with colour codes; MATLAB

Now the measured data (LiDAR) from METEO object is the basis, and interpolations together with WasP calculated transfer functions (scaler) gives the calculated wind speed, wake reductions, and output power at each turbine for each time step. The method for scaling is an iterative process that starts by choosing the LiDAR data that we want to calibrate the reanalysis data to. For this we have chosen to use 74 – 214 meters, as 74m is the lowest measurement available on site, and the wind turbine blade tip does not exceed 214m. The LiDAR data that is used in METEO Analyzer[1] is: wind speed, wind direction and wind speed standard deviation for all height, along with sea surface temperature. The lowest measurement also includes temperature and relative humidity. We choose which METEO object we want to scale from, in which we start with the NORA3 data, and run the EMD default scaler. Now, a new scaled data series is created through transfer functions. By examining the newly created time series to the local measurement at hub height during a concurrent period we see clear trends and similarity. A good tool for comparison is the radar graph presented in figure 35 which displays the wind

[1] METEO Analyzer: the METEO analyzer is a tool that works directly on the data located in the Meteo objects. The analyzer has the ability to work on data from multiple objects in parallel and is therefore suitable for creating new time series based on a scaler and immediately compare it with other measurements (e.g. downscaled meso data to a local measurement) which is essential for post calibration of the scaler so that scaled data matches the measured data better. The meteo analyzer is also suitable for substituting/filling data from one signal to another.

speed and direction on concurrent time stamps for the LiDAR data and the raw NORA3 data before doing any scaling.

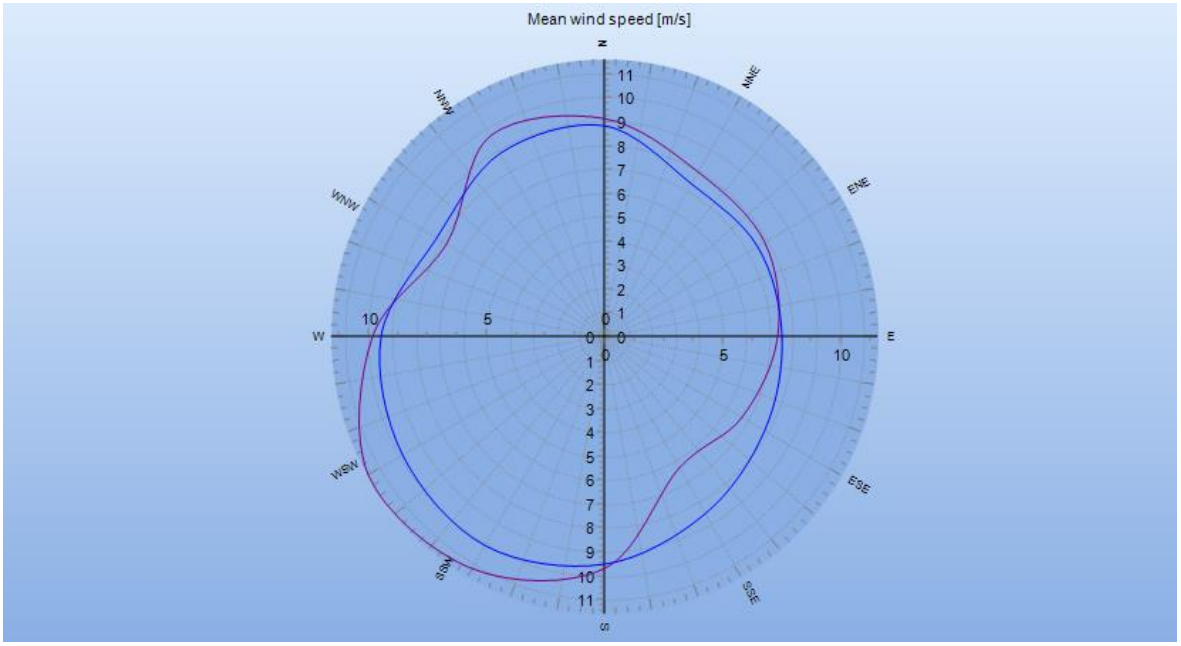

Figure 33: Comparison during reference period 16.01.2016 – 06.12.2017. Wind speed and direction at hub height. LiDAR data (purple), raw NORA3 (blue); WindPRO

The two radar graphs in figure 33 shows a decent correlation, but are not completely aligned. To bring the correlation to a higher, we create a scaler based on the ratios from Figure 33. One important measure of the scaler is to bring the meso data as close to the measured wind distribution (weibull fit) as possible. Figure 34 shows the Weibull distribution of both the raw NORA3 and the LiDAR measurements. By examining the two Weibull distributions we can tell there is a deviation and we therefore proceed to scaling.

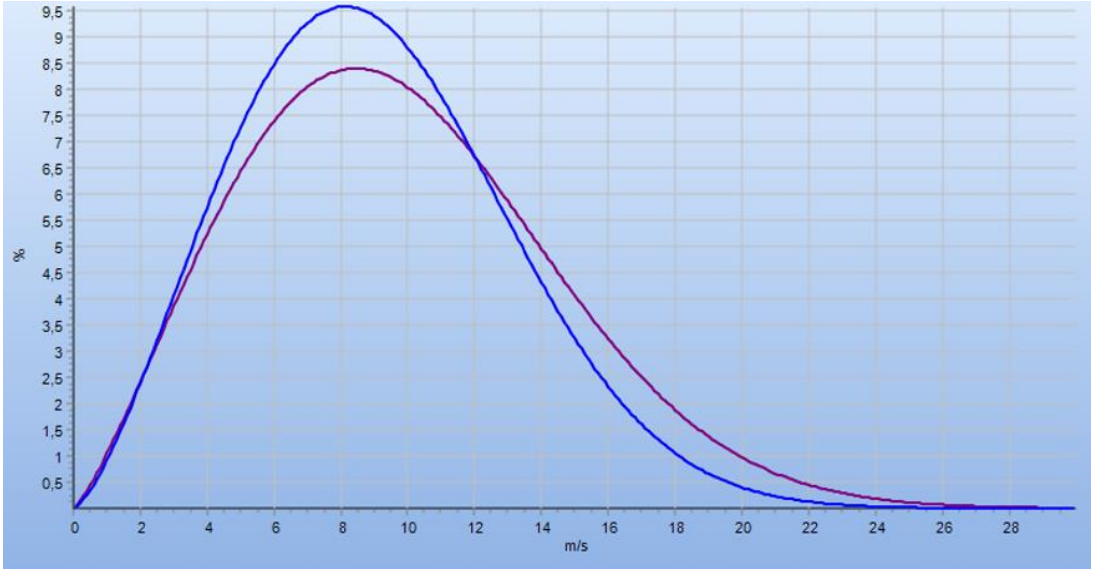

Figure 34: Weibull distribution raw NORA3 (blue) and LiDAR measurements (purple) both at hub height; WindPRO.

The post calibration of the scaler is carried out in accordance with EMD manual: we start by extracting the data from the radar graph, which contains the mean wind speed at different directions presented in table 19.

Mean Wind Speeds at direction			
Angle	**Local measurement**	**NORA3**	**Ratio**
360	9.106399977	8.611711237	1.0334000
330	7.947962941	7.386914597	1.075951649
300	7.853478217	7.502077113	1.046840508
270	7.37772279	7.574436464	0.974029266
240	6.761111121	7.874660921	0.858590762
210	6.357105276	8.549430151	0.743570643
180	9.749479744	9.517286816	1.024396967
150	11.2316556	10.1213912	1.109694841
120	11.59393587	9.882118498	1.173223725
90	9.836360775	9.509897979	1.034328738
60	7.71897261	8.240999645	0.936654889
30	9.677093054	8.833116543	1.095546856

Table 19: Directional ratios of local measuremnt (LiDAR) to raw NORA3.

We can tell from the table that the NORA3 data under-predicts at in north direction (0 degrees) and overpredicts in direction east to south. Now that the ratios have been determined we can return to the scaler and correct section-wise it according to table 19. After the sectional configuration the scaler is shaped as shown in figure 35, where the black circle indicates the base case (all ratios =1), and blue shape shows section wise correction.

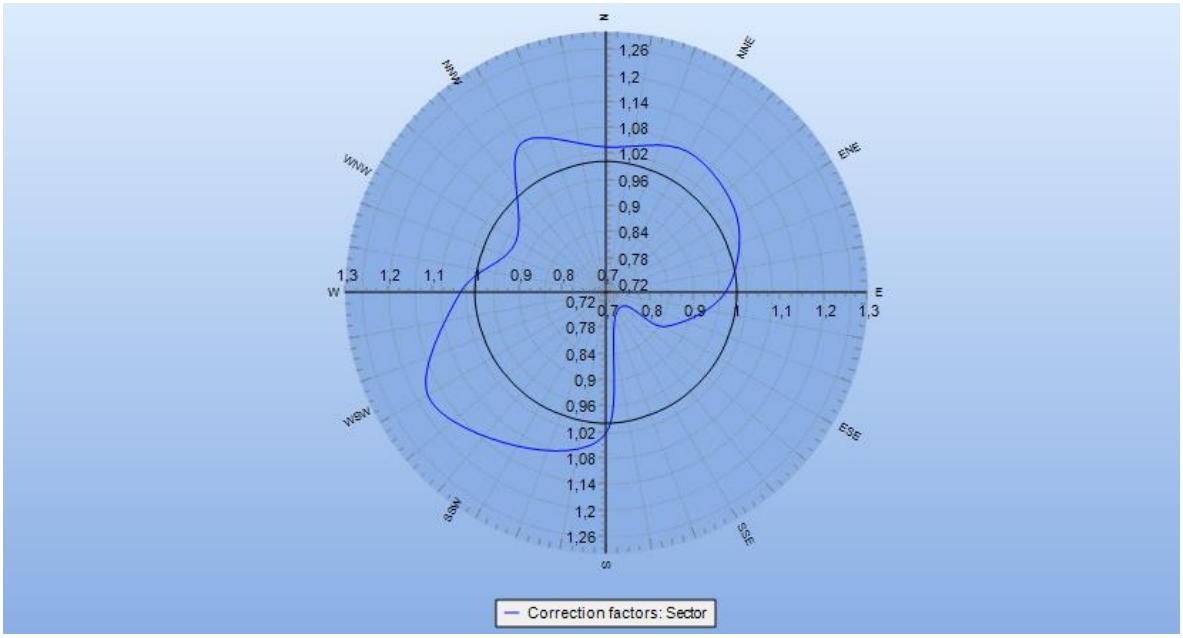

Figure 35: Scaler with added correction factors section wise, blue shape illustrates the sectional configurations of the scaler; WindPRO

Now that we have calculated the ratios for the different directions, the MCP module is used to analyze the correlation between the local measurements and the scaled long-term reference data. Comparing the data statistics of the local measurements and the sectional corrected NORA3 data as illustrated in table 20.

Count	measured wind speed (LiDAR)		NORA3 sectional corr.	
	mean [m/s]	Std.dev [m/s]	mean [m/s]	Std.dev [m/s]
1856	9.61	4.8	10.75	5.2

Table 20: MCP module Comparison LiDAR data to the sectional corrected NORA3

Based on the assumption that the cumulative distributions of the modelled data shall be the same as the measured, the information in table 20 can be utilized and the following relationship is used:

$$\frac{u_{model} - u_{mean,model}}{StDev,model} = \frac{u_{meas} - u_{mean,meas}}{StDev,meas} \quad [45]$$

From this relationship the following formulas for the needed calibration can be derived:

$$\text{Main}Scale = \frac{\sigma_{measured}}{\sigma_{model}} \quad [46]$$

Where $\sigma_{measured}$ is the wind speed standard deviation for measured (LiDAR) data, and σ_{model} is the standard deviation og the model data available in table 20.

$$MainOffset = u_{mean,meas} - \left(\frac{\sigma_{measured}}{\sigma_{model}}\right) \times u_{mean,model} \quad [47]$$

Once we have determined the main scale and offset value, we return to the METEO analyzer to correct the scaler. We now create the final time series which is the scaled NORA3 data. By examining the Weibull distribution for the two datasets in figure 36, we can clearly see a good correlation. The new radar graph comparison (figure 37) also shows a good match.

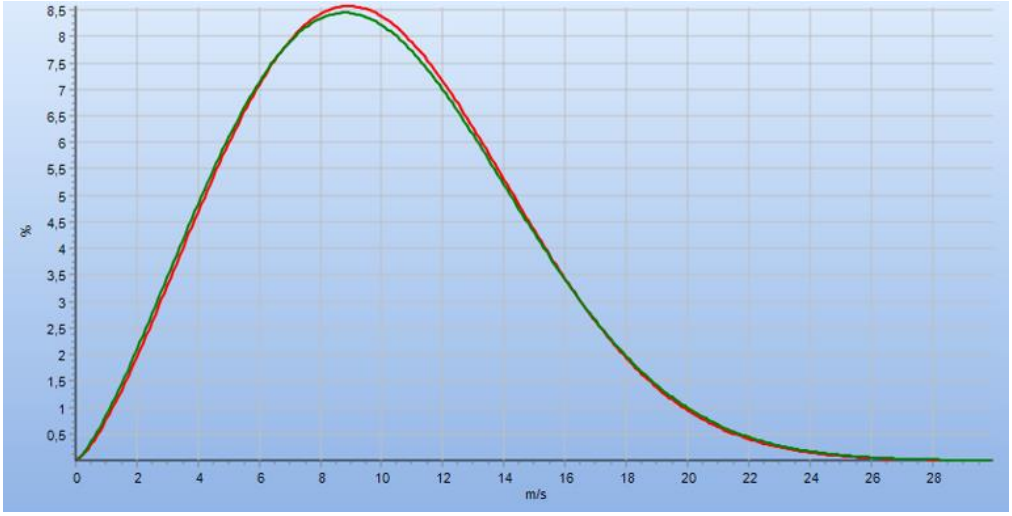

Figure 36: Weibull distribution of scaled NORA3 (red) at hub height, and LiDAR data (green) at hub height; WindPRO.

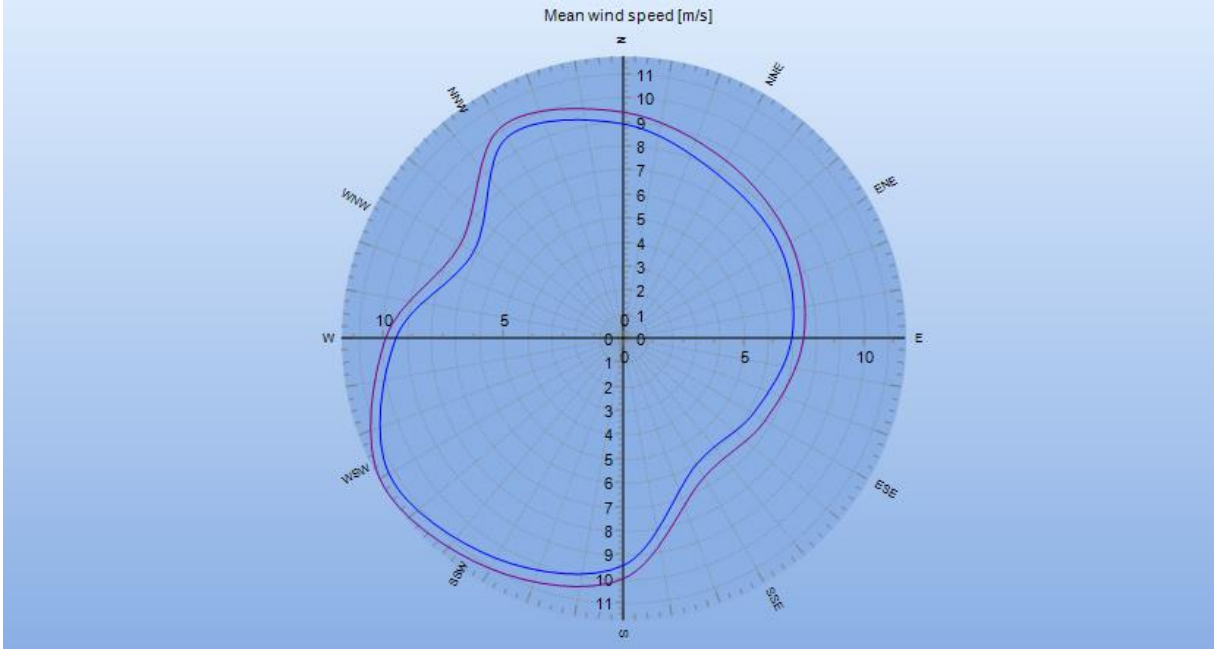

Figure 37: Radar graph of scaled NORA3 (blue) at hub height, and LiDAR data (purple) at hub height; WindPRO.

Once we have completed the new time series with the scaler, we calculate the AEP in the PARK calculation module. The procedure followed in this chapter has been applied to NORA3, ERA5, and NEWA data sets in order to compare and find the best fit for WMR. The results are compared to the actual SCADA data and presented in tables. There have been tested two different power curves (corrected and raw) and two different wake models (Jensen and eddy-viscosity wake model). The results will be presented in separated tables and in a comparing graph. The full production analysis for the different data sets can be found in Appendix 1(a) to (d). Table 21 presents the daily averaged correlation between the reanalysis data and LiDAR data before and after scaling.

	NORA3	ERA5	NEWA
Scaled meso Correlation to LiDAR – Energy (daily averaged)	0.980	0.983	0.943
Scaled meso Correlation to LiDAR - Wind speed (daily averaged)	0.983	0.985	0.956
Raw meso data correlation to LiDAR Energy (Daily averaged)	0.977	0.979	0.927
Raw meso data correlation to LiDAR Wind speed (Daily averaged)	0.982	0.983	0.945

Table 21 : The correlation is between concurrent samples: 1856, approximately 2,5 months during the reference period.

It should be mentioned that the correlations would have been more sensitive to change if averaged to a narrower time ineterval.

The following tables 22 – 25, and figure 39 shows the AEP using the scaled reanalysis data for different scenarios given by the table captions. The different scenarios can be seen in figure 38.

	NORA3	ERA5	NEWA	SCADA
Production [MWh/y]	**806 823.0**	**883 180.20**	**899 259.40**	**867 369**
Turbine average [MWh/y]	23 052.09	25 233.72	25 693.13	24 794.8
Wake Loss [%] average year	6.61	6.00	5.97	-
Capacity factor [%]	39.4	43.2	44	-
Full load hours [hours/year]	3 458	3 785	3 854	-

Table 22: Production table using power curve corrected and Jensen wake model with scaled reanalysis data.

	NORA3	ERA5	NEWA	SCADA
Production [MWh/y]	**780 630.0**	**865 422.20**	**879 996.40**	**867 369**
Turbine average [MWh/y]	22 303.71	24 726.35	25 142.74	24 794.8
Wake Loss [%] average year	9.88	7.90	7.98	-
Capacity factor [%]	38.2	42.3	43	-
Full load hours [hours/year]	3 346	3 709	3 771	-

Table 23: Production table using power curve corrected and eddy-viscosity wake model with scaled reanalysis data.

	NORA3	ERA5	NEWA	SCADA
Production [MWh/y]	**863 636.90**	**936 211.20**	**952 592.10**	**867 369**
Turbine average [MWh/y]	24 675.34	26 748.89	27 216.92	24 794.8
Wake Loss [%] average year	6.61	5.82	5.78	-
Capacity factor [%]	42.2	45.8	46.6	-
Full load hours [hours/year]	3 701	4 012	4 083	-

Table 24: Production table using raw power curve and Jensen wake model with scaled reanalysis data.

	NORA3	ERA5	NEWA	SCADA
Production [MWh/y]	**844 850.0**	**919 091.0**	**934 150.10**	**867 369**
Turbine average [MWh/y]	24 138.57	26 259.74	26 690.01	24 794.8
Wake Loss [%] average year	8.65	7.53	7.61	-
Capacity factor [%]	41.3	44.9	45.7	-
Full load hours [hours/year]	3 621	3 939	4 003	-

Table 25: Production table using raw power curve and eddy-viscosity model with scaled reanalysis data.

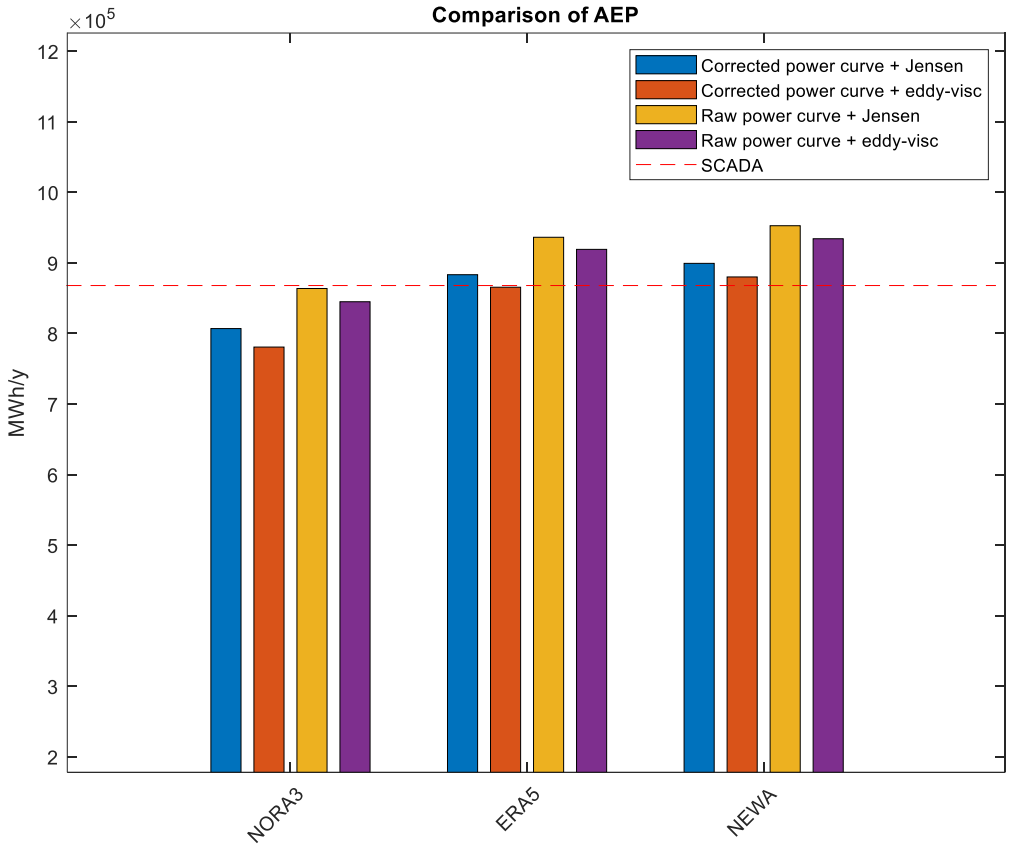

Figure 38: Comparison of AEP thourgh different sources using scaled reanalysis data; MATLAB.

For comparison the same methodology is followed for the raw meso-data to see the impact of the 12 % of LiDAR data used in scaling. Table 26-29 shows the raw reanalysis data with different configurations.

	NORA3	ERA5	NEWA	SCADA
Production [MWh/y]	**974 230**	**887 343**	**969 378**	**867 369**
Turbine average [MWh/y]	25 052	22 817	24 956	24 794.8
Wake Loss [%] average year	5.5	6.4	5.6	-
Capacity factor [%]	47.6	43.4	47.4	-
Full load hours [hours/year]	4 175	3 803	4 154	-

Table 26: Production table using raw reanalysis data, corrected power curve, and Jensen wake model.

	NORA3	ERA5	NEWA	SCADA
Production [MWh/y]	**953 616**	**870 038**	**949 238**	**867 369**
Turbine average [MWh/y]	24 522	24 956	24 409	24 794.8
Wake Loss [%] average year	7.5	6.2	7.6	-
Capacity factor [%]	46.6	43.1	46.4	-
Full load hours [hours/year]	4 087	3 833	4 068	-

Table 27: Production table using raw reanalysis data, corrected power curve, and Eddy-viscosity wake model

	NORA3	ERA5	NEWA	SCADA
Production [MWh/y]	**1 028 180**	**942 971**	**1 021 782**	**867 369**
Turbine average [MWh/y]	26 439	24 248	26 274	24 794.8
Wake Loss [%] average year	5.3	6.2	5.4	-
Capacity factor [%]	50.3	46.1	50	-
Full load hours [hours/year]	4 406	4 041	4 379	-

Table 28: Production table using raw reanalysis data, raw power curve, and Jensen wake model.

	NORA3	ERA5	NEWA	SCADA
Production [MWh/y]	**1 008 606**	**924 810**	**1 002 713**	**867 369**
Turbine average [MWh/y]	25 936	23 781	25 784	24 794.8
Wake Loss [%] average year	7.1	8.0	7.2	-
Capacity factor [%]	49.3	45.2	49	-
Full load hours [hours/year]	4 323	3 963	4 297	-

Table 29: Production table using raw reanalysis data, raw power curve, and Eddy-viscosity wake model.

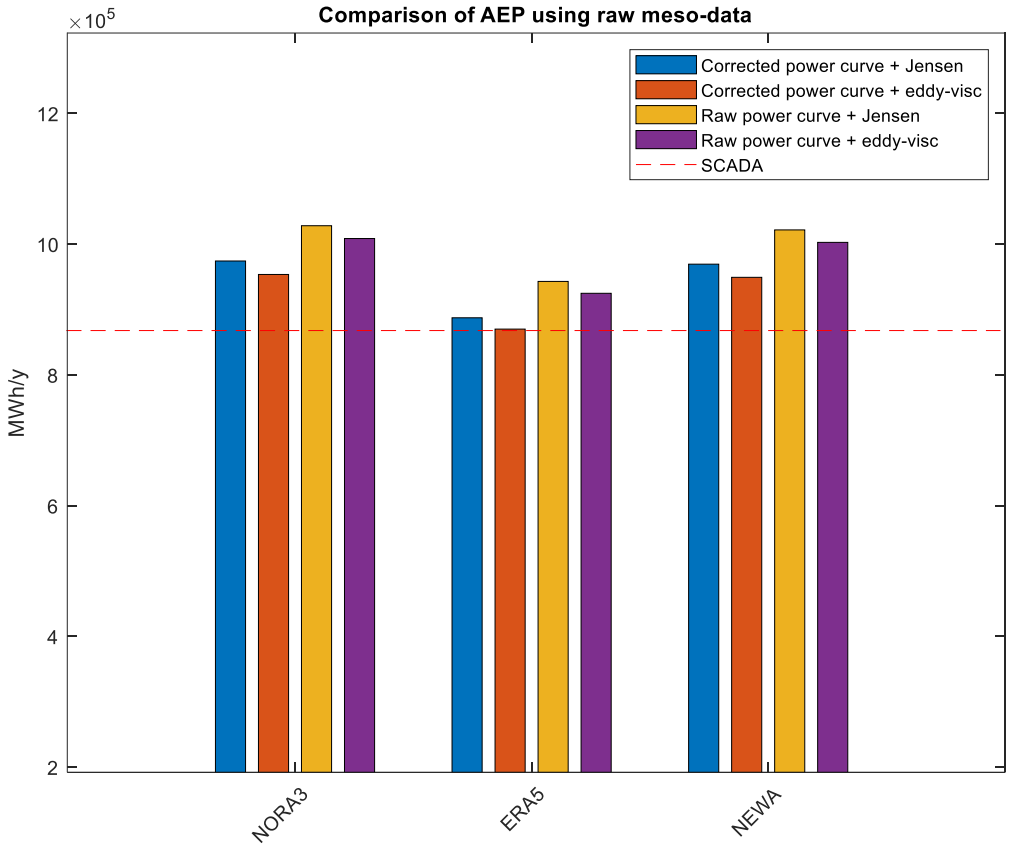

Figure 39: Comparison of AEP thourgh different sources using raw reanalysis data; MATLAB.

When comparing figure 38 to 39, ERA5 best fit for WMR when comparing the AEP to actual SCADA data. Figure 40 shows the time series for the raw ERA5, the scaled ERA5, and the raw lidar data in a period where we have concurrent data. Figure 42 shows the scaled ERA5 together with the raw ERA5 over one month. Both figure 41 and 42 is given for comparison.

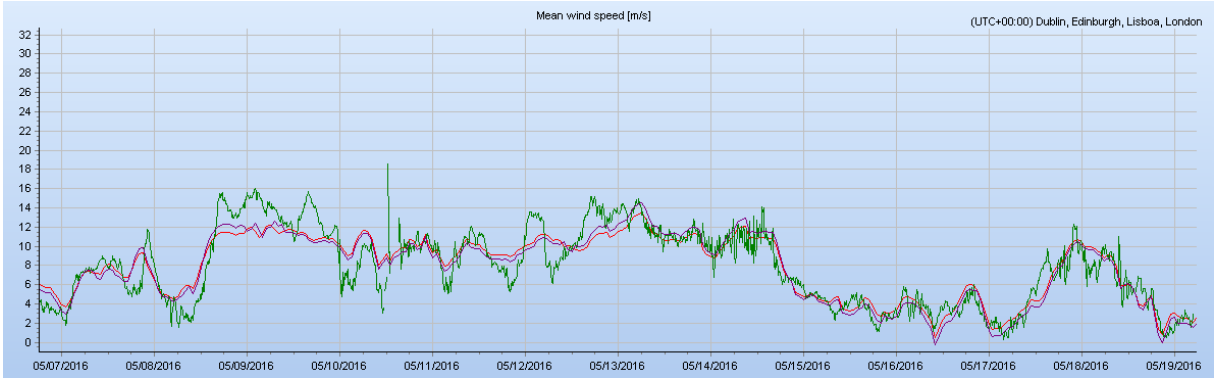

Figure 40: Raw ERA5 (red), LiDAR measurement (green), scaled ERA5 (purple); WindPRO.

We can tell from figure 40 that the scaled ERA5 follows the LiDAR trends, but struggles to capture the short-term fluctuations. The displayed period is from 07.05.2016 - 19.05.2016.

Figure 41: Scaled ERA5 (green), Raw ERA5 (red); WindPRO.

By examining figure 41, we can see that the scaled ERA5 adds both higher peeks and lower throughs compared to the raw ERA 5. The displayed period is from 09.01.2016 – 08.02.2016.

The sector-wise energy production [MWh/y] and wake losses for the whole park, using the ERA5 corrected data together with corrected power curve and Eddy viscosity wake model, is shown in figure 42. The complete analysis for this scenario can be found in Appendix 2.

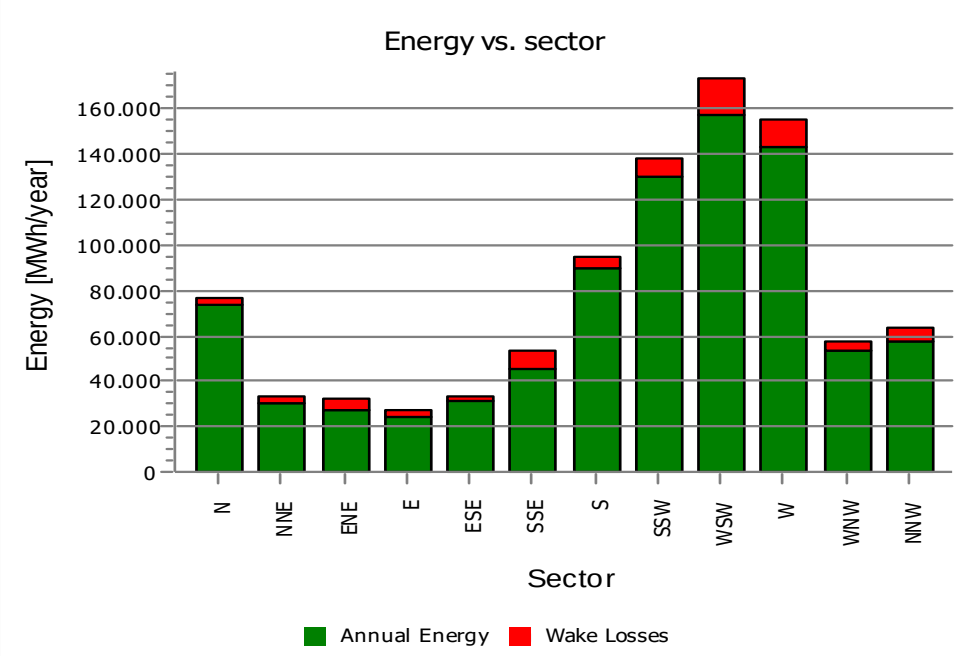

Figure 42: Energy [MWh/year] based on section including wake losses; WindPRO

6.4.2 *Wake models*

In the following, wake reduction is presented in percentage by the different models. Results for the corrected power curve only is presented as it seems to give a more realistic description of the power generated by the WTG-s. Wake reduction as a percentage of the AEP is preented in figure 43, with different scaled reanalysis data, (a) to (f). For section wise wake reduction of scenario (b), see Appendix 2, table 32.

When using the Eddy viscosity model, the parameter we need to choose is the surface roughness. For normal offshore conditions, EMD recommends to use 0,0002. This is also what is used in this thesis. The choice of wake decay constant is crucial when using the Jensen wake model. A coefficient of 0.06 is applied in this thesis, which according to DTU's findings in 2018 yields more accuracy for offshore conditions.

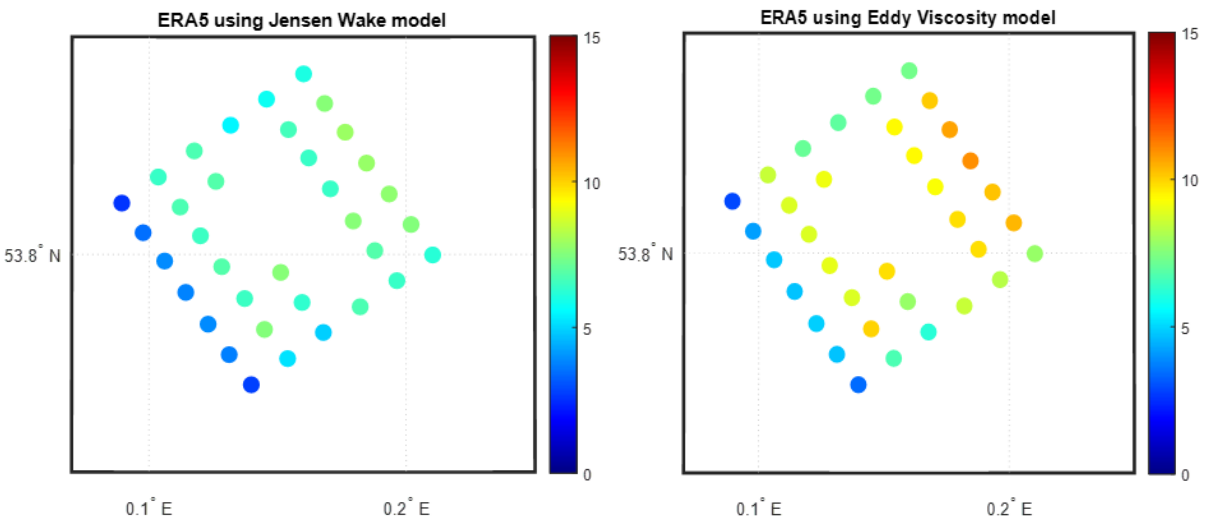

(a) (b)

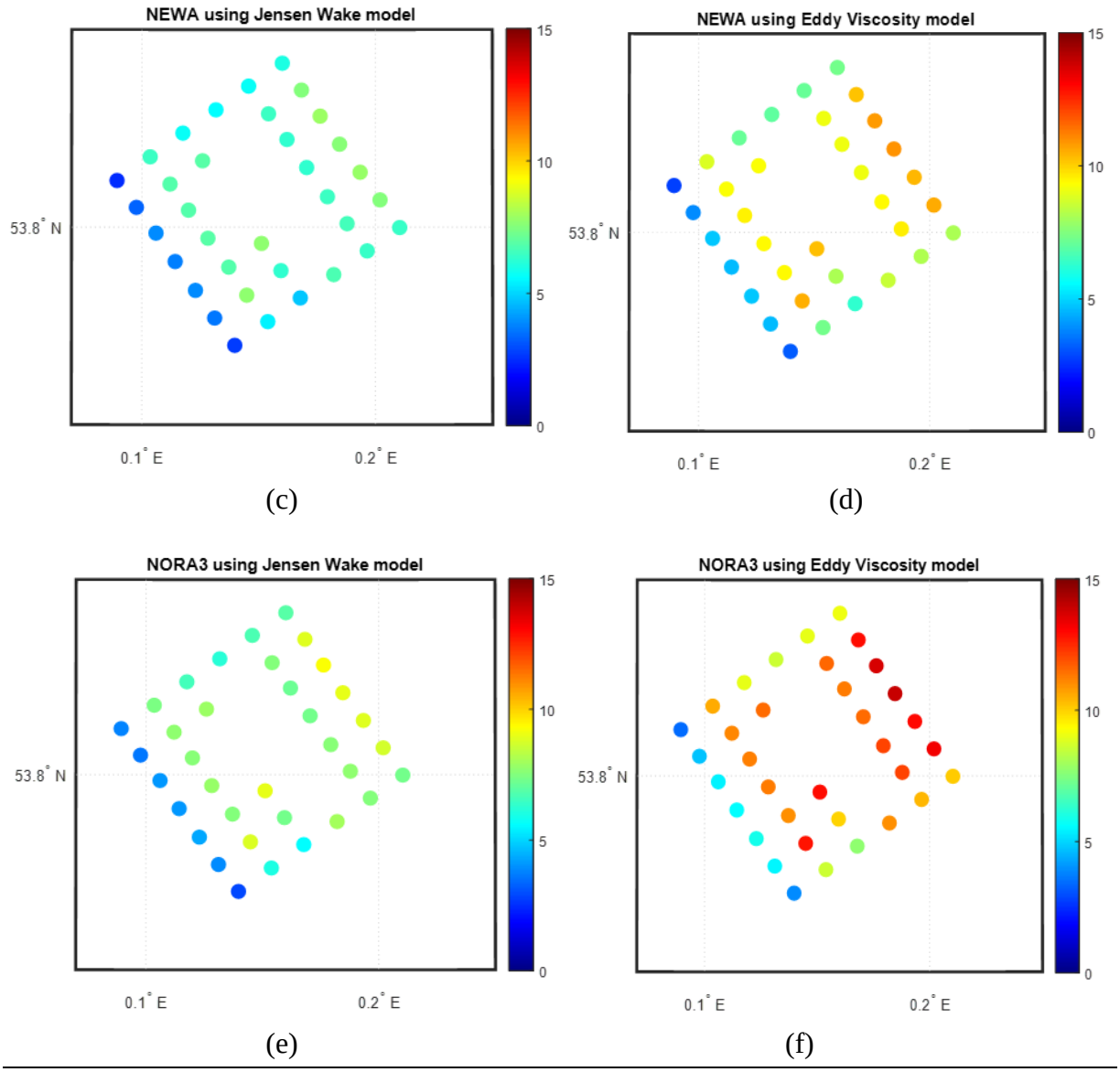

Figure 43: Percentage wake loss MATLAB were (a) ERA5 using Jensen Wake model; (b) ERA5 using Eddy viscosity model; (c) NEWA using Jensen Wake model; (d) NEWA using Eddy Viscosity model; (e) NORA3 using Jensen Wake model; (f) NORA3 using Eddy Viscosity model.

6.4.3 Performance Check -post construction

This sub-chapter is not an continuation of the previous result chapters but serves as a stand-alone chapter. None of the power curves described in chapter 7 are utilized in the performance check as one of the module tasks is to assign filter codes that indicates stopped or suboptimal performance and applied to all the 35 turbines specific power curves, based solely on SCADA data. The SCADA data is paired and loaded in to their respective turbine.

Actual production is used to calculate the potential production when the WTG is normal operation with no faults or stoppage. For periods when there are faults or stops, production is determined using the wind speed experienced at the nacelle, and the historic power curve. The potential production is long-term corrected by using an energy index to correctly establish the normalized production. Following this, expected long-term future losses are subtracted to get to the expected future production. The NET production calculation is based on the parameters in table 30.

NET production calculation basis	
Turbine type	Siemens Gamesa SWT-6.0-154 154
Number of turbines	35
Production data set	SCADA
Production data period	Jan/2016 – dec/2017
Reference data set	NORA3
Reference data period	Jan/1999 – dec/2022

Table 30: Net production calculation basis.

The power curve (historical) is the turbine specific power curve based on the analysis operation period's filtered SCADA data. The discrepancy between potential and actual production is characterized as lost production. Actual losses are those incurred during the operation period under consideration. Potential production is characterized as the production that could have become realized if the turbine had been running at full capacity, and it is determined by using the nacelle wind speed together with the historical power curve. According to EMD, normalized production can be defined as the production a wind farm would generate in a regular year with no losses (except for electrical losses and wake losses). Expected losses are the anticipated future losses, which may include electrical losses and losses due to degradation if specified.

For the individual turbine power curves, self-consumption has been omitted. The measured binned power curve is the result of normal operational data and is used to calculate losses for time stamps that have been filtered as a ‘’stop’’ or ‘’suboptimal’’ operating period. The power curve for WTG A01 is displayed in figure 44 where the red dots are the measured data, pink dots are the filtered data, and green dots are the binned measured data. Because of the black circumference of the dots, measurements displays as black whenever there is a high measurement density.

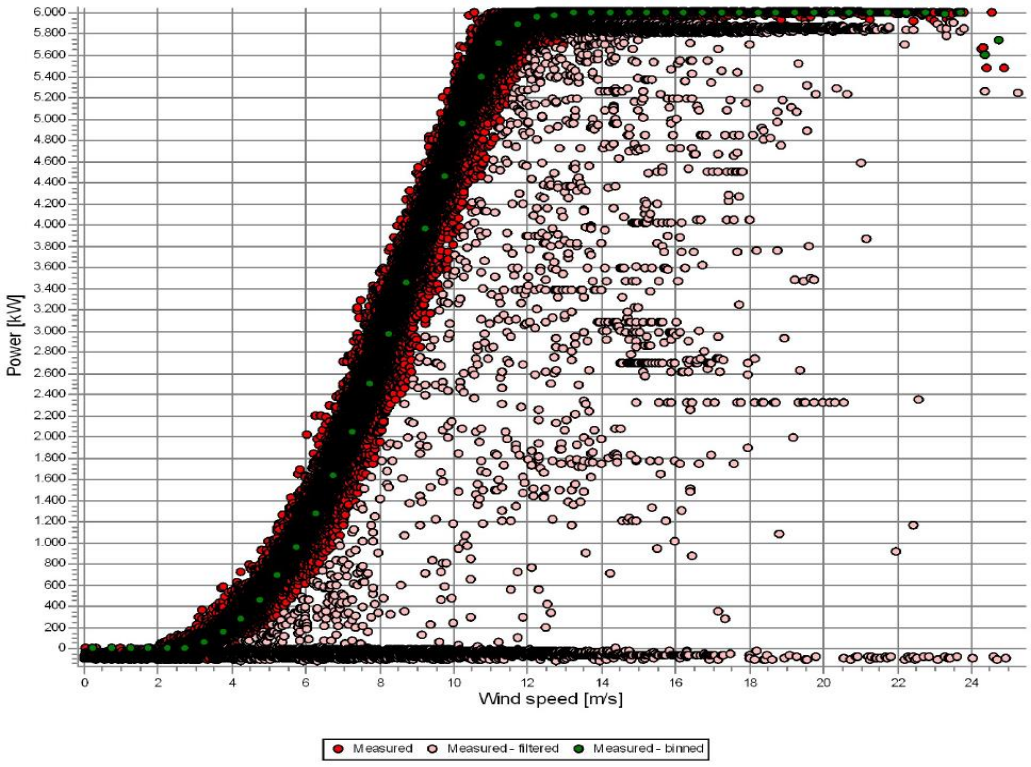

Figure 44: Power curve A01; WindPRO

Because the nacelle wind speed is influenced by the operational mode of the WTG the IEC 61400-26-1 recommends correcting for the potential bias. The correction filter is applied to the nacelle wind speeds during periods, where the turbine has nor operated in an ideal way to correct for the bias. Because error codes were not given by the SCADA data, it was manually inserted to WindPRO. The error codes chosen are: (1) stop when wind speed is more than 4m/s and power less or equal to 5 % of rated power. (2) for steep part- stop when wind speed is more than 4m/s and power below wind speed shifted PC is 1 m/s. (3) for flat part – stop when power is below rated power. (4) stop when above cut out wind speed.

Actual losses are calculated for each time step that coincides with an error occurrence as the difference between measured power and potential power based on the power curve (historic)

and the corrected wind speed experienced at the nacelle. The production analysis is presented in table 31.

WTG	[1] [MWh]	[2] [%]	[3] [MWh] / [MWh/y]	[4] LT corr.fac*	[5] [MWh/y]	[6] [%]	[7] [MWh/y]
All	**1766681**	**3,86**	**1837624 / 918812**	**0,997**	**916500**	**5,36**	**867369**
C03	51140	2,17	52274 / 26137	0,997	26069	3,67	25112
B04	45926	7,98	49907 / 24953	0,997	24886	9,48	22527
E04	51701	3,54	53600 / 26800	0,997	26733	5,04	25384
B05	49906	2,43	51148 / 25574	0,997	25499	3,93	24498
C06	50236	3,33	51965 / 25983	0,997	25910	4,83	24659
B03	50328	3,64	52231 / 26115	0,997	26049	5,14	24710
C02	48060	6,64	51480 / 25740	0,997	25672	8,14	23581
E05	51793	2,06	52881 / 26441	0,997	26370	3,56	25432
E03	48916	5,24	51623 / 25812	0,998	25752	6,74	24015
B06	49189	4,63	51578 / 25789	0,998	25728	6,13	24150
B02	48254	5,48	51050 / 25525	0,997	25454	6,98	23678
E06	48637	2,81	50042 / 25021	0,998	24971	4,31	23896
E02	50701	3,99	52806 / 26403	0,998	26340	5,49	24895
A04	50374	4,35	52668 / 26334	0,997	26263	5,85	24726
A05	50266	6,25	53618 / 26809	0,998	26748	7,75	24675
C07	49812	3,66	51704 / 25852	0,998	25797	5,16	24466
D07	51310	3,20	53007 / 26504	0,997	26431	4,70	25189
F04	49888	3,40	51646 / 25823	0,997	25753	4,90	24491
A03	50800	5,72	53880 / 26940	0,997	26871	7,22	24932
C01	49269	3,99	51316 / 25658	0,997	25587	5,49	24183
D01	51695	2,81	53188 / 26594	0,997	26523	4,31	25381
F05	49592	4,29	51816 / 25908	0,997	25829	5,79	24333
F03	48109	2,75	49471 / 24736	0,998	24690	4,25	23639
B07	50905	3,06	52514 / 26257	0,997	26183	4,56	24988
A06	53611	2,10	54761 / 27380	0,997	27311	3,60	26328
E07	51874	4,08	54083 / 27041	0,997	26973	5,58	25466
B01	51066	3,13	52718 / 26359	0,997	26290	4,63	25072
A02	49897	5,22	52645 / 26322	0,998	26282	6,72	24516
E01	51721	4,36	54077 / 27038	0,998	26974	5,86	25394
F06	52135	2,31	53365 / 26683	0,997	26614	3,81	25601
F02	51246	3,14	52905 / 26452	0,997	26384	4,64	25160
A07	53628	2,05	54748 / 27374	0,998	27308	3,55	26339
A01	52158	4,97	54885 / 27443	0,998	27375	6,47	25604
F07	51926	3,83	53995 / 26998	0,997	26927	5,33	25491
F01	50614	2,72	52029 / 26015	0,998	25953	4,22	24857

Table 31 : [1]Actual Production [2]Actual losses [3]Potential production [4]LT corr.factor* [5]Normalized production AEP [6]Expected total losses [7] Net production AEP

*The long-time correction factor is based on the ratio between normalized production AEP and potential energy production.

The monthly losses for the whole wind farm during the reference period are displayed in figure 45.

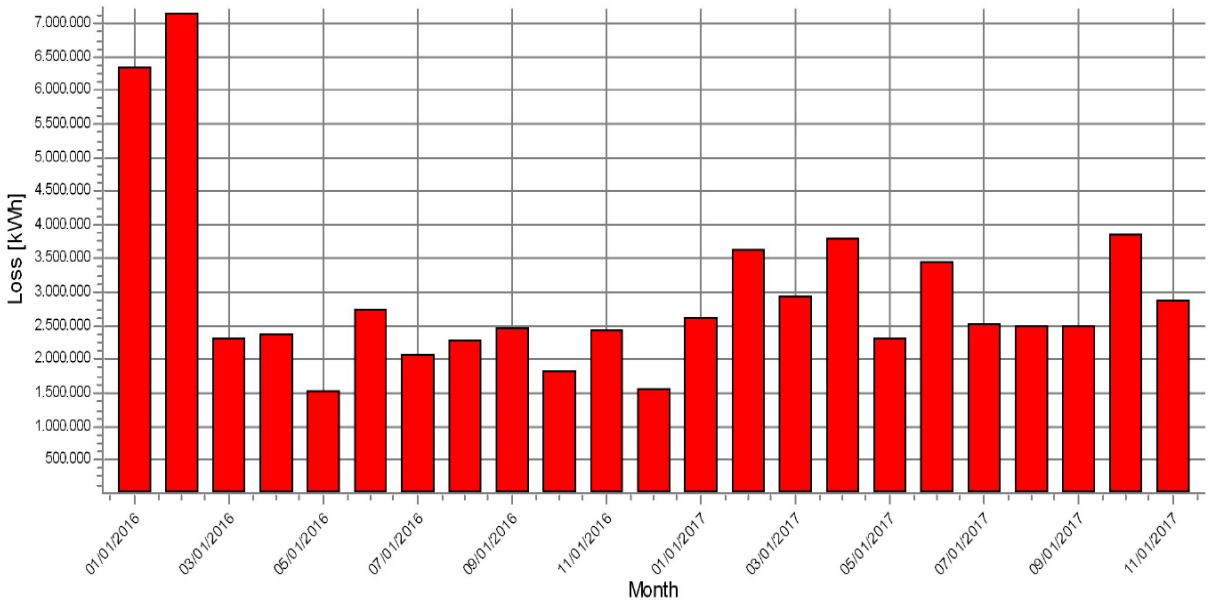

Figure 45: Monthly losses for all turbines; WindPRO.

7 Summary and Discussion

This chapter is separated in-to the six main objectives of the thesis for a better overview. Let us recall the thesis main objectives.

(1) Compare different methods for determining the atmospheric stability.

In determination of the atmospheric stability at Westermost Rough wind farm both the bulk Richardson number and Gradient Richardson number were used for comparison. For the bulk method under steady conditions where the stability parameter is negative, the bin averages can to some degree be described by the MO theory (logarithmic law) for measures at low elevation. The same is true for neutral conditions when the stability parameter is zero. For unsteady conditions where the stability parameter is positive the methods show strong inadequacy. The deviation from theory increases with elevation and shows inadequacy for all stability conditions at high altitudes. The same applies when using the gradient Richardson number, although this method showed worse results for all heights and the RMSE value difference between the two methods showed an increase along with elevation. The findings from this study support Gryning et al (2007) study on the validity of Monin Obukhov scaling at higher altitudes, and the need for extended wind profiles to describe shear at high altitude.

(2) Use LiDAR data to calculate Energy output through hub height wind speed and rotor equivalent wind speed.

The Hub height wind speed was was compared to the rotor equivalent wind speed in order to best predict the energy output. Data from LiDAR containing measurements from 13.01.2016 to 17.02.2016 were used for this analysis as it was the longest period with coherent measurements. Both methods was then compared to the SCADA data power output for the same period. Within the short period of measurement available, allthough both HHWS and REWS underestimated the power output, the power output were best predicted using REWS. This supports Ryu et al (2022) conclusion on REWS ability to predict higher wind speeds. Both in this thesis and the study carried out by Ruy et al at Anholt wind park, REWS had a more accurate prediction than the HHWS.

(3) Obtain the real power curve through SCADA data.

The objective for chapter 6.3 was to obtain the real power curve through the use of SCADA data, inspired by a novel idea by Dai et al (2022). The idea is based on the assumption that the

wind speed experienced by the anemometer installed at the nacelle, downwind of the WTG rotor, is not of the same magnitude as the wind speed experienced at the WTG rotor. To compensate for the difference between the measured and actual wind speed the wind speed was corrected by applying moving average filtering (MAF). In order to see the impact of different window lengths, the illustrations in chapter 6.3 is based on one week of measurements (1008 10-min measurements). The wind speed was tested corrected with window lengths of 10 to 30. The chapter applied N=10 as window length of choice, as this window length succeeds to describe the consistency of trends without smoothing the graph too much. It should be emphasized that the length is an approximate value. The corrected wind speed is presented in a graph along with the raw wind speed. As a result of MAF the corrected wind speed had a reduction in wind speed fluctuations with a small delay in time compared to the raw wind speed.

The corrected power curve was compared against the raw power curve where the corrected power curve showed a more conservative power output than the raw power curve for the same wind speeds from cut-in to start of rated. This matches the assumption put out by Dai et al (2022) that the wind speed recorded at the anemometer is distorted, and that the WTG requires higher wind speeds to match the recorded power output.

(4) Scale reanalysis data to LiDAR on-cite measurements for long-time correction and compare the energy prediction to actual energy production.

In chapter 6.4, the main objective was to determine the suitability of the different reanalysis data sets (NORA3, NEWA, and ERA5) when scaled to very scarce amount of local LiDAR measurements. The data sets are tested along with the Jensen wake model, and the Eddy viscosity wake model. Both the corrected power curve and the raw power curve were also tested.

All the reanalysis data sets showed too large power production before scaling (raw), for all scenarios (figure 39). When applying offset value and sectional correction to the scaler, the power output decreased for all data sets, making them come closer to the actual SCADA data. The ERA 5 data set seems to experience the least configurations out of the data sets. The main assumption for this is that the ERA5 data set had the highest correlation before applying scaler, and maintaing highest correlation after (table 21). Anyhow, this does not explain the strong improvement of the NORA3 data after applying the scaler. It should be mentioned again that the correlation is based on daily averages and only includes concurrent data. If WindPRO had the ability to show correlation with smaller time steps it would be more convenient to see the

connection. In other words, when looking at a larger averaged for correlation, the difference of correlation should be smaller than when using smaller averaged, which strengthens the first assumption.

Another assumption that also confirms the findings retrieved by the studies carried out by Solbrekke et al (2021) and Haakenstad et al (2021) (chapther 4.2) that the NORA3 windspeeds typically is 5% lower than the actual wind speeds can be drawn by studying the difference in total load hours for the NORA3 data before and after the scaling of the data set. After applying the scaler, NORA3 experiences a significant reduction in total load hours which indicates that the raw NORA3 wind speeds has too many measurements within range of the power curve (too low wind speeds), and when applying the scaler, a fair amount of the measurements ends up outside the range of the power curve.

When evaluating this specific site, the ERA5 dataset yielded an over-all better result than the other data sets when comparing energy output to the actual SCADA data.

(5) Compare performance of the Jensen wake model and the Eddy viscosity wake model.

The Jensen wake model and the Eddy viscosity wake model were tested for the different scenarios in chapter 6.4. When examining the wake distributions in chapter 6.4.2, figure 43. We can see that the middle turbines positioned at upwind row F experience the most wake reductions, while the most down-wind turbines, row A experiences the least. This may seem counter intuitive but can be explained by the fact that the distance between adjacent turbines in a row is shorter than the distance to the closest turbine from a different column. The distances between the turbines can be found in Appendix 3, table 34. Also, good park arraying can contribute to this phenomenon. The main yaw-direction is given in arrows can be seen in Appendix 3, Figure 50.

Based on the illustrations in chapter 6.4.2, figure 43, the turbine C03 seems to experience significant wake losses even tho it only has one adjacent turbine in the row. A reasenable explanation for this is that the offshore sub-station Z01 (LiDAR) is placed adjacent to this turbine (Appendix 3, figure 49).

In this thesis, the Eddy viscosity model proved to be the most conservative wake model. This does not coincide with Sørensen et al (2006) comparison on model performance as their findings showed that the Jensen wake model yielded the most conservative results. It should be mentioned that Sørensen's study used a wake decay constant of 0.04. In this thesis a wake decay constant of 0.06 is used, resulting in quicker recovery of the wind field behind the turbine. Appendix 5, figure 52 contains an extract from Sørensen et al (2006) comparing park efficiency using the Jensen wake model together with a wake decay constant of 0.04, and one using 0.075. The two different wake decay constant clearly shows an impact on park efficiency.

(6) Performance check for the wind farm using SCADA data in WindPRO

The final objective of this thesis was to perform a post construction performance check of the Westermost rough wind farm in WindPRO. The results are presented in chapter 6.4.3, table 31 which describes the actual power production, actual losses, potential production, normalized production AEP, expected total losses, and net production AEP. The monthly losses in kWh for the whole park can be visualized though figure 45, chapter 6.4.3. The results shows significant larges losses for January and February 2016 than the rest of the reference period. As the same months in 2017 does not experience the same trends it can not be linked to a seasonal bias. Anyhow, longer measuring period would be necessary to describe trends in energy losses. It should be mentioned that we would have received a more precise result if we had the actual error codes from turbine log files.

8 References

Ahsbahs, Tobias, et al. "Wind farm wakes from SAR and doppler radar." *Remote Sensing* 12.3 (2020): 462.

Akgül, Fatma Gül, Birdal Şenoğlu, and Talha Arslan. "An alternative distribution to Weibull for modeling the wind speed data: Inverse Weibull distribution." *Energy Conversion and Management* 114 (2016):234-240.

Antoniou, Ioannis, Søren Markilde Pedersen, and Peder Bay Enevoldsen. "Wind shear and uncertainties in power curve measurement and wind resources." *Wind Engineering* 33.5 (2009): 449-468.

Aries, Nawel, Sidi Mohammed Boudia, and Houdayfa Ounis. "Deep assessment of wind speed distribution models: A case study of four sites in Algeria." *Energy Conversion and Management* 155 (2018): 78-90.

Azad, A. K., M. M. Alam, and Manabendra Saha. "Effect of wind shear coefficient on wind velocity at coastal sites of Bangladesh." *International conferencen on Mechanical Engineering, Dhaka, Bangladesh* (2011): 1-6.

Bojek, Piotr. "Renewable Electricity." (2022).

Bratton, Daniel C., and Carole A. Womeldorf. "The wind shear exponent: Comparing measured against simulated values and analyzing the phenomena that affect the wind shear." *Energy Sustainability*. Vol. 54686. 2011.

Carrillo, C., et al. "Review of power curve modelling for wind turbines." *Renewable and Sustainable Energy Reviews* 21 (2013): 572-581.

Celik, Ismail B. "Introductory turbulence modeling." (1999): 33-40.

Chai, Tianfeng, and Roland R. Draxler. "Root mean square error (RMSE) or mean absolute error (MAE)." *Geoscientific model development discussions* 7.1 (2014): 1525-1534.

Charnock, H. "Wind stress on a water surface." *Quarterly Journal of the Royal Meteorological Society* 81.350 (1955): 639-640.

Chen, Zhe, and Frede Blaabjerg. "Wind farm—A power source in future power systems." *Renewable and Sustainable Energy Reviews* 13.6-7 (2009): 1288-1300.

Choukulkar, Aditya, et al. "A new formulation for rotor equivalent wind speed for wind resource assessment and wind power forecasting." *Wind Energy* 19.8 (2016): 1439-1452.

Christie, David, and Simon Neill. "Measuring and observing the ocean renewable energy resource." *Reference Module in Earth Systems and Environmental Sciences; Elsevier: Amsterdam, The Netherlands* (2021).

Csanady, Gabriel T. *Air-sea interaction: laws and mechanisms*. Cambridge University Press, 2001.

Dai J, Zeng H, Zhang F, Chen H and Li M (2022) Study on Obtaining Real Power Curve of Wind Turbines Using SCADA Data. Front. Energy Res. 10:916355. doi: 10.3389/fenrg.2022.916355

Dai, Juchuan, et al. "Research on power coefficient of wind turbines based on SCADA data." Renewable Energy 86 (2016): 206-215

Dorrego Portela, José Rafael, et al. "Microscale Wind Assessment, Comparing Mesoscale Information and Observed Wind Data." *Sustainability* 14.19 (2022): 11991.

Dörenkämper, Martin, et al. "The making of the new european wind atlas–part 2: Production and evaluation." *Geoscientific model development* 13.10 (2020): 5079-5102.

EEA, 2022. European Environment Agency. [Online] Available at: www.eea.europa.eu/signals/signals-2022/articles/state-of-play-energy-underpins [Accessed 03 05 2023].

EMD, 2014. Modules. [Online] Available at: http://www.emd.dk/WindPRO/Modules/ [Accessed 01 06 2023].

EMD, 2023. EMD WindPRO. [Online] Available at: http://www.emd-international.com/windpro/ [Accessed 04.05.2023].

EMD, 2023b. Mesoscale Data. [Online] Available at: www.emd-international.com/windpro/online-data/ [Accessed 06.05.2023].

EMD, 2023c. PARK. [Online] Available at: www.emd-international.com/windpro/windpro-modules/energy-modules/park/ [Accessed 07.05.2023].

Emeis, Stefan. "Current issues in wind energy meteorology." *Meteorological Applications* 21.4 (2014): 803-819.

European Commission, 2023. European Green Deal. [Online] Available at: ec.europa.eu/commission/presscorner/detail/en/IP_23_2061. [Accessed 01 05 2023].

Geernaert, G. L. "Surface layer." *Encyclopedia of atmospheric sciences* (2003): 305-311.

Grachev, A. A., and C. W. Fairall. "Dependence of the Monin–Obukhov stability parameter on the bulk Richardson number over the ocean." *Journal of Applied Meteorology* 36.4 (1997): 406-414.

Gryning, Sven-Erik, et al. "On the extension of the wind profile over homogeneous terrain beyond the surface boundary layer." *Boundary-layer meteorology* 124 (2007): 251-268.

Haakenstad, Hilde, et al. "NORA3: A nonhydrostatic high-resolution hindcast of the North Sea, the Norwegian Sea, and the Barents Sea." *Journal of Applied Meteorology and Climatology* 60.10 (2021): 1443-1464.

Han, Qinkai, et al. "Non-parametric models for joint probabilistic distributions of wind speed and direction data." *Renewable Energy* 126 (2018): 1032-1042.

Hansen, Martin OL. *Aerodynamics of wind turbines*. Routledge, 2015.

Hansen, Kurt S., et al. "The impact of turbulence intensity and atmospheric stability on power deficits due to wind turbine wakes at Horns Rev wind farm." *Wind Energy* 15.1 (2012): 183-196.

Hasager, Charlotte Bay, et al. "Using satellite SAR to characterize the wind flow around offshore wind farms." *Energies* 8.6 (2015): 5413-5439.

Hersbach, Hans, et al. "Operational global reanalysis: progress, future directions and synergies with NWP." (2018).

Hersbach, Hans, et al. "ERA5 hourly data on single levels from 1979 to present." *Copernicus climate change service (c3s) climate data store (cds)* 10.10.24381 (2018).

Hersbach, Hans, et al. "The ERA5 global reanalysis." *Quarterly Journal of the Royal Meteorological Society* 146.730 (2020): 1999-2049.

Holtslag, M. C., W. A. A. M. Bierbooms, and G. J. W. Van Bussel. "Estimating atmospheric stability from observations and correcting wind shear models accordingly." *Journal of Physics: Conference Series*. Vol. 555. No. 1. IOP Publishing, 2014.

IEC, IEC. "61400-12-1 Wind turbines–Part 12-1: Power performance measurements of electricity producing wind turbines." *Geneva, Switzerland: IEC* (2005).

International Electrotechnical Commission, 1998, “Wind Turbine Generator Systems—Part 12: Wind Turbine Power Performance Testing,” Technical Report No. IEC 61400-12.

Jogararu, M. J. 2018. MCP (MEASURE – CORRELATE – PREDICT). [Online] Available at: https://help.emd.dk/knowledgebase/content/Guides/QuickGuide_MCP.pdf [Accessed 04 04 2023]

Katic, I., Jørgen Højstrup, and Niels Otto Jensen. "A simple model for cluster efficiency." *European wind energy association conference and exhibition*. Vol. 1. Rome, Italy: A. Raguzzi, 1986.

Landberg, Lars, et al. "Wind resource estimation—an overview." *Wind Energy: An International Journal for Progress and Applications in Wind Power Conversion Technology* 6.3 (2003): 261-271.

Magnusson, M., K. G. Rados, and S. G. Voutsinas. "A study of the flow downstream of a wind turbine using measurements and simulations." *Wind Engineering* (1996): 389-403.

Meyers, Johan, et al. "Wind farm flow control: prospects and challenges." *Wind Energy Science* 7.6 (2022): 2271-2306.

Nielsen, P., 2016. *PARK WITH SCALER AND MEASURED WIND DATA*. [Online] Available at:https://help.emd.dk/knowledgebase/content/Guides/Quick_Guide_PARK_Measurement_SCALER_Calculation_2016.pdf [Accessed 05.04.2023]

Nygaard, Nicolai Gayle, and Alexander Christian Newcombe. "Wake behind an offshore wind farm observed with dual-Doppler radars." *Journal of Physics: Conference Series*. Vol. 1037. No. 7. IOP Publishing, 2018.

Nygaard, Nicolai Gayle, et al. "Modelling cluster wakes and wind farm blockage." *Journal of Physics: Conference Series*. Vol. 1618. No. 6. IOP Publishing, 2020.

Obhrai, Charlotte, Siri Kalvig, and Ove Tobias Gudmestad. "A review of current guidelines and research on wind modelling for the design of offshore wind turbines." *ISOPE International Ocean and Polar Engineering Conference*. ISOPE, 2012.

Perrin, Olivier, Holger Rootzén, and Roger Taesler. "A discussion of statistical methods used to estimate extreme wind speeds." *Theoretical and applied climatology* 85 (2006): 203-215.

Peña, Alfredo, Pierre-Elouan Réthoré, and M. Paul van der Laan. "On the application of the Jensen wake model using a turbulence-dependent wake decay coefficient: the Sexbierum case." *Wind Energy* 19.4 (2016): 763-776.

Platis, Andreas, et al. "First in situ evidence of wakes in the far field behind offshore wind farms." *Scientific reports* 8.1 (2018): 2163.

Putri, Rieska Mawarni, Charlotte Obhrai, and J. M. Knight. "Offshore wind turbine loads and motions in unstable atmospheric conditions." *Journal of Physics: Conference Series*. Vol. 1356. No. 1. IOP Publishing, 2019.

Qin, Zhilong, Wenyuan Li, and Xiaofu Xiong. "Estimating wind speed probability distribution using kernel density method." *Electric Power Systems Research* 81.12 (2011): 2139-2146.

Rathmann, Ole Steen, et al. "The park2 wake model-documentation and validation." *Peninsula Risø: DTU Wind Energy* (2018).

Ray, M. L., A. L. Rogers, and J. G. McGowan. "Analysis of wind shear models and trends in different terrains." *University of Massachusetts, Department of Mechanical and Industrial Engineering, Renewable Energy Research Laboratory* (2006).

Robeson, Scott M., and Karsten A. Shein. "Spatial coherence and decay of wind speed and power in the north-central United States." *Physical Geography* 18.6 (1997): 479-495.

Rose, Stephen, and Jay Apt. "What can reanalysis data tell us about wind power?." *Renewable Energy* 83 (2015): 963-969.

Ryu, Geon Hwa, et al. "Analysis of Vertical Wind Shear Effects on Offshore Wind Energy Prediction Accuracy Applying Rotor Equivalent Wind Speed and the Relationship with Atmospheric Stability." *Applied Sciences* 12.14 (2022): 6949.

Saleh, H., A. Abou El-Azm Aly, and S. Abdel-Hady. "Assessment of different methods used to estimate Weibull distribution parameters for wind speed in Zafarana wind farm, Suez Gulf, Egypt." *Energy* 44.1 (2012): 710-719.

Sarkar, Arnab, et al. "Weibull and generalized extreme value distributions for wind speed data analysis of some locations in India." *KSCE Journal of Civil Engineering* 23 (2019): 3476-3492.

Shakoor, Rabia, et al. "Wake effect modeling: A review of wind farm layout optimization using Jensen′ s model." *Renewable and Sustainable Energy Reviews* 58 (2016): 1048-1059.

Scott, Ryan, et al. "Evolution of eddy viscosity in the wake of a wind turbine." *Wind Energy Science* 8.3 (2023): 449-463.

Shi, Huanyu, et al. "Wind speed distributions used in wind energy assessment: a review." *Frontiers in Energy Research* (2021): 790.

Sebastiani, Alessandro, et al. "Data analysis and simulation of the Lillgrund wind farm." *Wind Energy* 24.6 (2021): 634-648.

Solbrekke, Ida Marie, Asgeir Sorteberg, and Hilde Haakenstad. "The 3 km Norwegian reanalysis (NORA3)–a validation of offshore wind resources in the North Sea and the Norwegian Sea." *Wind Energy Science* 6.6 (2021): 1501-1519.

Sorensen, P., and T. Nielsen. "Recalibrating wind turbine wake model parameters—validating the wake model performance for large offshore wind farms." *European Wind Energy Conference and Exhibition, EWEA*. 2006.

Stiesdal , Henrik. *Reducing Cost of Energy in the Offshore Wind Energy Sector*. *University Press of Southern Denmark*, 2019. pp. 11-16.

Stull, Roland B. "Mean boundary layer characteristics." An Introduction to Boundary Layer Meteorology. Springer, Dordrecht, 1988. 1-27.

Sumner, Jonathon, and Christian Masson. "Influence of atmospheric stability on wind turbine power performance curves." (2006): 531-538.

Troen, I. E. L. P., and Erik Lundtang Petersen. "European wind atlas." (1989).

Türk, Matthias, and Stefan Emeis. "The dependence of offshore turbulence intensity on wind speed." *Journal of Wind Engineering and Industrial Aerodynamics* 98.8-9 (2010): 466-471.

Van Sark, Wilfried GJHM, et al. "Do we really need rotor equivalent wind speed?." *Wind Energy* 22.6 (2019): 745-763.

VanLuvanee, David Ryan. "Investigation of observed and modeled wake effects at Horns Rev using WindPRO." *Technical University of Denmark Department of Mechanical Engineering* (2006).

VanLuvanee, D., et al. "Effects of atmospheric conditions on wind turbine power performance and review of proposed correction techniques." *Proceedings of WindPower 2009* (2009).

Veers, Paul, et al. "Grand Challenges in the Design, Manufacture, and Operation of Future Wind Turbine Systems." *Wind Energy Science Discussions* (2022): 1-102.

Vickers, Dean, and L. Mahrt. "Fetch limited drag coefficients." *Boundary-Layer Meteorology* 85 (1997): 53-79.

Wagner, Rozenn, et al. "Accounting for the speed shear in wind turbine power performance measurement." *Wind Energy* 14.8 (2011): 993-1004.

Wagner, Rozenn, et al. "The influence of the wind speed profile on wind turbine performance measurements." *Wind Energy: An International Journal for Progress and Applications in Wind Power Conversion Technology* 12.4 (2009): 348-362.

Wang, Guichao, et al. "Estimation of the dissipation rate of turbulent kinetic energy: A review." *Chemical Engineering Science* 229 (2021): 116133

Wang, Lingzhi, Jun Liu, and Fucai Qian. "Wind speed frequency distribution modeling and wind energy resource assessment based on polynomial regression model." *International Journal of Electrical Power & Energy Systems* 130 (2021): 106964.

Weibull, Waloddi. "A statistical distribution function of wide applicability." *Journal of applied mechanics* (1951).

Weisman, Morris L., and Joseph B. Klemp. "The structure and classification of numerically simulated convective stormsin directionally varying wind shears." *Monthly weather review* 112.12 (1984): 2479-2498.

Wharton, Sonia, and Julie K. Lundquist. "Assessing atmospheric stability and its impacts on rotor-disk wind characteristics at an onshore wind farm." *Wind Energy* 15.4 (2012): 525-546.

Wharton, Sonia, and Julie K. Lundquist. "Atmospheric stability affects wind turbine power collection." *Environmental Research Letters* 7.1 (2012): 014005.

Woo, Jae-kyoon, et al. "AEP Prediction of a Wind Farm in Complex Terrain: WindPRO Vs. WindSim." *한국태양에너지학회 논문집* 32.6 (2012): 1-10.

Xu, Xiaoyuan, Zheng Yan, and Shaolun Xu. "Estimating wind speed probability distribution by diffusion-based kernel density method." *Electric Power Systems Research* 121 (2015): 28-37.

Yang, K., and K. Cho. "Simulated annealing algorithm for wind farm layout optimization: A benchmark study. Energies 2019, 12, 4403."

Ørsted, 2015. ORSTED. [Online] Available at: https://orsted.com/en/media/newsroom/news/2015/05/full-power-at-westermost-rough-offshore-wind-farm [Accessed 06.04.2023]

Standards:

• IEC 61400-1. Wind Turbines – Part 1: Design Requirements, 2005

• GL Guidelines for the Certification of Offshore Wind Turbines, Ed. 2005

• IEC 61400-3: Wind Turbines – Part 3: Design Requirements for Offshore Wind Turbines, 2009

• DNV-RP-C205: Environmental Conditions & Environmental Loads, October 2010

• DNV-OS-J101: Design of Offshore Wind Turbine Structures, September 2011

• DNV-RP-J101: Use of Remote Sensing for Wind Energy Assessments, April 2011

Appendices

Appendix 1 – Turbine Production

(a) Turbine production using corrected power curve and Jensen wake model

WTG	NORA3	WL [%]	ERA5	WL [%]	NEWA	WL [%]	SCADA
A01	24 018.00	2.9	26 080.60	2.8	26 595.79	2.7	24 238.00
A02	23 771.00	3.9	25 848.40	3.7	26 343.4	3.6	23 858.00
A03	23 687.40	4.3	25 781.50	3.9	26 265.65	3.9	24 459.00
A04	23 731.60	4.1	25 817.90	3.8	26 303.46	3.7	24 815.00
A05	23 720.80	4.1	25 788.70	3.9	26 247.96	3.9	24 039.00
A06	23 852.10	3.6	25 911.10	3.5	26 424.87	3.3	25 466.00
A07	24 049.10	2.8	26 145.90	2.6	26 652.38	2.5	24 281.00
B01	23 262.50	6	25 440.30	5.2	25 851.39	5.4	25 522.00
B02	22 572.40	8.8	24 821.70	7.5	25 221.54	7.7	26 232.00
B02	22 889.40	7.5	25 088.10	6.5	25 468.64	6.8	23 700.00
B03	22 828.40	7.8	25 019.80	6.8	25 445.89	6.9	26 249.00
B04	22 866.90	7.6	25 084.20	6.5	25 463.81	6.8	25 483.00
B05	22 837.30	7.7	25 045.30	6.7	25 453.31	6.8	25 820.00
B06	22 916.40	7.4	25 116.90	6.4	25 559.09	6.5	24 526.00
B07	23 364.10	5.6	25 525.00	4.9	26 004.24	4.8	24 304.00
C01	22 936.90	7.3	25 159.30	6.3	25 600.42	6.3	25 251.00
C03	22 524.80	9	24 805.30	7.6	25 207.33	7.7	25 512.00
C06	22 798.30	7.9	25 001.80	6.8	25 440.09	6.9	24 473.00
C07	23 121.90	6.6	25 315.90	5.7	25 775.45	5.7	23 565.00
D01	22 757.30	8	25 036.50	6.7	25 491.2	6.7	24 980.00
D07	23 202.10	6.2	25 372.10	5.5	25 794.71	5.6	24 965.00
E01	22 900.80	7.5	25 112.20	6.4	25 585.4	6.4	25 204.00
E02	22 842.30	7.7	25 010.50	6.8	25 510.52	6.6	24 102.00
E03	22 855.40	7.6	25 037.20	7.6	25 557.06	6.5	23 925.00
E04	22 951.30	7.3	25 113.50	6.4	25 614.91	6.3	24 823.00
E05	22 957.60	7.2	25 105.10	6.4	25 610.68	6.3	24 907.00
E06	22 892.00	7.5	25 061.10	6.6	25 557.38	6.5	24 370.00
E07	23 098.90	6.7	25 274.80	5.8	25 769.8	5.7	25 244.00
F01	22 935.40	7.3	25 164.60	6.2	25 594.35	6.3	25 480.00
F02	22 595.50	8.7	24 823.20	7.5	25 271.32	7.5	23 345.00
F03	22 532.90	8.9	24 770.80	7.7	25 201.73	7.8	24 700.00
F04	22 519.00	9	24 754.30	7.8	25 237.04	7.6	24 279.00
F05	22 451.90	9.3	24 708.90	7.9	25 176.68	7.9	25 225.00
F06	22 551.90	8.9	24 799.70	7.6	25 267.7	7.5	25 011.00
F07	23 029.40	6.9	25 238.00	6	25 694.21	6	25 467.00
Total	**806 823.00**	**6.85**	**883 180.20**	**6.00**	**899 259.40**	**5.97**	**867 820.00**

(b) Turbine production using corrected power curve and Eddy-viscosity wake model

WTG	NORA3	WL [%]	ERA5	WL [%]	NEWA	WL [%]	SCADA
A01	23 788.50	3.9	25 933.90	3.4	26 444.90	3.2	25 225.00
A02	23 380.70	5.5	25 584.30	4.7	26 075.00	4.6	24 370.00
A03	23 292.00	5.9	25 527.20	4.9	26 007.60	4.8	24 473.00
A04	23 364.70	5.6	25 590.10	4.7	26 079.80	4.6	24 526.00
A05	23 414.50	5.4	25 563.00	4.8	26 025.10	4.8	24 304.00
A06	23 585.70	4.7	25 709.90	4.2	26 249.10	3.9	24 823.00
A07	23 902.30	3.4	26 081.50	2.9	26 563.80	2.8	24 279.00
B01	22 614.50	8.6	25 038.40	6.7	25 319.50	7.3	25 244.00
B02	21 586.70	12.8	24 150.60	10	24 460.90	10.5	24 281.00
B02	22 019.30	11	24 494.00	8.8	24 765.60	9.4	26 249.00
B03	21 944.50	11.3	24 420.90	9	24 754.60	9.4	25 466.00
B04	21 965.90	11.2	24 497.10	8.8	24 730.50	9.5	23 858.00
B05	22 005.40	11.1	24 478.30	8.8	24 782.70	9.3	24 815.00
B06	22 111.50	10.6	24 558.40	8.5	24 909.40	8.8	23 700.00
B07	22 839.90	7.7	25 172.40	6.2	25 599.80	6.3	23 925.00
C01	22 265.10	10	24 742.70	7.8	25 105.10	8.1	24 980.00
C03	21 561.00	12.9	24 220.30	9.8	24 501.40	10.3	24 238.00
C06	21 911.80	11.5	24 402.30	9.1	24 788.60	9.3	24 039.00
C07	22 529.80	9	24 942.20	7.1	25 370.70	7.1	25 251.00
D01	22 030.20	11	24 566.00	8.5	24 991.00	8.5	24 965.00
D07	22 617.40	8.6	24 970.80	7	25 399.20	7	25 512.00
E01	22 164.80	10.4	24 626.10	8.3	25 071.90	8.2	25 480.00
E02	21 761.20	12.1	24 227.70	9.8	24 711.40	9.6	25 820.00
E03	21 748.00	12.1	24 207.70	9.8	24 753.40	9.4	26 232.00
E04	21 911.20	11.5	24 349.40	9.3	24 849.30	9.1	24 459.00
E05	21 946.60	11.3	24 335.90	9.4	24 847.80	9.1	25 522.00
E06	21 881.00	11.6	24 333.80	9.4	24 824.50	9.1	25 483.00
E07	22 527.10	9	24 898.70	7.3	25 382.20	7.1	24 907.00
F01	22 249.00	10.1	24 746.50	7.8	25 118.60	8.1	25 467.00
F02	21 462.90	13.3	24 058.00	10.4	24 431.60	10.6	24 700.00
F03	21 530.60	13	24 097.80	10.2	24 493.00	10.4	24 102.00
F04	21 316.80	13.9	23 899.40	11	24 336.10	10.9	23 565.00
F05	21 365.30	13.7	23 963.70	10.7	24 376.10	10.8	25 204.00
F06	21 545.60	12.9	24 145.00	10.1	24 543.80	10.2	23 345.00
F07	22 488.50	9.1	24 888.20	7.3	25 332.00	7.3	25 011.00
Total	780 630.00	9.88	865 422.20	7.90	879 996.00	7.98	867 820.00

(c) Turbine production using raw power curve and Jensen wake model

WTG	NORA3	WL [%]	ERA5	WL [%]	NEWA	WL [%]	SCADA
A01	25 665.60	2.9	27 613.30	2.8	28 135.30	2.6	25 225.00
A02	25 410.30	3.8	27 368.00	3.6	27 867.80	3.5	24 370.00
A03	25 324.30	4.2	27 299.90	3.9	27 786.30	3.8	24 473.00
A04	25 368.80	4	27 337.00	3.7	27 825.20	3.7	24 526.00
A05	25 354.20	4	27 302.50	3.9	27 764.50	3.9	24 304.00
A06	25 489.20	3.5	27 426.80	3.4	27 940.90	3.3	24 823.00
A07	25 697.40	2.7	27 671.50	2.6	28 174.20	2.5	24 279.00
B01	24 889.60	5.8	26 960.90	5.1	27 381.80	5.2	25 244.00
B02	24 181.60	8.5	26 331.20	7.3	26 741.60	7.4	24 281.00
B02	24 501.90	7.3	26 597.00	6.4	26 985.40	6.6	26 249.00
B03	24 437.90	7.5	26 522.20	6.6	26 958.20	6.7	25 466.00
B04	24 481.70	7.3	26 590.50	6.4	26 983.10	6.6	23 858.00
B05	24 449.00	7.5	26 550.70	6.5	26 969.10	6.6	24 815.00
B06	24 527.30	7.2	26 623.00	6.3	27 070.90	6.3	23 700.00
B07	24 989.60	5.4	27 041.40	4.8	27 519.00	4.7	23 925.00
C01	24 556.00	7.1	26 678.40	6.1	27 128.50	6.1	24 980.00
C03	24 134.00	8.7	26 314.60	7.3	26 726.10	7.5	24 238.00
C06	24 412.20	7.6	26 514.60	6.6	26 965.00	6.6	24 039.00
C07	24 742.00	6.4	26 833.70	5.5	27 292.00	5.5	25 251.00
D01	24 380.70	7.7	26 562.40	6.5	27 022.70	6.4	24 965.00
D07	24 825.60	6	26 893.40	5.3	27 320.00	5.4	25 512.00
E01	24 523.90	7.2	26 637.00	6.2	27 121.40	6.1	25 480.00
E02	24 471.20	7.4	26 530.80	6.6	27 045.80	6.4	25 820.00
E03	24 481.10	7.3	26 554.90	6.5	27 087.90	6.2	26 232.00
E04	24 583.90	7	26 630.70	6.2	27 146.70	6	24 459.00
E05	24 587.30	6.9	26 619.10	6.3	27 137.30	6	25 522.00
E06	24 519.40	7.2	26 573.80	6.4	27 080.20	6.2	25 483.00
E07	24 723.00	6.4	26 793.10	5.7	27 291.60	5.5	24 907.00
F01	24 556.70	7.1	26 684.20	6	27 127.50	6.1	25 467.00
F02	24 212.60	8.4	26 334.50	7.3	26 797.80	7.2	24 700.00
F03	24 147.60	8.6	26 277.70	7.5	26 727.10	7.5	24 102.00
F04	24 135.90	8.7	26 263.10	7.5	26 762.90	7.3	23 565.00
F05	24 064.80	8.9	26 215.50	7.7	26 699.10	7.6	25 204.00
F06	24 164.20	8.5	26 307.90	7.4	26 789.50	7.3	23 345.00
F07	24 646.40	6.7	26 755.90	5.8	27 219.70	5.8	25 011.00
Total	863 636.90	6.61	936 211.20	5.82	952 592.10	5.77	867 820.00

(d) Turbine production using raw power curve and Eddy-viscosity wake model

WTG	NORA3	WL [%]	ERA5	WL [%]	NEWA	WL [%]	SCADA
A01	25 521.90	3.4	27 474.50	3.3	27 998.20	3.1	25 225.00
A02	25 140.00	4.9	27 107.90	4.6	27 610.90	4.4	24 370.00
A03	25 055.50	5.2	27 054.10	4.7	27 538.40	4.7	24 473.00
A04	25 121.90	4.9	27 114.70	4.5	27 608.10	4.4	24 526.00
A05	25 157.90	4.8	27 084.90	4.6	27 550.50	4.6	24 304.00
A06	25 319.20	4.2	27 233.30	4.1	27 771.30	3.9	24 823.00
A07	25 629.70	3	27 616.50	2.8	28 094.20	2.7	24 279.00
B01	24 413.70	7.6	26 569.40	6.4	26 866.40	7	25 244.00
B02	23 457.60	11.2	25 677.60	9.6	26 008.10	10	24 281.00
B02	23 840.60	9.8	26 012.00	8.4	26 298.10	9	26 249.00
B03	23 769.10	10	25 931.20	8.7	26 284.80	9	25 466.00
B04	23 804.90	9.9	26 013.30	8.4	26 265.10	9.1	23 858.00
B05	23 829.20	9.8	25 988.40	8.5	26 313.10	8.9	24 815.00
B06	23 922.00	9.5	26 068.70	8.2	26 430.10	8.5	23 700.00
B07	24 621.10	6.8	26 701.00	6	27 128.40	6.1	23 925.00
C01	24 096.80	8.8	26 277.20	7.5	26 658.20	7.7	24 980.00
C03	23 440.00	11.3	25 749.10	9.3	26 042.90	9.8	24 238.00
C06	23 769.20	10	25 930.60	8.7	26 332.00	8.8	24 039.00
C07	24 344.00	7.9	26 478.40	6.8	26 903.70	6.9	25 251.00
D01	23 905.30	9.5	26 117.40	8	26 555.20	8.1	24 965.00
D07	24 445.60	7.5	26 518.40	6.6	26 946.60	6.7	25 512.00
E01	24 023.30	9.1	26 175.00	7.8	26 643.60	7.8	25 480.00
E02	23 659.50	10.5	25 776.00	9.2	26 289.10	9	25 820.00
E03	23 632.80	10.6	25 754.10	9.3	26 325.50	8.9	26 232.00
E04	23 806.10	9.9	25 899.30	8.8	26 422.50	8.5	24 459.00
E05	23 826.50	9.8	25 877.70	8.9	26 408.10	8.6	25 522.00
E06	23 764.30	10.1	25 870.20	8.9	26 374.70	8.7	25 483.00
E07	24 362.50	7.8	26 442.90	6.9	26 929.90	6.8	24 907.00
F01	24 096.40	8.8	26 288.80	7.4	26 683.80	7.6	25 467.00
F02	23 371.70	11.5	25 596.30	9.9	25 995.80	10	24 700.00
F03	23 427.80	11.3	25 639.30	9.7	26 054.90	9.8	24 102.00
F04	23 243.00	12	25 443.80	10.4	25 900.60	10.3	23 565.00
F05	23 276.70	11.9	25 499.60	10.2	25 933.70	10.2	25 204.00
F06	23 439.70	11.3	25 678.60	9.6	26 095.20	9.7	23 345.00
F07	24 314.50	8	26 430.80	6.9	26 888.40	6.9	25 011.00
Total	844 850.00	8.65	919 091.00	7.53	934 150.10	7.61	867 820.00

(e) Turbine production using raw meso-data, raw power curve, and Jensen model

WTG	NORA3	WL [%]	ERA5	WL [%]	NEWA	WL [%]	SCADA
A01	30 281.00	2.4	27 861.80	3	30 092.00	2.5	25 225.00
A02	30 035.50	3.2	27 590.30	3.9	29 831.00	3.4	24 370.00
A03	29 954.60	3.5	27 514.20	4.2	29 736.80	3.7	24 473.00
A04	29 992.00	3.3	27 551.90	4.1	29 777.80	3.6	24 526.00
A05	29 963.00	3.4	27 521.30	4.2	29 723.90	3.7	24 304.00
A06	30 098.50	3	27 658.40	3.7	29 898.80	3.2	24 823.00
A07	30 312.80	2.3	27 926.90	2.7	30 141.50	2.4	24 279.00
B01	29 569.00	4.7	27 171.80	5.4	29 353.70	4.9	25 244.00
B02	28 914.70	6.8	26 505.00	7.7	28 737.70	6.9	24 281.00
B02	29 203.70	5.9	26 769.70	6.8	28 965.40	6.2	26 249.00
B03	29 140.30	6.1	26 694.00	7	28 938.80	6.3	25 466.00
B04	29 185.10	5.9	26 755.00	6.8	28 957.60	6.2	23 858.00
B05	29 159.40	6	26 718.20	7	28 933.90	6.3	24 815.00
B06	29 239.30	5.8	26 796.90	6.7	29 049.70	5.9	23 700.00
B07	29 669.70	4.4	27 245.10	5.1	29 490.60	4.5	23 925.00
C01	29 259.50	5.7	26 882.20	6.4	29 116.40	5.7	24 980.00
C03	28 880.10	6.9	26 478.90	7.8	28 716.00	7	24 238.00
C06	29 137.10	6.1	26 693.60	7	28 964.60	6.2	24 039.00
C07	29 444.60	5.1	27 018.00	5.9	29 260.60	5.2	25 251.00
D01	29 130.30	6.1	26 757.20	6.8	29 010.50	6	24 965.00
D07	29 510.00	4.9	27 092.00	5.7	29 304.10	5.1	25 512.00
E01	29 245.50	5.7	26 836.50	6.5	29 100.50	5.7	25 480.00
E02	29 207.50	5.9	26 716.20	7	29 032.30	6	25 820.00
E03	29 209.20	5.9	26 737.70	6.9	29 059.20	5.9	26 232.00
E04	29 305.50	5.5	26 822.30	6.6	29 126.60	5.7	24 459.00
E05	29 298.90	5.6	26 809.90	6.6	29 112.80	5.7	25 522.00
E06	29 250.10	5.7	26 763.70	6.8	29 066.40	5.9	25 483.00
E07	29 424.60	5.2	26 988.80	6	29 257.60	5.2	24 907.00
F01	29 263.30	5.7	26 896.20	6.3	29 120.80	5.7	25 467.00
F02	28 967.50	6.6	26 519.30	7.6	28 794.60	6.7	24 700.00
F03	28 902.40	6.8	26 449.60	7.9	28 716.40	7	24 102.00
F04	28 904.10	6.8	26 431.20	8	28 751.50	6.9	23 565.00
F05	28 839.00	7	26 379.50	8.1	28 687.70	7.1	25 204.00
F06	28 930.20	6.8	26 475.90	7.8	28 775.10	6.8	23 345.00
F07	29 352.50	5.4	26 941.40	6.2	29 179.60	5.5	25 011.00
Total	1028180.50	5.32	942970.60	6.18	1 021 782.50	5.45	867 820.00

(f) Turbine production using raw meso-data, raw power curve, and Eddy-viscosity model

WTG	NORA3	WL [%]	ERA5	WL [%]	NEWA	WL [%]	SCADA
A01	30 129.60	2.9	27 711.00	3.5	29 945.84	3	25 225.00
A02	29 764.50	4.1	27 307.70	4.9	29 550.45	4.3	24 370.00
A03	29 676.90	4.3	27 250.90	5.1	29 468.60	4.6	24 473.00
A04	29 737.40	4.2	27 315.50	4.9	29 542.13	4.3	24 526.00
A05	29 747.30	4.1	27 292.10	5	29 488.75	4.5	24 304.00
A06	29 907.70	3.6	27 450.90	4.4	29 714.73	3.8	24 823.00
A07	30 237.50	2.5	27 867.20	3	30 051.38	2.7	24 279.00
B01	29 057.30	6.3	26 749.90	6.8	28 813.73	6.7	25 244.00
B02	28 136.40	9.3	25 815.40	10.1	27 976.03	9.4	24 281.00
B02	28 510.50	8.1	26 141.20	9	28 251.90	8.5	26 249.00
B03	28 426.00	8.4	26 065.80	9.2	28 235.53	8.5	25 466.00
B04	28 467.60	8.2	26 136.80	9	28 214.06	8.6	23 858.00
B05	28 497.40	8.2	26 119.70	9	28 262.67	8.5	24 815.00
B06	28 582.50	7.9	26 202.00	8.8	28 383.61	8.1	23 700.00
B07	29 268.30	5.7	26 882.00	6.4	29 072.74	5.8	23 925.00
C01	28 745.20	7.4	26 458.60	7.9	28 624.13	7.3	24 980.00
C03	28 135.10	9.3	25 881.20	9.9	28 000.53	9.3	24 238.00
C06	28 447.70	8.3	26 071.10	9.2	28 311.65	8.3	24 039.00
C07	29 006.40	6.5	26 641.00	7.2	28 840.80	6.6	25 251.00
D01	28 611.70	7.8	26 291.20	8.4	28 518.60	7.6	24 965.00
D07	29 109.40	6.2	26 690.80	7.1	28 901.57	6.4	25 512.00
E01	28 728.80	7.4	26 346.00	8.3	28 609.74	7.3	25 480.00
E02	28 407.20	8.4	25 914.30	9.8	28 267.49	8.4	25 820.00
E03	28 362.60	8.6	25 895.40	9.8	28 286.07	8.4	26 232.00
E04	28 539.90	8	26 046.80	9.3	28 396.10	8	24 459.00
E05	28 547.50	8	26 027.90	9.4	28 375.73	8.1	25 522.00
E06	28 500.40	8.1	26 013.90	9.4	28 347.09	8.2	25 483.00
E07	29 052.80	6.4	26 618.10	7.3	28 882.86	6.5	24 907.00
F01	28 778.40	7.2	26 481.60	7.8	28 672.79	7.1	25 467.00
F02	28 108.70	9.4	25 740.10	10.4	27 980.25	9.4	24 700.00
F03	28 169.60	9.2	25 780.90	10.2	28 034.52	9.2	24 102.00
F04	27 995.60	9.8	25 567.40	11	27 881.63	9.7	23 565.00
F05	28 027.80	9.7	25 623.60	10.8	27 908.09	9.6	25 204.00
F06	28 188.00	9.1	25 807.90	10.1	28 066.24	9.1	23 345.00
F07	28 996.60	6.5	26 604.40	7.4	28 834.89	6.6	25 011.00
Total	1008606.30	7.12	924810.30	7.99	1 002 712.92	7.21	867 820.00

(g) Turbine production using raw meso-data, corrected power curve, and Jensen model

WTG	NORA3	WL [%]	ERA5	WL [%]	NEWA	WL [%]	SCADA
A01	28 738.60	2.5	26 252.00	3.1	28 586.70	2.6	25 225.00
A02	28 499.00	3.3	25 994.10	4	28 334.20	3.5	24 370.00
A03	28 418.80	3.6	25 920.90	4.3	28 245.00	3.8	24 473.00
A04	28 457.80	3.4	25 957.80	4.2	28 286.00	3.6	24 526.00
A05	28 434.30	3.5	25 934.90	4.2	28 237.80	3.8	24 304.00
A06	28 566.90	3.1	26 066.70	3.8	28 411.40	3.2	24 823.00
A07	28 771.00	2.4	26 323.90	2.8	28 642.40	2.4	24 279.00
B01	28 029.30	4.9	25 578.00	5.6	27 853.20	5.1	25 244.00
B02	27 377.00	7.1	24 925.10	8	27 237.90	7.2	24 281.00
B02	27 668.80	6.1	25 187.90	7	27 470.70	6.4	26 249.00
B03	27 607.30	6.3	25 119.30	7.3	27 446.20	6.5	25 466.00
B04	27 650.10	6.2	25 178.80	7	27 464.40	6.4	23 858.00
B05	27 622.50	6.3	25 140.80	7.2	27 444.40	6.5	24 815.00
B06	27 700.80	6	25 215.30	6.9	27 555.90	6.1	23 700.00
B07	28 128.50	4.5	25 652.40	5.3	27 991.10	4.6	23 925.00
C01	27 719.60	5.9	25 290.90	6.6	27 612.90	5.9	24 980.00
C03	27 339.20	7.2	24 898.90	8.1	27 216.90	7.3	24 238.00
C06	27 594.50	6.4	25 104.70	7.3	27 459.70	6.4	24 039.00
C07	27 901.30	5.3	25 424.70	6.1	27 760.70	5.4	25 251.00
D01	27 577.20	6.4	25 158.00	7.1	27 498.70	6.3	24 965.00
D07	27 969.40	5.1	25 493.30	5.9	27 797.00	5.3	25 512.00
E01	27 697.90	6	25 233.80	6.8	27 593.80	6	25 480.00
E02	27 659.20	6.1	25 117.50	7.3	27 524.60	6.2	25 820.00
E03	27 661.40	6.1	25 145.90	7.2	27 557.30	6.1	26 232.00
E04	27 758.00	5.8	25 228.20	6.9	27 624.20	5.9	24 459.00
E05	27 755.70	5.8	25 220.20	6.9	27 614.40	5.9	25 522.00
E06	27 702.60	6	25 174.40	7	27 568.20	6.1	25 483.00
E07	27 880.70	5.4	25 395.80	6.2	27 762.50	5.4	24 907.00
F01	27 719.80	5.9	25 304.10	6.6	27 618.50	5.9	25 467.00
F02	27 422.90	6.9	24 936.00	7.9	27 296.60	7	24 700.00
F03	27 359.50	7.2	24 872.00	8.2	27 220.70	7.3	24 102.00
F04	27 357.30	7.2	24 852.00	8.2	27 255.20	7.1	23 565.00
F05	27 291.30	7.4	24 799.70	8.4	27 189.50	7.4	25 204.00
F06	27 384.30	7.1	24 893.10	8.1	27 276.80	7.1	23 345.00
F07	27 807.40	5.6	25 352.10	6.4	27 681.90	5.7	25 011.00
Total	974 229.90	5.54	887343.20	6.40	969 337.40	5.64	867 820.00

(h) Turbine production using raw meso-data, corrected power curve, and Eddy-viscosity wake model.

WTG	NORA3	WL [%]	ERA5	WL [%]	NEWA	WL [%]	SCADA
A01	28 571.60	3	26 188.50	3.7	28 426.70	3.2	25 225.00
A02	28 206.70	4.3	25 703.00	5.1	28 040.50	4.5	24 370.00
A03	28 120.90	4.6	25 746.00	5.3	27 962.70	4.7	24 473.00
A04	28 185.00	4.4	25 708.10	5.1	28 035.70	4.5	24 526.00
A05	28 205.10	4.3	25 695.40	5.1	27 989.90	4.6	24 304.00
A06	28 365.20	3.7	25 851.30	4.6	28 218.50	3.9	24 823.00
A07	28 683.80	2.7	26 254.70	3.1	28 541.30	2.8	24 279.00
B01	27 500.30	6.7	25 148.10	7.1	27 293.10	7	25 244.00
B02	26 570.90	9.8	24 219.20	10.6	26 444.00	9.9	24 281.00
B02	26 952.60	8.5	24 552.30	9.3	26 732.70	8.9	26 249.00
B03	26 871.90	8.8	24 483.70	9.6	26 716.20	9	25 466.00
B04	26 910.40	8.7	24 550.80	9.4	26 693.70	9.1	23 858.00
B05	26 939.90	8.6	24 535.30	9.4	26 746.10	8.9	24 815.00
B06	27 028.10	8.3	24 616.90	9.1	26 866.00	8.5	23 700.00
B07	27 710.50	6	25 479.90	6.7	27 552.10	6.1	23 925.00
C01	27 180.60	7.8	24 952.00	8.2	27 091.60	7.7	24 980.00
C03	26 561.90	9.9	24 282.60	10.3	26 470.60	9.8	24 238.00
C06	26 879.20	8.8	24 467.20	9.7	26 777.90	8.8	24 039.00
C07	27 442.20	6.9	25 035.00	7.6	27 319.50	6.9	25 251.00
D01	27 021.60	8.3	24 869.00	8.9	26 970.10	8.1	24 965.00
D07	27 540.40	6.5	25 071.10	7.4	27 367.20	6.8	25 512.00
E01	27 142.50	7.9	24 718.60	8.7	27 063.80	7.8	25 480.00
E02	26 811.00	9	24 385.90	10.3	26 716.20	9	25 820.00
E03	26 769.00	9.2	24 374.30	10.4	26 740.70	8.9	26 232.00
E04	26 944.70	8.6	24 519.00	9.8	26 848.70	8.5	24 459.00
E05	26 961.40	8.5	24 407.50	9.9	26 836.70	8.6	25 522.00
E06	26 911.20	8.7	24 598.80	9.9	26 812.30	8.7	25 483.00
E07	27 476.80	6.8	25 003.00	7.7	27 357.10	6.8	24 907.00
F01	27 198.80	7.7	24 963.40	8.2	27 133.10	7.6	25 467.00
F02	26 519.60	10	24 129.00	10.9	26 441.60	9.9	24 700.00
F03	26 576.90	9.8	24 269.10	10.8	26 497.10	9.7	24 102.00
F04	26 401.70	10.4	23 955.10	11.6	26 340.00	10.3	23 565.00
F05	26 435.00	10.3	24 113.20	11.3	26 364.70	10.2	25 204.00
F06	26 599.00	9.7	24 198.70	10.7	26 527.20	9.6	23 345.00
F07	27 419.40	7	24 992.60	7.7	27 302.80	7	25 011.00
Total	953 615.80	7.55	870038.30	8.38	949 238.10	7.61	867 820.00

Appendix 2 – Analysis of Best Scenario

Sector	0 N	1NNE	2ENE	3E	4ESE	5SSE
[1]	77 009	32 908	32 316	27 209	33 269	53 348
[2]	3 823	2 983	4 659	2 541	1 854	7 602
[3]	5.0	9.1	14.4	9.3	5.6	14.2
[4]	73 186	29 925	27 656	24 669	31 415	45 747
[5]	349	143	132	117	150	218

Sector	6S	7SSW	8WSW	9W	10WNW	11NNW
[1]	95 189	138 397	173 511	155 317	57 412	63 759
[2]	4 919	8 217	16 218	11 828	3 749	5 828
[3]	5.2	5.9	9.3	7.6	6.5	9.1
[4]	90 269	130 179	157 292	143 489	53 662	57 932
[5]	430	620	749	683	256	276

	Total
[1]	939 644
[2]	74 223
[3]	7.90
[4]	865 422
[5]	4 121

Table 32 : PARK production sectional analysis using scaled ERA 5 with corrected power curve and Eddy viscosity wake model. [1] is the model based energy (MWh); [2] is the decrease due to wake losses (MWh); [3] is the percentage decrease due to wake losses (%); [4] is the resulting energy (MWh); and [5] is the full load equivalent (Hours/year).

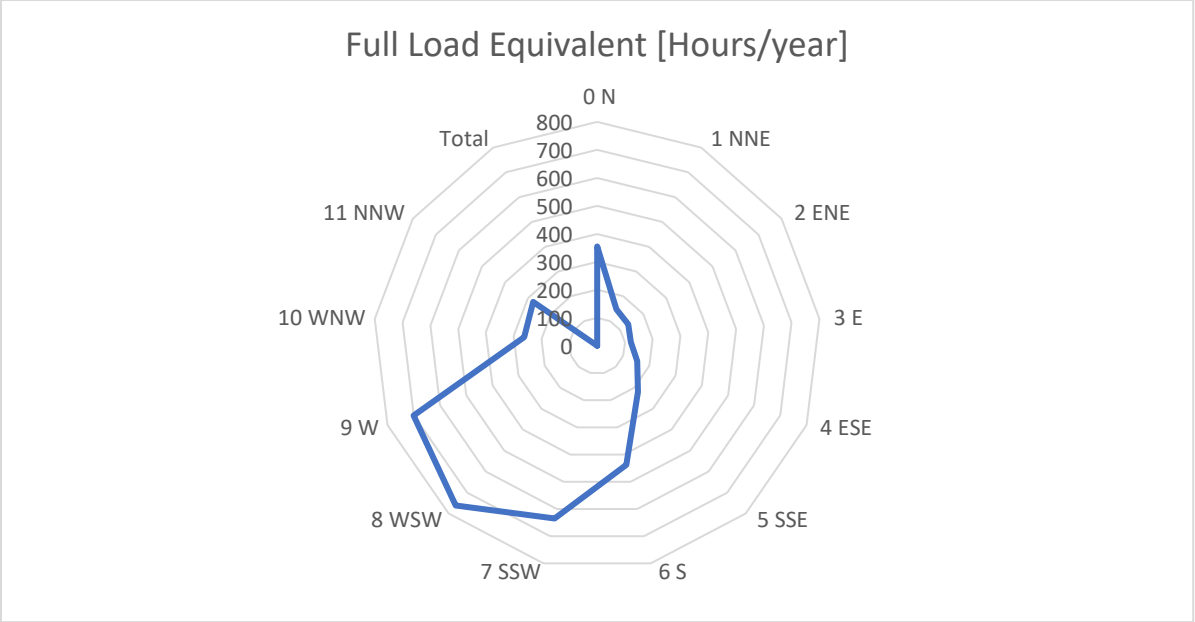

Figure 46: Full Load Equivalent by sector [Hours/year] using scaled ERA 5 with corrected power curve and Eddy viscosity wake model. Figure represents data from [5] in table 29.

Hour/Month [MWh]	1	2	3	4	5	6	7	8	9	10	11	12	Grand Total
0	3 133	4 012	3 327	3 354	3 027	2 483	2 781	2 855	3 133	3 921	3 540	1 985	37 552
1	3 101	3 856	3 458	3 354	3 021	2 339	2 915	2 829	3 151	3 867	3 524	1 912	37 325
2	3 068	3 629	3 547	3 356	3 016	2 419	2 882	2 737	3 043	3 879	3 558	1 940	37 073
3	3 032	3 840	3 630	3 201	3 041	2 367	2 828	2 621	2 989	3 951	3 648	2 002	37 149
4	3 116	3 835	3 526	3 117	3 086	2 385	2 816	2 510	3 013	3 986	3 797	2 080	37 267
5	3 103	3 963	3 476	3 074	3 142	2 400	2 728	2 458	3 041	3 957	3 927	2 105	37 375
6	3 167	3 950	3 421	2 990	3 176	2 291	2 574	2 501	3 074	3 931	4 053	2 167	37 295
7	3 148	3 938	3 389	2 873	3 119	2 334	2 479	2 428	3 087	3 867	4 047	2 167	36 876
8	3 101	3 932	3 201	2 873	3 027	2 236	2 368	2 436	3 116	3 913	3 933	2 116	36 251
9	3 123	4 067	3 334	2 742	2 983	2 174	2 248	2 391	3 099	3 810	3 923	2 051	35 944
10	3 042	3 922	3 054	2 424	2 654	1 992	1 960	2 320	2 857	3 629	3 552	1 972	33 378
11	3 072	3 899	2 964	2 398	2 817	2 042	2 038	2 382	2 931	3 676	3 464	1 985	33 669
12	3 058	3 801	2 896	2 416	2 867	2 271	2 066	2 467	3 028	3 732	3 491	1 951	34 043
13	2 978	3 655	2 936	2 501	2 972	2 453	1 963	2 510	3 125	3 768	3 541	1 950	34 353
14	2 957	3 650	2 968	2 511	3 123	2 521	2 106	2 446	3 100	3 780	3 537	1 980	34 679
15	2 900	3 619	3 021	2 566	3 104	2 512	2 156	2 573	3 082	3 808	3 544	2 057	34 941
16	2 842	3 658	2 967	2 663	3 094	2 601	2 109	2 666	2 930	3 748	3 485	2 068	34 833
17	2 914	3 671	2 985	2 816	3 173	2 555	2 267	2 757	2 855	3 866	3 478	2 104	35 442
18	3 070	3 756	2 984	2 949	3 262	2 496	2 038	2 750	2 958	3 854	3 601	2 174	35 894
19	3 135	3 815	3 049	2 981	3 332	2 423	1 970	2 609	3 022	3 859	3 778	2 107	36 081
20	3 158	3 970	3 167	3 229	3 374	2 392	2 014	2 728	3 148	3 879	3 784	2 005	36 849
21	3 160	4 031	3 194	3 223	3 336	2 423	2 188	2 780	3 193	3 923	3 751	1 977	37 179
22	3 124	3 919	3 131	3 203	3 135	2 473	2 320	2 737	3 245	3 784	3 675	2 016	36 762
23	3 219	3 897	3 186	3 320	3 135	2 503	2 410	2 791	3 212	3 903	3 610	2 025	37 211
Grand Total	73 720	92 286	76 811	70 136	74 016	57 086	56 223	62 281	73 431	92 293	88 241	48 898	865422

Table 33: PARK time varying AEP using scalaed ERA5, corrected power curve and Eddy viscosity wake model. The table shows the mean yield per month and hpur [MWh]. The results include wake losses and any curtailment losses.

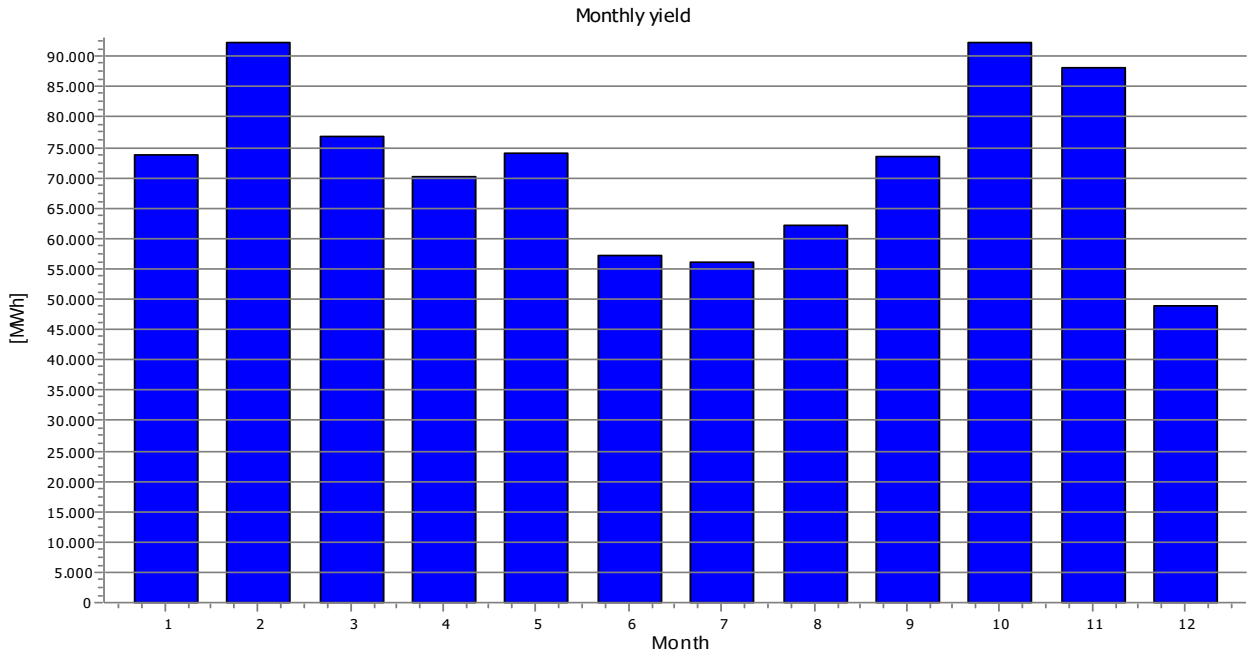

Figure 47: PARK time varying AEP using scalaed ERA5, corrected power curve and Eddy viscosity wake model. Figure displays monthly mean yield and includes wake losses and any curtailment losses and is based on the 210 MW windfarm consisting of 35 turbines.

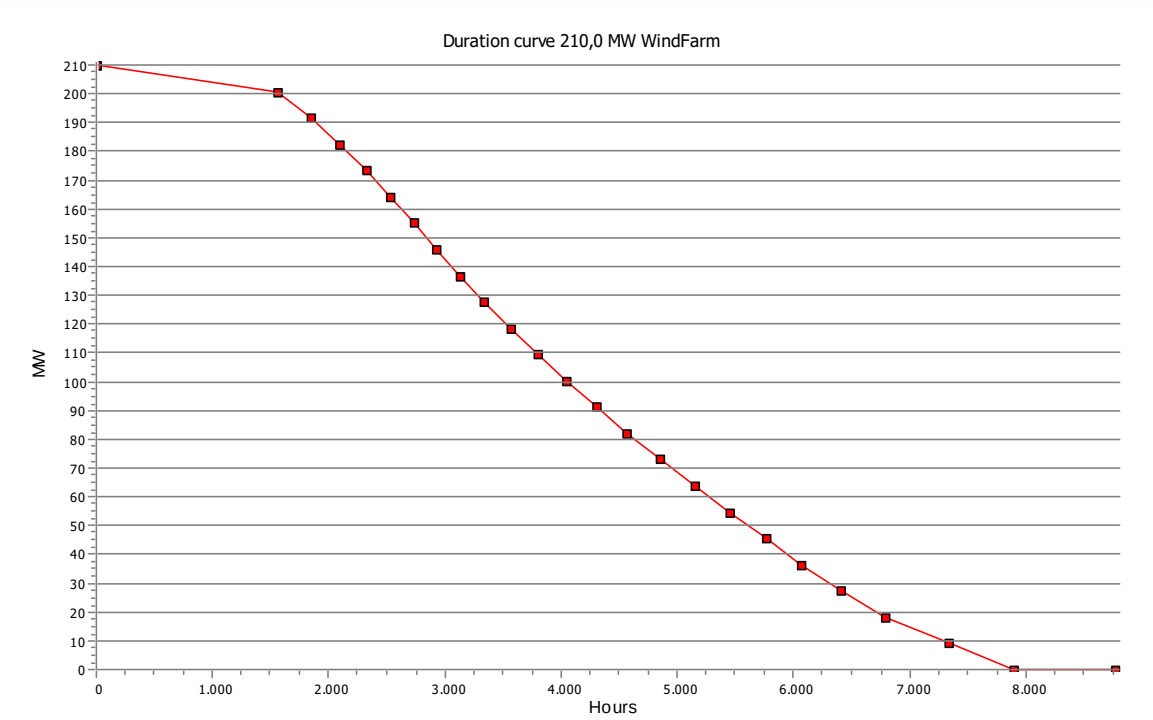

Figure 48: PARK time varying AEP using scalaed ERA5, corrected power curve and Eddy viscosity wake model. Figure displays the duration curve of the 210 MW wind farm consisting 35 turbines. The results includes wake losses and any curtailment losses.

Appendix 3 – Park Layout and spacing

Figure 49: Park Layout created in google earth with input data from WindPRO.

WTG distances			
	Nearest WTG	Horizontal distance [m]	number of rotor distances
C03	B02	981	6.4
B04	B05	955	6.2
E04	E05	966	6.3
B05	B06	922	6
C06	C07	977	6.3
B03	B02	920	6
B02	C01	948	6.2
E05	E06	905	5.9
E03	E02	908	5.9
B06	B05	922	6
B02	B03	920	6
E06	E05	905	5.9
E02	E03	908	5.9
A04	A05	968	6.3
A05	A06	923	6
C07	C06	977	6.3
D07	E07	1133	7.4
A03	A02	898	5.8
F04	F05	944	6.1
C01	B02	948	6.2
D01	E01	1103	7.2
F05	F06	917	6
F03	F02	954	6.2
B07	B06	969	6.3
A06	A05	923	6
E07	E06	946	6.1
A02	A03	898	5.8
B01	B02	951	6.2
E01	E02	939	6.1
F06	F07	904	5.9
F02	F01	951	6.2
A07	A06	959	6.2
A01	A02	1010	6.6
F07	F06	904	5.9
F01	F02	951	6.2

Table 34: WTG spacing inside the WMR wind farm. Table displays closest WTG in horizontal distance by meter, and by number of rotor diameters.

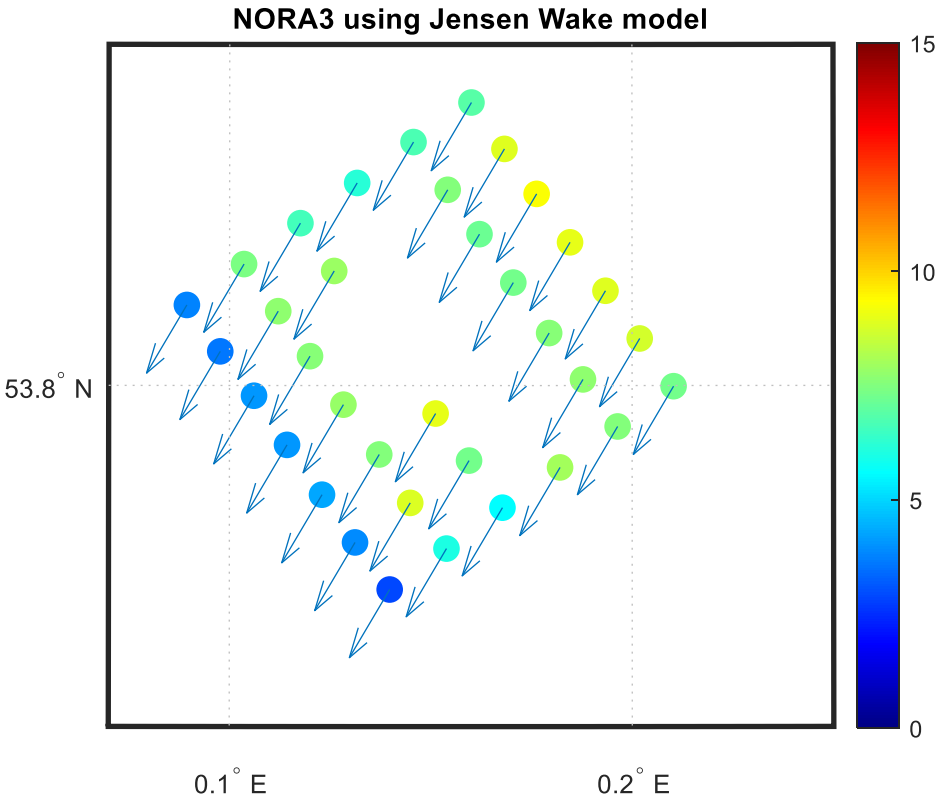

Figure 50: WTG layout and main yaw angle; MATLAB.

Appendix 4 – Shear Analysis

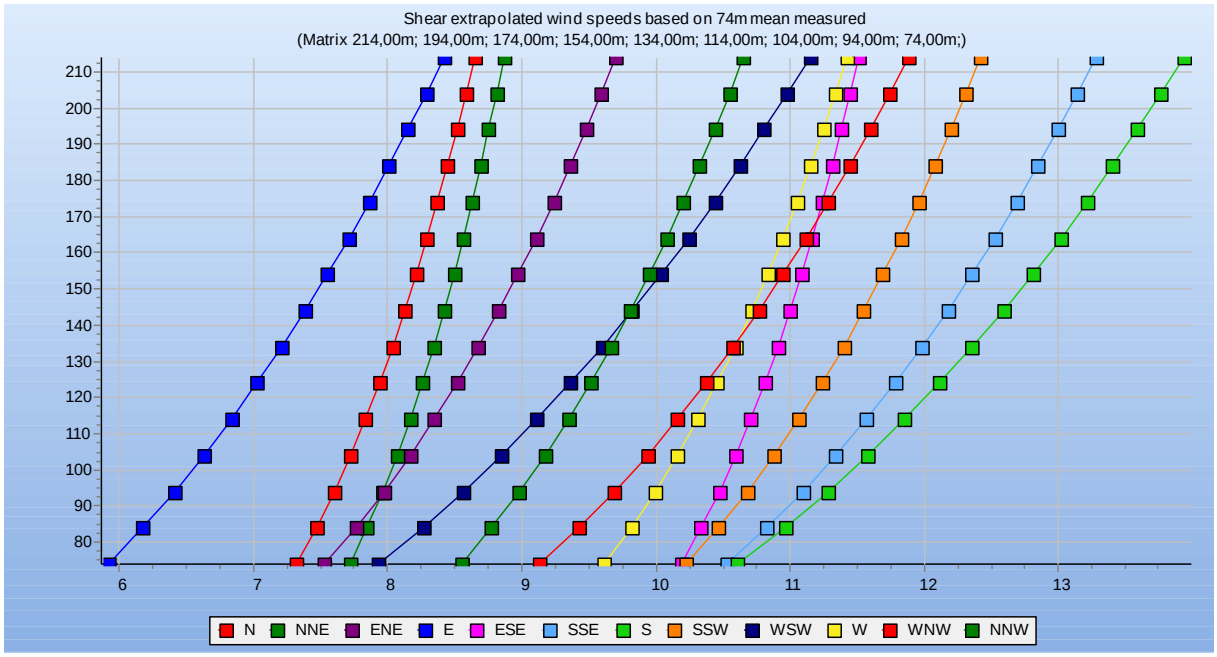

Figure 51: Shear extrapolated wind speeds based on 74m mean measured. Figure displays directional wind shear for scaled ERA5; WindPRO.

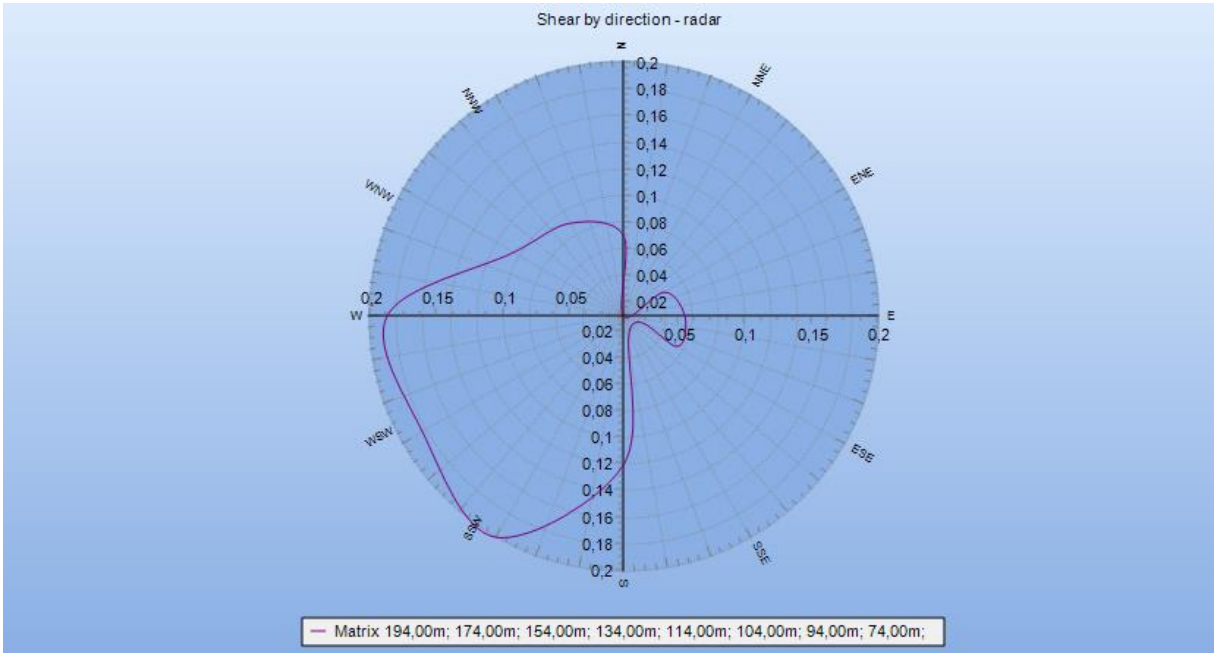

Figure 52: Shear by direction presented in radar graph. Figure displays wind shear for scaled ERA5; WindPRO.

Appendix 5 – Wake decay coefficient

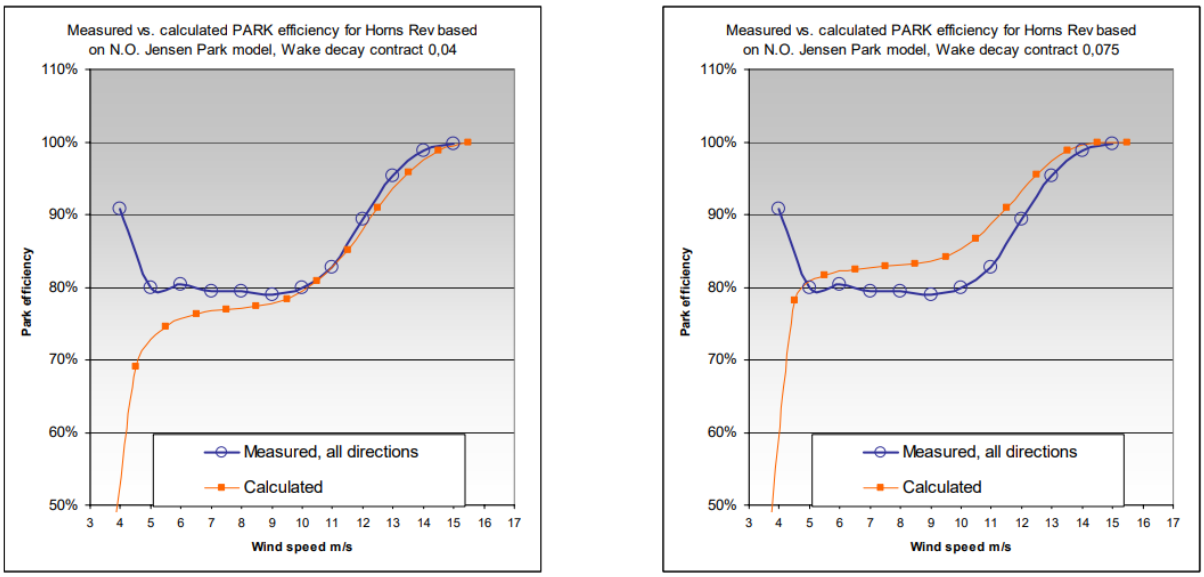

(a) (b)

Figure 53: Park efficiency comparison, WDC=0.04 (a); WDC=0.075(b). ref: Sørensen et al (2006).